AD-A154 575 BUBBLE DYNAMICS IN POLYMER SOLUTIONS UNDERGOING SHEAR 1/2
(U) PRINCETON UNIV NJ DEPT OF CHEMICAL ENGINEERING
P S KEZIOS 01 APR 85 160-6076-4 N00014-79-C-0385

UNCLASSIFIED F/G 20/4 NL

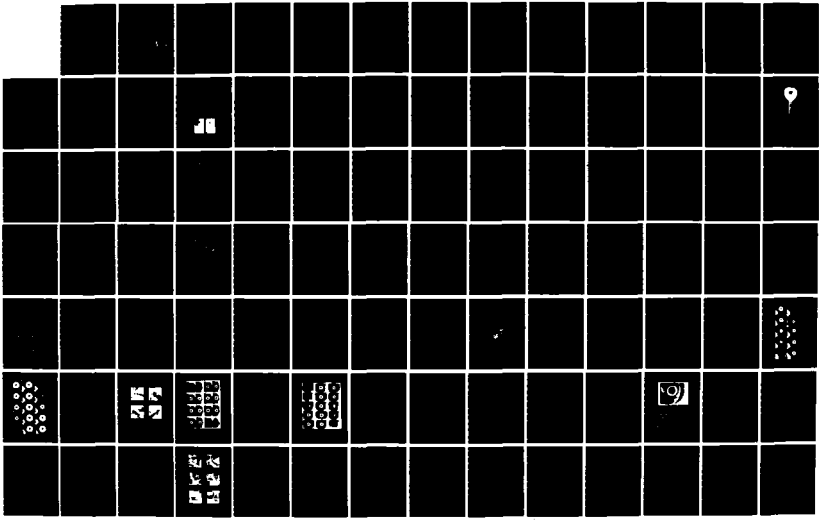

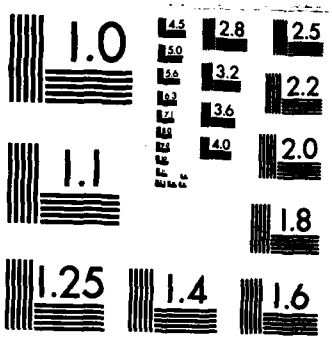

MICROCOPY RESOLUTION TEST CHART
NATIONAL BUREAU OF STANDARDS-1963-A

SECURITY CLASSIFICATION OF THIS PAGE (When Data Entered)

REPORT DOCUMENTATION PAGE

READ INSTRUCTIONS BEFORE COMPLETING FORM

1. REPORT NUMBER: 160-6076-4
2. GOVT ACCESSION NO.:
3. RECIPIENT'S CATALOG NUMBER: (4)

4. TITLE (and Subtitle): Bubble Dynamics in Polymer Solutions Undergoing Shear

5. TYPE OF REPORT & PERIOD COVERED: Interim

6. PERFORMING ORG. REPORT NUMBER:

7. AUTHOR(s): Peter S. Kezios

8. CONTRACT OR GRANT NUMBER(s): N00014-79-C-0385

9. PERFORMING ORGANIZATION NAME AND ADDRESS:
Department of Chemical Engineering
Princeton University
Princeton, NJ 08544

10. PROGRAM ELEMENT, PROJECT, TASK AREA & WORK UNIT NUMBERS: NR 062-637

11. CONTROLLING OFFICE NAME AND ADDRESS:
Office of Naval Research (Code 438)
800 N. Quincy Street
Arlington, VA 22217

12. REPORT DATE: 1 April 1985

13. NUMBER OF PAGES: 166

14. MONITORING AGENCY NAME & ADDRESS (if different from Controlling Office):

15. SECURITY CLASS. (of this report): Unclassified

15a. DECLASSIFICATION/DOWNGRADING SCHEDULE:

16. DISTRIBUTION STATEMENT (of this Report)

Approved for public release; distribution unlimited.

17. DISTRIBUTION STATEMENT (of the abstract entered in Block 20, if different from Report)

DTIC ELECTE JUN 6 1985 S D A

18. SUPPLEMENTARY NOTES

Ph.D. Dissertation of Peter S. Kezios

19. KEY WORDS (Continue on reverse side if necessary and identify by block number)

cavitation, rheology, non-Newtonian fluid mechanics, bubbles, nonspherical, viscoelastic liquids, polymers.

20. ABSTRACT (Continue on reverse side if necessary and identify by block number)

Hydraulic cavitation and its effects have been reported to be substantially inhibited and subsequently suppressed by the addition of minute quantities of water-soluble polymer. Modelling the growth and collapse of a single cavitation bubble in water has been established as the fundamental theoretical approach to understanding this phenomenon. Laser-induced cavitation has been developed as a technique for the

DD FORM 1 JAN 73 1473 EDITION OF 1 NOV 65 IS OBSOLETE
S/N 0102-LF-014-6601

SECURITY CLASSIFICATION OF THIS PAGE (When Data Entered)

AD-A154 575

DTIC FILE COPY

85 04 16 074

20. (continued)

experimental investigation and confirmation of predicted spherical and nonspherical bubble dynamics in quiescent viscous fluids.

Previous extensions of single bubble models have included fluid viscoelasticity to explain the macroscopic observations of cavitation inhibition. However, for spherical dynamics in a quiescent fluid, the effect of viscoelasticity was theoretically and experimentally found to be negligible. Fluid rheology was predicted to have a small effect on the behavior of nonspherical bubbles in this quiescent case. Such changes were predicted to be greater with an imposed external flow.

The present experimental research has sought to form a link between previous theoretical and experimental efforts. Optical cavitation has been used to create model cavitation bubbles nonintrusively within a fluid undergoing a steady shear flow history. The flow-induced deformation of these single bubbles was recorded and analyzed. Originator Supplied Keywords include:

The amplitude of bubble deformation was found to increase linearly with flow strength over a range of shear from 0 to 250 sec^{-1}. Fluid viscosity, between 0.01 and 0.16 poise, was found to have only a minimal effect on the magnitude of such deformations. However, fluid elasticity resulting from the addition of polymer solutes in the concentration range of 0 to 2000 wppm was demonstrated to decrease the amplitude of nonsphericity. Competition between viscous and elastic effects was seen at the highest polymer concentration (C = 2000 wppm).

Cont'd DD 1473

Recent modelling efforts involving an oscillatory flow were modified and applied to these steady flow experiments. Agreement between theory and experiment for low-viscosity Newtonian fluids was found to be within the experimental uncertainty of ± 10%. However, agreement worsened (to within ± 15%) as fluid viscosity increased. For viscoelastic fluids, the model qualitatively predicted the deformation suppression which was observed experimentally.

These results have been indirectly related to macroscopic observations through previous research involving pressure-field modelling of nonspherical bubble collapse. That work showed collapse pressure amplitude near a solid wall to increase with increased bubble nonsphericity. This research has established the role of dilute polymer solutions in the suppression of flow-induced bubble nonsphericity. Thus, for hydraulic systems which combine wall proximity and strong flow, the addition of minute quantities of polymer solutes could reasonably be expected to diminish cavitation intensity.

TABLE OF CONTENTS

	page
ABSTRACT	ii
ACKNOWLEDGEMENTS	iii
LIST OF FIGURES	v
LIST OF TABLES	viii
NOMENCLATURE	ix
CHAPTERS:	
I. INTRODUCTION	1
II. PREVIOUS RESEARCH	6
1. Newtonian Analyses	6
2. Non-Newtonian Analyses	19
III. EXPERIMENTAL TECHNIQUES	26
1. Previous Work	26
2. Experimental Apparatus	30
IV. EXPERIMENTAL RESULTS AND DISCUSSION	53
1. Preliminary Experiments	53
2. Data Analysis Techniques	63
3. Flow System Experiments	72
V. MODEL APPLICATION RESULTS	115
VI. CONCLUSIONS AND RECOMMENDATIONS	138
VII. BIBLIOGRAPHY	143
APPENDICES:	153
A. Bubble Energy Experiments	153
B. Sample Calculations	161

Accession For
NTIS GRA&I
DTIC TAB
Unannounced
Justification
By
Distribution/
Availability Codes
Avail and/or
Dist Special
A-1
DTIC COPY INSPECTED

LIST OF FIGURES

figure	title
1-1	Polymer effects on cavitation inception.
1-2	Polymer effects on cavity appearance.
2-1	Spherical laser-induced bubble dynamics.
2-2	Vapor cavity jet formation.
2-3	Bubble collapse near a solid wall.
2-4	Nonspherical vapor bubble collapse.
2-5	Vapor bubble dynamics near a free surface.
2-6A	Nonspherical bubble dynamics in distilled water.
2-6B	Nonspherical bubble dynamics in dilute polymer.
3-1	Closed-loop hydraulic cavitation tunnel.
3-2	Laser system optical components.
3-3	Aspheric laser focussing lens.
3-4	Quiescent fluid test cell.
3-5	Energy measurement test cell.
3-6	Cylindrical Couette flow system.
3-7	Flow system auxilliary equipment.
3-8	High-speed framing camera optics.
4-1	Single-exposure experiment configuration.
4-2A,B	Single-exposure bubble sequences in DH2O.
4-3	High-speed equipment photographs.
4-4	High-speed spherical bubble dynamics (DH2O).

figure	title
4-5	High-speed nonspherical bubble dynamics (DH2O).
4-6	Nonspherical bubble shapes from harmonics.
4-7	Extensional flow field streamlines.
4-8A	Flow-induced bubble shapes from theory.
4-8B	Flow-induced bubble shape from experiment.
4-9A	Flow system experiment configuration.
4-9B	Flow system equipment photographs.
4-10	Equipment configuration near test region.
4-11	Dimensionless bubble radius profile (DH2O).
4-12	Bubble deformation composites (DH2O).
4-13A	Maximum bubble deformations (DH2O).
4-13B	Bubble deformation growth rates (DH2O).
4-14	Flow visualization photographs.
4-15	Experimental flow space diagram.
4-16A	Bubble deformation composites (DH2O(+PAM)).
4-16B	Bubble deformation composites (DH2O(+PEO)).
4-17	Maximum bubble deformations (DH2O(+PAM/PEO)).
4-18	Bubble deformation composites (DH2O(+PEO/PEO*)).
4-19A	Quiescent deformation composites (DH2O(+PAM)).
4-19B	Quiescent deformation composites (DH2O+PEO/PEO*).
4-20	Bubble deformation composites (GLY(2:1)).
4-21	Maximum bubble deformations (GLY(2:1)).
4-22A,B,C	Bubble deformation composites (GLY(1:1)(+PAM)).
4-23	Quiescent deformation composites (GLY(+PAM)).
4-24	Maximum bubble deformations (GLY(1:1)(+PAM)).

figure	title
5-1	Nonspherical bubble dynamics in glycerol/water.
5-2	Best-fit theory for bubble deformation.
5-3	Experiment/theory flow relationship.
5-4	Experiment/theory bubble deformations (DH2O).
5-5A	Experiment/theory bubble deformations (DH2O(+PAM)).
5-5B	Experiment/theory bubble deformations (DH2O(+PEO)).
5-5C	Experiment/theory bubble deformations (GLY(+PAM)).
A-1	Energy measurment experimental configuration.
A-2	Energy measurment equipment photographs.
A-3	Bubble energy versus maximum volume.

LIST OF TABLES

table	title
3-1	Laser system components.
3-2	Aspheric lens specifications.
3-3	Flow system specifications.
3-4	Flow system sample calculations.
3-5	Single-exposure photographic system.
3-6	High-speed photographic system.
3-7	Experimental electronic components.
4-1	High-speed photograhic parameters.
4-2	Deformation analysis relationships.
4-3A,B	Sample experimental raw/reduced data.
4-4	Dimensional spherical parameters (DH2O).
4-5	Summary of flow experiments.
4-6	Polymer product information.
4-7	Solvent and solution properties.
4-8A,B	Elastic effect on bubble deformation reduction.
5-1	Model/experiment nonspherical bubble results.
5-2	Theory/experiment deformation comparison (DH2O).
5-3A,B	Theory/experiment deformation comparison (GLY/DH2O).
A-1	Laser energy calibration results.
A-2	Bubble energy versus maximum size.
B-1	Sample experimental and model parameters.
B-2	Sample bubble composite data.
B-3	Sample bubble model predictions.

NOMENCLATURE

symbol	definition
a	spheroid semiaxis (actual)
$a_{nm} = a_{nm}(t)$	amplitude of the (n,m) spherical harmonic
a_i	amplitude of the (i,0) spherical harmonic
a_0	initial model amplitude
$\dot{a}_0$	initial model amplitude velocity
A	bubble deformation amplitude
A_i	specific bubble deformation amplitude
$\bar{A} = \bar{A}(t/\tau)$	average bubble deformation amplitude
A_s	bubble deformation amplitude in solvent
A_m	model bubble deformation amplitude
$A^*(t)$	complex model flow amplitude function
A^*	complex model flow amplitude constant
b	spheroid semiaxis (actual)
c_∞	speed of sound in liquid
C	(1) speed of sound in liquid (2) (polymer) concentration
C_i	Fourier series coefficients
C_p	specific heat at constant pressure
C_v	specific heat at constant volume
d	focal spot depth
D	(laser pulse) diameter
De	Deborah number
$\underset{\approx}{e}$	strain tensor

symbol	definition
$\dot{\underset{\approx}{e}}$	rate of strain tensor
E	model prediction error
E_b	bubble nucleation energy
E_{cal}	laser calibration energy
E_{net}	transmitted (measured) laser energy
$\exp(x) = e^x$	exponential of x
f , f'	lens focal lengths (in different media)
g	annular gap width
G_e	elastic modulus
h	(gap) height
H	(1) liquid enthalpy (2) (flow system) height
i	integer
$\underset{\approx}{I}$	identity tensor
$\mathrm{Im}(z)$	imaginary part of the complex number z
j	integer
k	Boltzmann's constant
L	reflective energy loss percentage
m	integer
max	maximum value
M	(polymer) molecular weight
n	(1) integer (2) (polymer) number density
n , n'	refractive indices (of different media)
N_{av}	Avagadro's number
p	pressure

symbol	definition
p_∞	ambient pressure
p_g	gas pressure
p_v	vapor pressure
$p(R)$	pressure at the bubble surface
P	power
r	(1) spherical coordinate radius (2) equivalent spherical bubble radius (measured)
$r(\theta,\phi,t)$	bubble shape function
r_f	(flow system) focal radius
$R = R(t)$	equivalent spherical bubble radius (actual)
R_g	bubble radius for $p(R)=p_g$
R_0	maximum spherical bubble radius
$\overline{R}_0$	composite maximum bubble radius
$R_{fit}(t)$	Fourier series bubble radius function
R_i	inner cylinder radius
R_o	outer cylinder radius
R_m	model bubble radius
$Re(A^*)$	real model flow amplitude constant
$ReN(A^*)$	normalized real model flow amplitude constant
$Re(z)$	real part of the complex number z
s	focal spot radius
S	(flow system) side length
$S(r,\theta,\phi,t)$	bubble surface function
t	(1) time (2) (superscript) transpose tensor
t'	past time

symbol	definition
t_j	specific time
t_c	bubble collapse time
t_{decay}	model flow amplitude decay constant
T	temperature
$\underset{\sim}{v}$	velocity vector
v_w	wall velocity
v_∞	free stream velocity
V	volume
V_{cap}	laser capacitor bank charge voltage
$Y_n^m(\theta,\phi)$	spherical harmonic of order n and degree m
α	spheroid semiaxis (measured)
β	spheroid semiaxis (measured)
γ	polytropic gas constant (C_p/C_v)
$\dot{\gamma}$	shear rate
Γ	gamma function
$\Delta(x)$	change in x
$\dot{\varepsilon}$	strain rate
ζ	model flow amplitude decay constant
η	fluid viscosity
η_s	solvent viscosity
θ	(1) spherical coordinate cone angle (2) laser pulse divergence
κ	cylinder size ratio (R_i/R_o)
λ	fluid relaxation time
μ	fluid viscosity

symbol	definition
ν	kinematic viscosity
π	pi (≈ 3.1416)
ρ	fluid density
σ	fluid surface tension
σ_i	incipient cavitation number
$\underset{\approx}{\sigma}$	total stress tensor
Σ	summation
τ	(1) characteristic flow time (2) experimental bubble collapse period
τ_j	specific experimental bubble collapse period
τ_{rr}	normal stress component
$\tau_{r\theta}$	shear stress component
$\underset{\approx}{\tau}$	extra stress tensor
ϕ	spherical coordinate polar angle
ω	rotation rate
ω_t	transition rotation rate
Ω	model flow oscillation frequency
d/dx	total first derivative w.r.t. x
d^2/dx^2	total second derivative w.r.t. x
$\partial/\partial x$	partial first derivative w.r.t. x
$\partial^2/\partial x^2$	partial second derivative w.r.t. x
$\underset{\sim}{\nabla}$	gradient vector
$\cdot$	total first derivative w.r.t. time
$\cdot\cdot$	total second derivative w.r.t. time
$\int$	integral

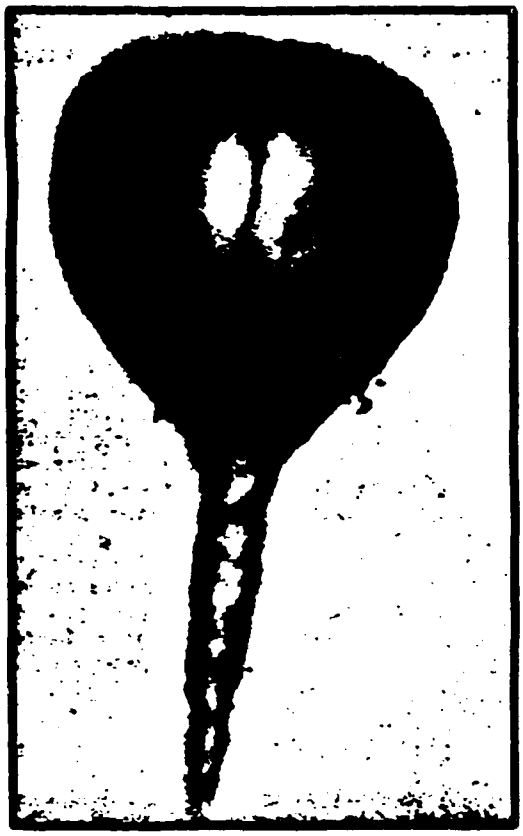

FIGURE 2-2. Vapor cavity in water with a typical well developed jet (Lauterborn, 1979).

with bubble collapse. It has been further postulated that the high-speed impingement of this microjet on a solid surface is a fundamental mechanism of cavitation damage (Kornfeld & Suvorov, 1944; Naude & Ellis, 1961; Shutler & Mesler, 1965).

Near a plane solid boundary jet formation occurs via a three-part mechanism. First, the flow field induced by the proximity of the wall causes a motion of the bubble center toward the boundary upon

spherical shape can become unstable during the final stages of collapse (Plesset & Mitchell, 1956). Neglected here were the effects of vapor and liquid viscosities and vapor density. However, the resulting trends have been shown to remain valid even with the inclusion of a small viscous effect (Prosperetti & Seminara, 1978).

A paramount problem associated with nonspherical bubble dynamics is the determination of cavity shape. It has become common to specify the bubble shape by use of an expansion in terms of spherical harmonics $Y_n^m(\theta,\phi)$,

$$S(r,\theta,\phi,t) = r - R(t) - \sum_{n,m} a_{nm}(t)\, Y_n^m(\theta,\phi) \qquad (2\text{-}10)$$

where $R(t)$ is the instantaneous average radius, $a_{nm}(t)$ is the amplitude of the spherical harmonic component of order n and degree m and,

$$S(r,\theta,\phi,t) = 0 \qquad (2\text{-}11)$$

is the equation describing the bubble surface (Plesset & Prosperetti, 1977).

The presence of a solid boundary or free surface near a vapor cavity can greatly alter the flow field created by the bubble dynamics and lead to large deviations from sphericity during collapse. The formation of a cumulative jet (Figure 2-2), directed toward a solid boundary and away from a free surface, has been inherently associated

wall motion with first-order corrections becomes,

$$\rho\left\{R\ddot{R}\left(1-\frac{2\dot{R}}{c_\infty}\right)+(3/2)\dot{R}^2\left(1-(4/3)\frac{\dot{R}}{c_\infty}\right)\right\} = \tag{2-9}$$

$$p_g\left(\frac{R_g}{R}\right)^{3\gamma}\left\{1-3\gamma\frac{\dot{R}}{c_\infty}\right\}+p_v-p_\infty-\left\{\frac{2\sigma}{R}+4\mu\frac{\dot{R}}{R}\right\}\left\{1-\frac{\dot{R}}{c_\infty}\right\}-4\mu\frac{\ddot{R}}{c_\infty}$$

where c_∞ is the speed of sound in the liquid and is assumed constant. However, it is noted that the duration of cavity collapse is so short, approximately one microsecond, that the effects of liquid compressibility and bubble contents behavior can be drastically diminished (Plesset & Prosperetti, 1977).

These analyses have all assumed the maintenance of spherical symmetry throughout the bubble growth and collapse. However, nonspherical bubble shapes have been found to result from a number of circumstances. For example, far field conditions, such as an imposed flow or the proximity of a solid boundary or free surface, may be applied to the liquid, or a cavity may simply be initiated nonspherically.

A preliminary linear stability study has been conducted for a nearly spherical drop formed by the interface between two immiscible, incompressible, inviscid fluids (Plesset, 1954). It was determined that both droplet growth and surface tension promote shape stability while droplet collapse has a destabilizing effect. A more involved analysis for a vapor cavity in an unbounded quiescent fluid revealed that the

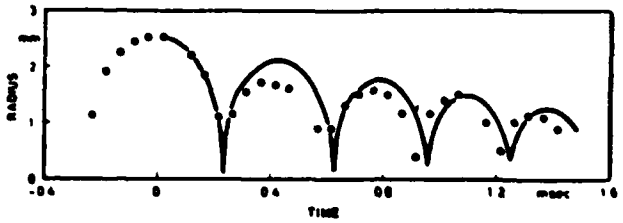

FIGURE 2-1. Comparison of experiment and RNNP theory for a spherical laser-induced model cavitation bubble in silicone oil (Lauterborn, 1974).

account for liquid compressibility resulting in,

$$R\ddot{R}\left\{1 - \frac{\dot{R}}{C}\right\} + \frac{3}{2}\dot{R}^2\left\{1 - \frac{\dot{R}}{3C}\right\} = H\left\{1 + \frac{\dot{R}}{C}\right\} + \dot{H}\,\frac{R}{C}\left\{1 - \frac{\dot{R}}{C}\right\} \qquad (2\text{-}8)$$

where H and C are the liquid enthalpy and the speed of sound at the bubble wall. Gilmore could only obtain solutions of this model based on an approximation (Kirkwood & Bethe, 1942). A full solution was later obtained numerically (Hickling & Plesset, 1964) and compared to the incompressible and approximately compressible models.

More recently, the generalized Rayleigh-Plesset equation has been extended to include both first and second-order corrections for liquid compressibility (Fujikawa & Akamatsu, 1980). The equation of bubble

questions. The quiescent fluid result is the nonlinear differential equation,

$$\rho\left\{R\ddot{R} + \frac{3}{2}\dot{R}^2\right\} = p_g\left(\frac{R_g}{R}\right)^{3\gamma} + p_v - p_\infty - \frac{2\sigma}{R} - 4\mu\frac{\dot{R}}{R} \qquad (2\text{-}6)$$

with the internal gas pressure, p_g, for a bubble of radius, R_g, given by,

$$p_g = p_\infty + \frac{2\sigma}{R_g} - p_v \qquad (2\text{-}7)$$

where p_v is the vapor pressure and γ is the ratio of specific heats (C_p/C_v) of the permanent gas. A numerical solution of this model has been obtained for representative experimental parameters (Lauterborn, 1974). The results were found to be in good agreement with experimental data on the decaying nonlinear oscillations of spherical laser-induced cavities in silicone oil (Figure 2-1). In addition, it is quite likely that the internal vapor also acts as a noncondensible gas because mass transfer (condensation) cannot keep up with bubble wall motion as the radial velocity approaches the speed of sound in the vapor (Plesset & Prosperetti, 1977; Hammitt, 1980).

Furthermore, the liquid compressibility effects can become significant if the bubble wall velocity approaches the speed of sound in the liquid. The Rayleigh equation has been successfully modified (Gilmore, 1952) to

where p_i is now the bubble interior pressure and σ is the surface tension constant. It was ultimately resolved that normal stresses across the bubble surface must be balanced, rather than pressures (Poritsky, 1952). It is only through this *boundary condition,*

$$p(R) = p_i - \frac{2\sigma}{R} - 4\mu\frac{\dot{R}}{R} \tag{2-4}$$

where $\dot{}$ denotes differentiation with respect to time, that the liquid viscosity, μ, appears. The resulting *Rayleigh-Plesset* equation,

$$\rho\left\{R\ddot{R} + \frac{3}{2}\dot{R}^2\right\} = p_i - p_\infty - \frac{2\sigma}{R} - 4\mu\frac{\dot{R}}{R} \tag{2-5}$$

is the fundamental equation governing the dynamics of a spherical cavity in an unbounded incompressible viscous liquid (Prosperetti, 1982).

A further extension of this generalized equation is the *RNNP bubble model* which includes the additional effects of gas content on bubble collapse dynamics (Rayleigh, 1917; Noltingk & Neppiras, 1950; Poritsky, 1952). Neglected in this analysis are bubble translation, heat conduction, sound radiation, gas diffusion and shape stability

consist primarily of a noncondensible gas and are therefore not associated with the cavitation phenomenon. The latter describes cavities composed almost entirely of the vapor of the surrounding liquid.

The field of vapor-bubble dynamics has been further subdivided into two categories depending on whether the surrounding liquid is in a superheated or subcooled state. This delineation results from a difference in the relative importance of thermal and inertial effects (Plesset & Prosperetti, 1977). In the case where thermal effects are important the term *boiling bubble* is used and the dynamics are controlled by the latent heat flow. For this analysis the coupling of an energy equation is essential. In the simpler case, referred to as a *cavitation bubble,* the motion is controlled primarily by liquid inertia and thermal effects can be neglected. Thus, the surprisingly accurate results of Rayleigh's highly idealized approach can be explained and understood.

It is clear that although the bubble growth (or collapse) process is initiated by pressure forces, inertia, surface tension and viscosity subsequently play important roles. The effects of surface tension can be easily included by making a simple, though not strictly correct, pressure balance across the bubble wall,

$$p(R) = p_i - \frac{2\sigma}{R} \tag{2-3}$$

cavity is,

$$\rho \left\{ R\frac{d^2R}{dt^2} + (3/2)\left(\frac{dR}{dt}\right)^2 \right\} = p(R) - p_\infty \tag{2-1}$$

where the liquid pressure at the bubble surface, p(R), the liquid pressure far from the bubble, p_∞, and the liquid density, ρ, are all assumed constant. For this *empty bubble* problem, p(R) is also equivalent to the pressure within the bubble. An important result of Rayleigh's model is an exact solution for the time, t_c, required for the complete collapse of a cavity,

$$t_c = \frac{\Gamma(5/6)}{\Gamma(1/3)}\left(\frac{3\pi\rho}{2[p_\infty - p(R)]}\right)^{\frac{1}{2}} R_0 \tag{2-2A}$$

$$\approx 0.91468\left(\frac{\rho}{p_\infty - p(R)}\right)^{\frac{1}{2}} R_0 \tag{2-2B}$$

from an initial radius R_0.

These early analyses neglected thermal effects in the formulation of governing equations. With subsequent expansion in bubble dynamics research it has become necessary to distinguish among several subgroups of bubbles within the field. A natural distinction can be made between the two subjects of *gas* and *vapor* bubbles (Plesset & Prosperetti, 1977). The former refers to bubbles whose interiors

PREVIOUS RESEARCH

1. Newtonian Analyses

The earliest analysis of bubble growth was that of Besant which was published in 1859. This highly idealized model predated the recognition of bubble dynamics as an important scientific question and was merely a mathematical exercise exploring an interesting problem. Hence, it was not until much later (Reynolds, 1894) that observations of cavitation bubble growth were first reported. Reynolds noted the formation of vapor cavities in water flowing through a constricted tube.

This nucleation of cavitation bubbles is found to occur in regions within a flowing fluid where the local pressure has fallen, in accordance with Bernoulli's equation, below the vapor pressure of the liquid. These vapor cavities are carried along by the fluid until they enter a region of increased pressure where they rapidly collapse. It was concluded by a British Admiralty commission in 1915 that the collapse of such bubbles near propellor blades was the prime mechanism of damage to the blades (Blake & Gibson, 1981).

Lord Rayleigh, associated with the British Admiralty at that time, proceeded to solve by an alternate method and apply to cavitation Besant's problem of the collapse of an empty bubble in an infinite mass of homogeneous liquid (Rayleigh, 1917). Assuming spherical symmetry and neglecting the effects of viscosity and surface tension, the resulting differential equation for the radius R(t) of the collapsing

research results of a similar nature (Hara, 1983) in an attempt to corroberate those recent model predictions. In addition, these unified conclusions from the fundamental viewpoint of non-Newtonian bubble dynamics are related, as best they can, to the applied observations of hydraulic cavitation suppression in dilute polymer solutions.

In the following sections the areas of interest specific to this research are presented individually. The pertinent background, both theoretical and experimental, is reviewed in order to lay a foundation for later sections and to place the present work in proper historical perspective. A detailed discussion of the experimental techniques and equipment is given, as is an overview of the relevant bubble modelling approaches, especially that of Hara. Results are subsequently presented and interpreted not only with respect to the fundamentals, but also with regard to the hydraulic cavitation phenomena which still elude complete explanation and serve to motivate further research. Finally, conclusions from the research results are drawn and recommendations for future work are made.

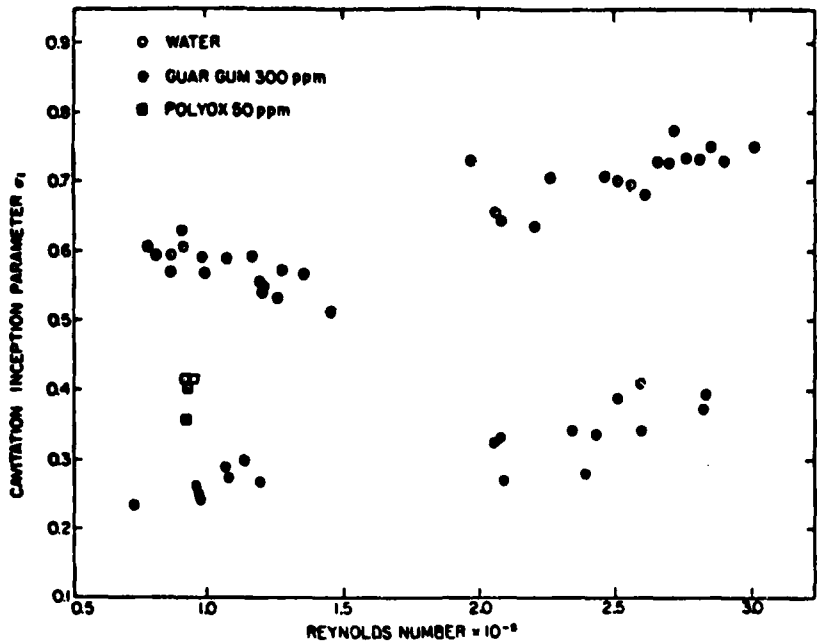

FIGURE 1-1. The effect of dilute polymer solutes on hydraulic cavitation inception (Ellis & Ting, 1974).

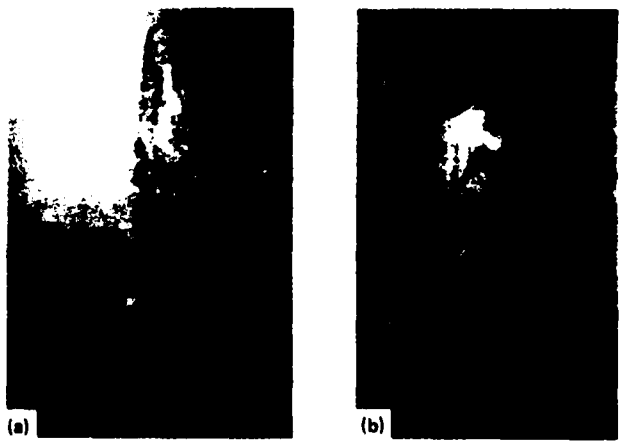

FIGURE 1-2. Comparison of cavitation appearance in (a) water and (b) dilute aqueous Polyox solution (Ting, 1978).

cavitation is significantly altered (Figure 1-2) by the presence of these *drag reducing* polymers (Brennen, 1970; Oba, Ito & Uranishi, 1978; Ting, 1978). This would seem to indicate that the alteration of flow cavitation by polymer additives is not merely a nucleation effect and that the investigation of bubble dynamics in macromolecular fluids should promote further insight concerning this phenomena.

Specifically, it has been postulated that the counterintuitive non-Newtonian behavior exhibited by even dilute polymer solutions are at least in part responsible for cavitation suppression. It is well known that the viscoelastic behavior of such macromolecular fluids can substantially alter both stress and velocity fields of a flowing system (Schowalter, 1978). Since the dynamics of spherical and especially non-spherical cavitation bubbles are intimately coupled to the fluid stresses and velocities at the bubble surface, it is anticipated that the effects of polymer additives on fluid rheology do in fact result in an alteration of the individual bubble dynamics and lead to macroscopic changes of the types reported. In particular, the case of a vapor bubble growing and collapsing while nonspherically deforming in an externally imposed flow field is expected to support the contention that cavitation modification by polymer additives is attributable to non-Newtonian bubble dynamics as well as viscoelastic nucleation.

In this light, the present study has sought to build upon previous theoretical research by experimentally investigating the growth, collapse and deformation of single model cavitation bubbles produced nonintrusively within a liquid bulk that is undergoing a well defined flow history. The experimental data are compared with theoretical

Recent investigations of cavitation bubble dynamics have been aided by improved methods of production, the most successful being the formation of single vapor bubbles by focussing short light pulses from a laser into a liquid (Lauterborn & Bolle, 1976). The precision and flexibility of this technique permits the incorporation of high-speed photography, an extremely powerful experimental tool, for data acquisition (Lauterborn, 1972). In this light, the experimental and theoretical investigations of the dynamics of *model cavitation bubbles* would appear to be of greatest help toward a fundamental understanding of the effects of hydraulic cavitation.

An intriguing aspect of this problem arises with modification of the test fluid by the addition of small amounts of *macromolecules*. It is well documented that the addition of water-soluble polymer to a cavitating system can both inhibit the onset and suppress the development of cavitation (Ellis, Waugh & Ting, 1970; Ting, 1974; Hoyt, 1976). The *incipient cavitation number*, σ_i, has been used as a measure of the state of a liquid at the onset of cavitation. It is given by,

$$\sigma_i \equiv \frac{p_\infty - p_v}{\frac{1}{2}\rho(v_\infty)^2} \tag{1-1}$$

where p_∞ is the free stream static pressure, p_v the liquid vapor pressure, ρ is the liquid density and v_∞ is the free stream velocity. Reduction of σ_i by as much as seventy percent from its value for pure water has been reported for dilute ($C \leq 1000$ wppm) aqueous polymer solutions (Figure 1-1). In addition, the physical appearance of

INTRODUCTION

The group of phenomena known collectively as *cavitation* and associated with the formation of cavities in liquids (either void, gas or vapor filled) has long occupied a position at the forefront of engineering research. The field of hydraulic cavitation, having arisen from practical needs, deals with all types of hydraulic systems including submerged propellors and bluff bodies, turbine blades, pumps and hydrofoils. The occurrence of cavitation in such systems can result in a dramatic decrease in efficiency, radiation of intense noise and even the destructive erosion of exposed parts. These observations have stimulated considerable interest in hydraulic cavitation with the ultimate goals of gaining an improved fundamental understanding of the phenomena as well as beneficially applying laboratory findings to situations of practical interest.

Experimental studies directed toward applied ends have suffered from a lack of reproducibility since the appearance of cavitation bubbles in practical systems is of a predominantly stochastic nature in both time and space. Different test facilities have reported large quantitative differences in cavitation parameters for similar tests as well as pronounced qualitative variations in the physical form of cavitation on identical test bodies (Johnsson, 1969). However, there is sufficient evidence available to confirm the generally accepted view that the macroscopic effects of cavitation can be attributed to the dynamics of individual bubbles (Knapp, 1955; Hammitt, 1963).

collapse. This leads to an initial substantial collapse of the bubble sides normal to the wall (i.e. an elongation perpendicular to the boundary). Then, this is followed by an accelerated collapse of the bubble surface farthest from the wall and the development of the observed microjet (Benjamin & Ellis, 1966; Plesset & Prosperetti, 1977; Hammitt, 1980). Complete theoretical analyses of the collapse of an empty cavity near as well as attached to a plane solid surface have been obtained numerically (Plesset & Chapman, 1971).

The validity of these calculations has been supported (Lauterborn & Bolle, 1975) by experimental data from laser-generated cavitation bubbles (Figure 2-3). In addition, these experiments confirmed quantitative predictions of maximum jet velocities between 13,000 and 18,000 cm/sec for reasonable physical parameters. An extremely important parameter governing vapor cavity collapse in the vicinity of a rigid boundary was found to be the ratio of the distance from the initial bubble center to the wall and the maximum bubble radius (Chahine & Fruman, 1979).

Other factors, such as nonspherical initial shape, have been shown to greatly affect the collapse dynamics for pure vapor bubbles in an unbounded quiescent liquid (Chapman & Plesset, 1972). These numerical analyses have revealed that upon collapse an initially prolate ellipsoid (a) leads to the formation of a pair of liquid jets while an initially oblate ellipsoid (b) results in a dumbbell form (Figure 2-4). Such highly nonspherical behavior can be predicted with or without the inclusion of liquid viscosity. Inviscid analyses have been performed by using integral methods (Voinov & Voinov, 1976) or by assuming a

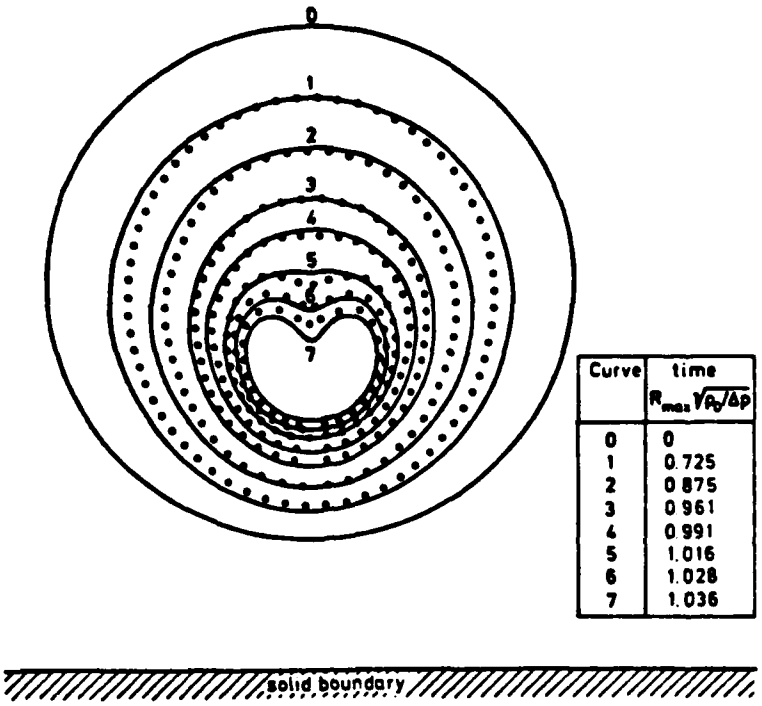

Curve	time $R_{max}\sqrt{\rho_0/\Delta p}$
0	0
1	0.725
2	0.875
3	0.961
4	0.991
5	1.016
6	1.028
7	1.036

FIGURE 2-3. Comparison of experiment and theory for bubble collapse near a solid boundary (Lauterborn & Bolle, 1975).

potential flow solution and employing Bernoulli's equation (Plesset & Chapman, 1971; Chapman & Plesset, 1972). Alternatively, the effects of viscosity have been investigated by using the Marker-and-Cell technique (Mitchell & Hammitt, 1973).

More recently, theoretical and experimental studies on the growth and collapse of a vapor cavity near a free surface have been conducted (Chahine, 1977; Blake & Gibson, 1981). Good agreement has been found between predicted and observed features including the formation

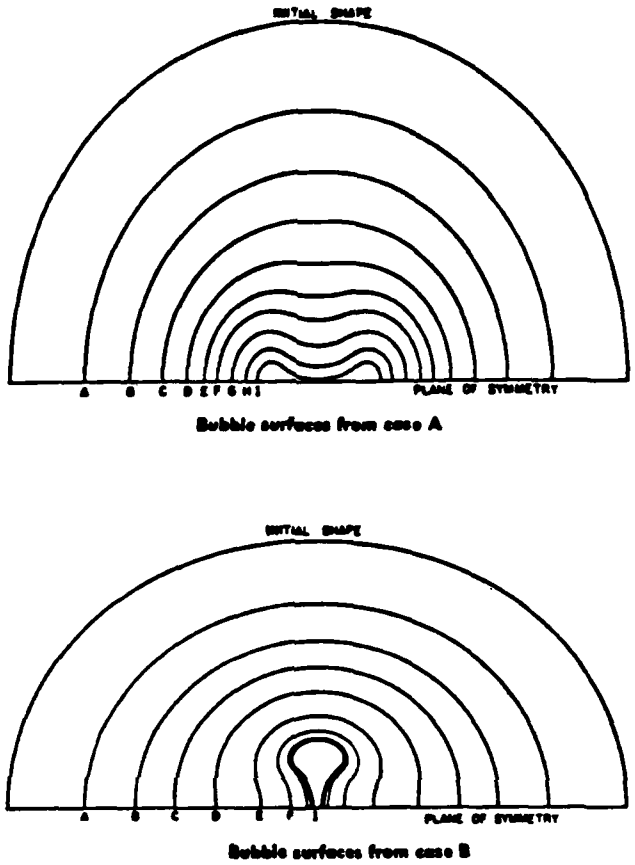

FIGURE 2-4. Theoretical collapse shapes for initially nonspherical vapor bubbles (Chapman & Plesset, 1972).

of a pronounced spike in the free surface (Figure 2-5). For this inviscid analysis, it was also determined that the same forces responsible for bubble migration during collapse were also responsible for bubble distortion. This latest work has been extended to investigate vapor bubble dynamics near flexible surfaces and deformable coatings (Gibson & Blake, 1982). The varying inertia and stiffness of

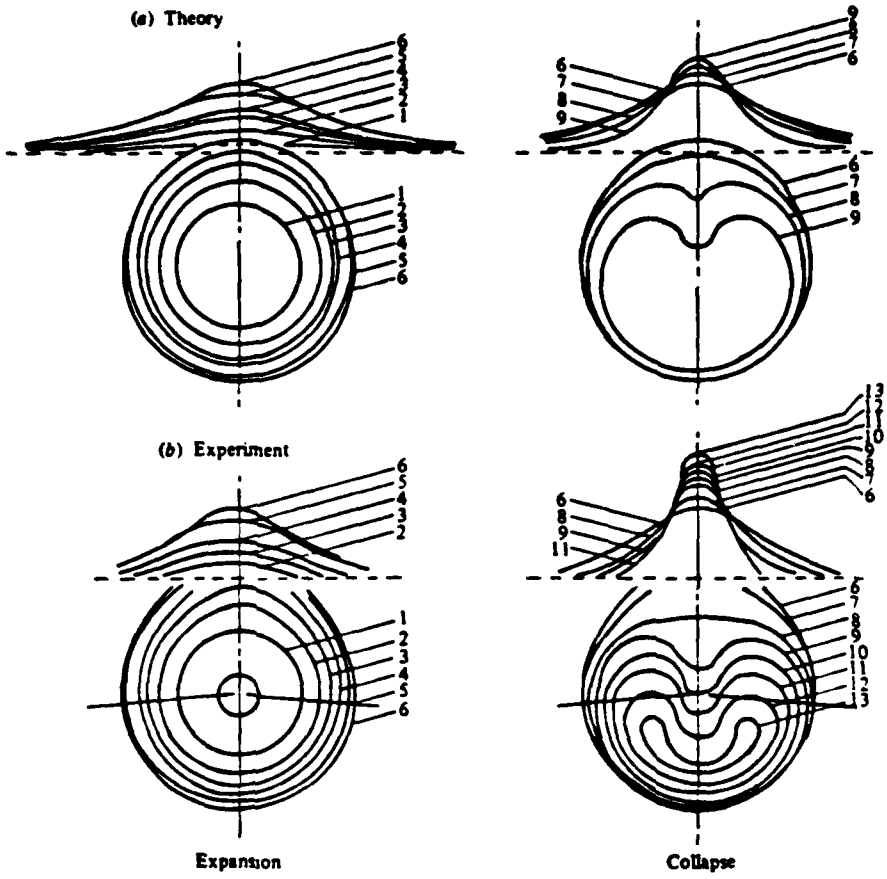

FIGURE 2-5. Comparison of experiment and theory for vapor bubble growth and collapse near a free surface (Blake & Gibson, 1981).

boundaries and coatings were used to construct a parameter space for the research. It was speculated that surface modification could lead to the repulsion of collapsing bubbles and result in the prevention of cavitation damage.

2. Non-Newtonian Analyses

Another approach toward diminishing cavitation damage has been through research on the effects of fluid modification by polymer additives. Many behaviors of these non-Newtonian fluids, such as *rod climbing* and *die swell* (Bird, Armstrong & Hassager, 1977), are considered counterintuitive with respect to the Newtonian behavior of water (Schowalter, 1978). These polymer solutions often exhibit viscoelastic behavior which can account for many of the unusual phenomena. Cavitation suppression in macromolecular fluids appears to arise from effects related to those demonstrated by situations involving free surface boundary conditions (Hoyt, 1976) or exhibiting flow field alteration (Chang & Schowalter, 1974).

To theoretically analyze a flow situation it is necessary to construct a constitutive model which can accurately predict the stress field of the system under various conditions of motion. This constitutive equation, formulated to determine the stress tensor, $\underset{\approx}{\sigma}$, must satisfy many physical constraints and be broadly applicable, yet it should be useful in a practical sense.

Under the constraint of incompressibility,

$$\underset{\sim}{\nabla} \cdot \underset{\sim}{v} = 0 \tag{2-12}$$

where $\underset{\sim}{v}$ is the velocity vector, the general constitutive equation for an

unspecified fluid is,

$$\underset{\approx}{\sigma} = -p \underset{\approx}{I} + \underset{\approx}{\tau} \tag{2-13}$$

where $\underset{\approx}{\tau}$ is the extra stress tensor. For a Newtonian fluid the extra stress tensor is given by,

$$\underset{\approx}{\tau} = \mu \left[\underset{\sim}{\nabla} \underset{\sim}{v} + (\underset{\sim}{\nabla} \underset{\sim}{v})^t \right] \tag{2-14}$$

which may be rewritten,

$$\underset{\approx}{\tau} = 2 \mu \underset{\approx}{\dot{e}} \tag{2-15}$$

where $\underset{\approx}{\dot{e}}$ is the rate of strain tensor which is defined as,

$$\underset{\approx}{\dot{e}} \equiv \tfrac{1}{2} \left[\underset{\sim}{\nabla} \underset{\sim}{v} + (\underset{\sim}{\nabla} \underset{\sim}{v})^t \right]. \tag{2-16}$$

For a purely elastic material the relationship between stress and strain is,

$$\underset{\approx}{\tau} = G_0 \underset{\approx}{e} \tag{2-17}$$

where G_s is the elastic modulus and $\underset{\approx}{e}$ is the strain tensor. The viscoelastic nature of many non-Newtonian effects suggests a combination of these two constitutive relations to describe macromolecular solutions.

The series addition of purely viscous and elastic elements describes a *Maxwell element,* whose differential constitutive equation is,

$$\underset{\approx}{\tau} + \lambda \dot{\underset{\approx}{\tau}} = \mu \dot{\underset{\approx}{e}} \tag{2-18}$$

where λ is the fluid relaxation time. In integral form the Maxwell element equation becomes,

$$\underset{\approx}{\tau}(t) = 2(\mu/\lambda) \int_0^t \exp[-(t-t')/\lambda] \, \dot{\underset{\approx}{e}}(t') \, dt' \tag{2-19}$$

which introduces the concept of a memory function over past times t'. Unfortunately, this linear viscoelastic model cannot be generally valid because it fails to satisfy the principle of material objectivity.

One approach to the formulation of constitutive equations has been the modificaton of linear viscoelastic relations to satisfy this constraint. Such manipulations require the use of specialized materially objective operators such as corotational and codeformational derivatives. Many constitutive models have been made (Bird, Armstrong & Hassager, 1977). However, the relative validity and applicability of these models vary with the particular system under consideration. Even an excellent

constitutive model can be of little or no use when the experimental flow geometry is too complex to be theoretically tractable. This is unfortunately the case in most phenomenological studies of cavitation inhibition and suppression.

The simplest system which could exhibit these effects is a spherical vapor bubble growing or collapsing in an unbounded viscoelastic fluid. Such a system has been investigated theoretically and a large elastic effect was predicted upon collapse (Fogler & Goddard, 1970). However, the range of fluid and flow conditions investigated (large Deborah number and/or large Reynolds number) was determined to be unrealistic for modelling cavitation phenomena in dilute polymer solutions. More realistic analyses of bubble growth were later performed but neither experimental nor theoretical results demonstrated any significant elastic influence (Ting & Ellis, 1974; Ting, 1975 and 1977).

For an unspecified incompressible fluid the Rayleigh-Plesset equation becomes,

$$\rho \left[R\ddot{R} + (3/2)\dot{R}^2 \right] = p_v - p_\infty - \frac{2\sigma}{R} + \int_R^\infty [\underset{\sim}{\nabla} \cdot \underset{\approx}{\tau}]_r \, dr \qquad (2\text{-}20)$$

with,

$$\int_R^\infty [\underset{\sim}{\nabla} \cdot \underset{\approx}{\tau}]_r \, dr = 3 \int_R^\infty (\tau_{rr}/r) \, dr$$

and bubble dynamics predictions for various formulations of the extra

stress tensor can be investigated. Several different fluid models have been examined and compared to one another as well as to experimental cavity collapse results (Pearson & Middleman, 1977 and 1978). It was found that as the elongation rate increased the agreement between theory and experiment worsened, especially for viscoelastic liquids.

Nonspherical bubble dynamics in a viscoelastic liquid have recently been studied in a preliminary way (Inge & Bark, 1982). This theoretical analysis of the free, damped, surface-tension-driven oscillations of a constant volume bubble revealed only small elastic changes. The effect of dissolved polymer on such motion was predicted to be mainly of a viscous nature, presumably due to the unstressed state of the surrounding fluid. The significantly more complex analyses of nonspherical bubble growth and collapse in both quiescent and flowing fluids have been recently completed (Hara, 1983; Hara & Schowalter, 1984). Good agreement between theory and experiment was reported for initially nonspherical cavities in both quiescent water and dilute aqueous polymer solutions (Figures 2-6A and 2-6B). From these experiments it was concluded that without external flow, fluid rheology (i.e. slight viscoelasticity) did not strongly influence either spherical or nonspherical cavitation bubble dynamics. However, model predictions demonstrated small but non-negligible effects for the nonspherically initiated cavities. In addition, it was seen that an external flow field which acts as the source of bubble deformation can significantly influence the system dynamics through fluid rheology (i.e. elastic memory). The flow field examined was an oscillating uniaxial extensional flow with a variable strain rate.

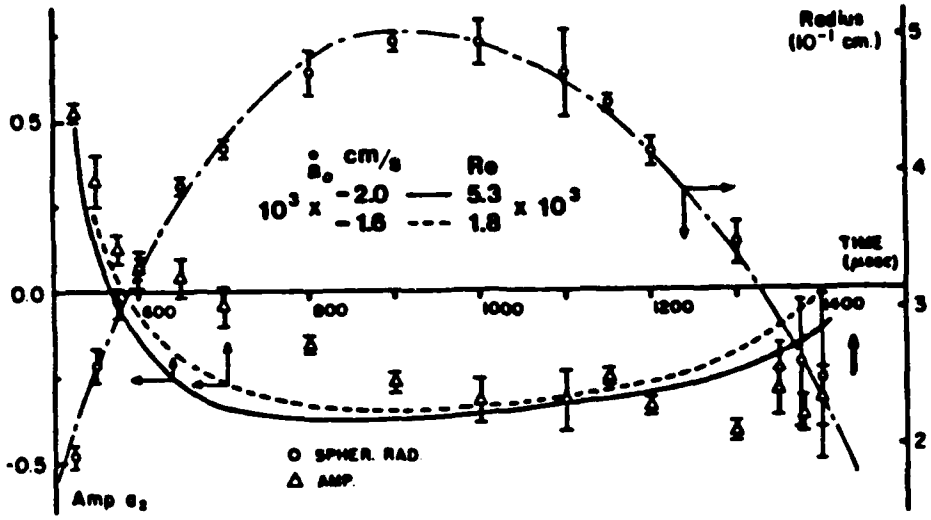

FIGURE 2-6A. Comparison of experiment and theory for nonspherically initiated model cavitation bubble dynamics in distilled water (Hara, 1983).

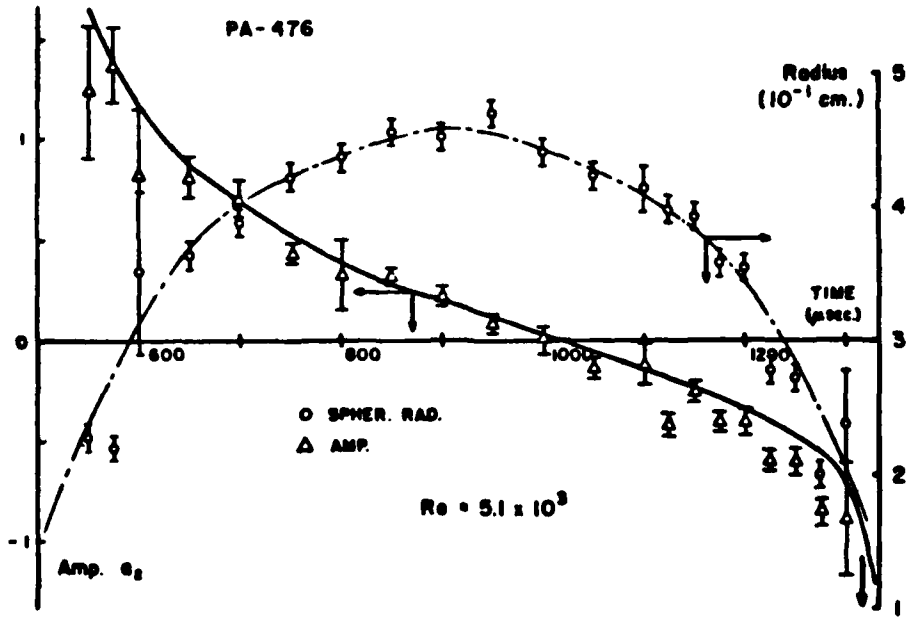

FIGURE 2-6B. Comparison of experiment and theory for nonspherically initiated model bubble dynamics in dilute aqueous polymer solution (Hara, 1983).

In particular, the contribution of viscoelasticity to the oscillating nonsphericity of a cavity of constant volume was predicted to change the amplitude of this flow induced deformation. The magnitude of this effect was found to increase with increasing *Deborah number,*

$$De \equiv \lambda/\tau \tag{2-21}$$

which is the ratio of fluid relaxation time, λ, to characteristic flow time, τ. Conditions which combined external flow and bubble collapse were shown to magnify any differences which resulted from fluid viscoelasticity. This prediction was concluded to be consistent with the idea that in contrast to a purely viscous liquid, a viscoelastic liquid would be influenced by the past history of an imposed flow.

However, the fundamental relationship between these model predictions and practical cavitation inhibition effects is still far from completely determined. Related observations by different researchers have sometimes led to opposing conclusions. For example, Oba et al. (1979) inferred from observations that bubble nonsphericity was increased by polymer additives while Chahine and Fruman (1979) attributed a stabilization of departure from bubble sphericity to the prescence of macromolecules. In the light of these contradictory reports, a related experimental study of bubble dynamics in a well defined flow field should serve to further elucidate this most interesting engineering research field.

EXPERIMENTAL TECHNIQUES

1. Previous Work

Within this field of cavitation research, very few standard experimental techniques have been developed. Research on hydraulic cavitation has been conducted with water tunnels as the primary tools. These are typically large facilities equipped to produce a closed-loop liquid flow with various controllable parameters such as flow rate or pressure

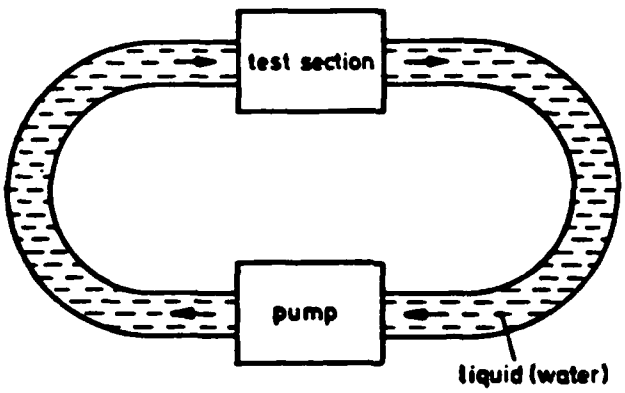

FIGURE 3-1. Schematic diagram of a closed-loop hydraulic cavitation tunnel (Lauterborn, 1974).

(Figure 3-1). The liquid is usually pumped continuously through a test section where cavitation on submerged bodies can be generated and studied. More recently, experimental investigations of single bubble dynamics have been undertaken in an effort to parallel theoretical advances, thereby improving the fundamental understanding of these

phenomena.

During the past two decades, researchers have employed only two primary techniques for cavitation bubble production. The earlier *spark-gap* method for the generation of dynamic vapor cavities has been used predominantly in studies involving either a very weak flow or no flow at all (Naude & Ellis, 1961; Benjamin & Ellis, 1966; Kling & Hammitt, 1972; Chahine & Fruman, 1979; Blake & Gibson, 1981). In this method a storage capacitor is rapidly discharged (< 1/100,000 sec) from several kilovolts across a pair of electrodes submerged in the test region. In all but the most stagnant situation, however, these protruding electrodes could have a disruptive effect on the dynamics of the flow system. As a direct consequence of this problem the technique of *laser-induced* bubble production, pioneered in the 1960s and refined in the 1970s, has been adopted for use in this research.

The effects of a laser beam in a liquid were first investigated over twenty years ago (Askar'yan et al., 1963). It was reported that the local heating within a liquid volume from a high-intensity laser pulse resulted in vapor bubble effervescence. The light source used was the unfocussed and focussed beam from a ruby laser with a pulse length of about one microsecond. With the advent of *Q-switching*, a technique for producing ultra-short (10-50 nanoseconds), ultra-high-power (100-1000 MW) light pulses from solid-state lasers, new phenomena resulting from the focussing of such pulses within liquids were observed and reported. These phenomena included stimulated Brillouin scattering, intense acoustic impulses, dielectric breakdown, high pressure shock waves and cavitation.

Initial interest was directed towards examination of the laser-induced pressure impulses within liquids (Bell & Landt, 1967; Carome et al., 1967; Roach et al., 1969). The output from a Q-switched laser was found to closely simulate an energy point source of small diameter (< 100 microns) and very high energy density (> 10^8 J/cm^3). It was further determined that this phenomenon was closely related to the dielectric breakdown of the liquid and that, in fact, shock waves were radiated from each point of breakdown within the liquid. The results of several investigations supported the idea that at sufficiently high output energy a focussed laser pulse could consistently lead to dielectric breakdown, plasma formation and vapor cavity nucleation at the focal point within the liquid (Stamberg & Gillespie, 1965; Barnes & Rieckoff, 1968; Singurel, 1969; Felix & Ellis, 1971).

Despite these advances, the detailed analysis of laser-induced cavitation bubble dynamics was only later made possible by the application of high-speed photography to record the events (Lauterborn, 1972). At that time both rotating drum and rotating mirror cameras were used to study laser-induced cavity formation, growth, collapse and rebound at framing rates of up to one million pictures per second. It was reported that laser output energies of 0.1 to 1.0 joules in pulses of duration 30 to 50 nanoseconds were found to produce cavities of maximum radius 0.1 to 0.2 centimeters with total lifetimes of 0.5 to 1.0 milliseconds. Experimental techniques were further refined as the number and shape of the bubbles produced were found to depend on the focal length of the single focussing lens. Reproducible formation of spherical vapor bubbles, essential to the present investigation of non-Newtonian effects, was accomplished by

with the four boundary conditions,

$$v_\theta(R_i,z) = 0$$

$$v_\theta(R_o,z) = 2\pi\omega R_o$$

$$v_\theta(r,0) = 0$$

$$v_\theta(r,h) = 2\pi\omega r$$

was solved using an iterative finite difference scheme. The influence of the ratio of gap height to gap width (h/g) was of particular interest. The results showed that a value for this aspect ratio of at least unity is required to insure a sufficiently large region of nearly fully developed flow.

The cylindrical Couette device was subsequently designed, constructed and modified several times before the final configuration was reached (Figure 3-6). The outer shell of the rotating cylinder was machined from aluminum and the shafting and bearings were stainless steel. The flanged bushing connecting the rotor top to the shafting was machined from brass. With these exceptions the primary material of construction was PMMA. General system specifications are listed in Table 3-3. Interchangeable stationary inner cylinders allowed two distinct gap sizes of 5.4 and 9.2 cm with acceptable aspect ratios of 1.76 and 1.04 respectively. The lens mount was situated so the laser pulse entered from below and was focussed upward into the test region. The system was mounted on a nearly cubic steel channel lattice which

turbulent flow velocity profiles for several values of the ratio of cylinder radii (κ) have been measured experimentally (Wendt, 1933). These measurements indicated that the turbulent velocity was linearly dependent on the radial position in the annular region, except near the walls (due to turbulent boundary layer effects). Also, for sufficiently small values of the cylinder ratio ($\kappa \leq 0.8$), laminar and turbulent shear rates near the center of the annulus were approximately equal (to within ± 10%).

Wendt (1933) also studied the changes in the turbulent velocity profile which resulted from different cylindrical end effects (rotating bottom, stationary bottom or half rotating/half stationary bottom). While these different conditions led to significant differences in the magnitude of the fluid velocity (± 10-25%), the magnitude of the turbulent shear rate near the center of the annular test region was virtually unchanged (to within ± 5%). To determine the extent to which end effects, both top and bottom, modify the ideal laminar velocity profile, an approximation of the exact Newtonian flow field in the annular region was obtained. The θ-component of the equation of motion,

$$\frac{\partial}{\partial r}\left\{\frac{1}{r}\frac{\partial}{\partial r}\left(r\, v_\theta(r,z)\right)\right\} + \frac{\partial^2 v_\theta(r,z)}{\partial z^2} = 0 \qquad (3\text{-}7)$$

profile, v_θ, is a function of radial position, r, alone, and is given by,

$$v_\theta(r) = \frac{2\pi\omega}{r}\left(\frac{r^2 - \kappa^2 R^2}{1 - \kappa^2}\right) \tag{3-4}$$

where ω is the rotation rate in revolutions per second, R is the radius of the outer (rotating) cylinder in centimeters and κ is the ratio of inner cylinder radius to outer cylinder radius. For these conditions and geometry, the radial shear rate, $\dot{\gamma}$, is defined as,

$$\dot{\gamma} \equiv \frac{\tau_{r\theta}}{\mu} = r\frac{d}{dr}\left(\frac{v_\theta(r)}{r}\right) \tag{3-5}$$

and is given by the expression,

$$\dot{\gamma} = 4\pi\omega\left(\frac{R^2}{r^2}\right)\left(\frac{\kappa^2}{1 - \kappa^2}\right) \tag{3-6}$$

where $\tau_{r\theta}$ is the shear stress and μ is the fluid viscosity. Therefore for a fixed geometry (gap ratio and outer radius) this laminar shear rate is a function of radial position and, of course, rotation rate. The maximum shear rate variation over the diameter of a typical bubble ($0 \leq R(cm) \leq 0.5$) was determined to be (± 2-6%) depending on the maximum size of the particular bubble. For this geometry, the

flow is strongly stabilized by centrifugal forces. The stability of this system has been thoroughly studied both theoretically (linear perturbation analyses) and experimentally (Schlichting, 1968).

> In the case of steady-state flow in the annulus between two concentric cylinders with the inner cylinder at rest and the outer cylinder rotating about its axis, no limit of stability can exist in analogy with Couette flow (Re(crit) = ∞)....
>
> A further confirmation of these theoretical results was recently supplied by F. Schultz-Grunow ... who was able to prove quite rigorously that the flow between two concentric cylinders of which the outer rotates and the inner is at rest is completely stable....
>
> It was established that although transition does occur during the starting process, the flow reverts to a laminar pattern when a steady-state has been established....
>
> It has thus been confirmed that the persistence of turbulence into the steady-state regime was caused by imperfections in the geometrical shape and did not signify that the theory had failed. (Schlichting, 1968)

In addition, the criteria for the transition from laminar to turbulent flow during an impulsive starting process have been investigated and reported (Bird, Stewart & Lightfoot, 1960; Schlichting, 1968).

Neglecting end effects, the unidirectional laminar Newtonian velocity

From these theoretical predictions, an expression for the magnitude of this steady-state deformation was determined. The nonsphericity, expressed as the ratio of bubble oscillation amplitude (A) to the equivalent spherical radius (R) was given by,

$$(A/R) \approx \frac{4\mu R\dot{\varepsilon}}{\sigma} \tag{3-3}$$

where μ is the liquid viscosity in poise, $\dot{\varepsilon}$ is the strain rate in sec^{-1} and σ is the liquid surface tension in dyne/cm. These estimates indicated that strain (or shear) rates of 100-500 sec^{-1} would be required to produce deformation ratios (A/R) of 0.10-0.25 in bubbles of maximum radius 0.2-0.5 cm in slightly to moderately viscous fluids ($\mu \approx$ 0.01-0.20 poise). Preliminary experimental work on spherical bubble dynamics in quiescent fluids indicated that a free distance (gap size) of 5-10 cm would be sufficient for the undisturbed growth and collapse of typical bubbles.

Stability of laminar flow was investigated for a four-roller apparatus (Fuller & Leal, 1981) and a *cross-flow cell* (Scrivner et al., 1979). Significant flow stability uncertainties inherent to these systems, over the deformation rates of interest, finally prompted the decision to adopt a cylindrical Couette experimental configuration. This concentric cylinder geometry is known to produce an approximation to planar shear flow for small gap sizes relative to the outer cylinder radius (Bird, Stewart & Lightfoot, 1960). With the outer cylinder rotating, even for the large relative gap sizes required for the present research, laminar

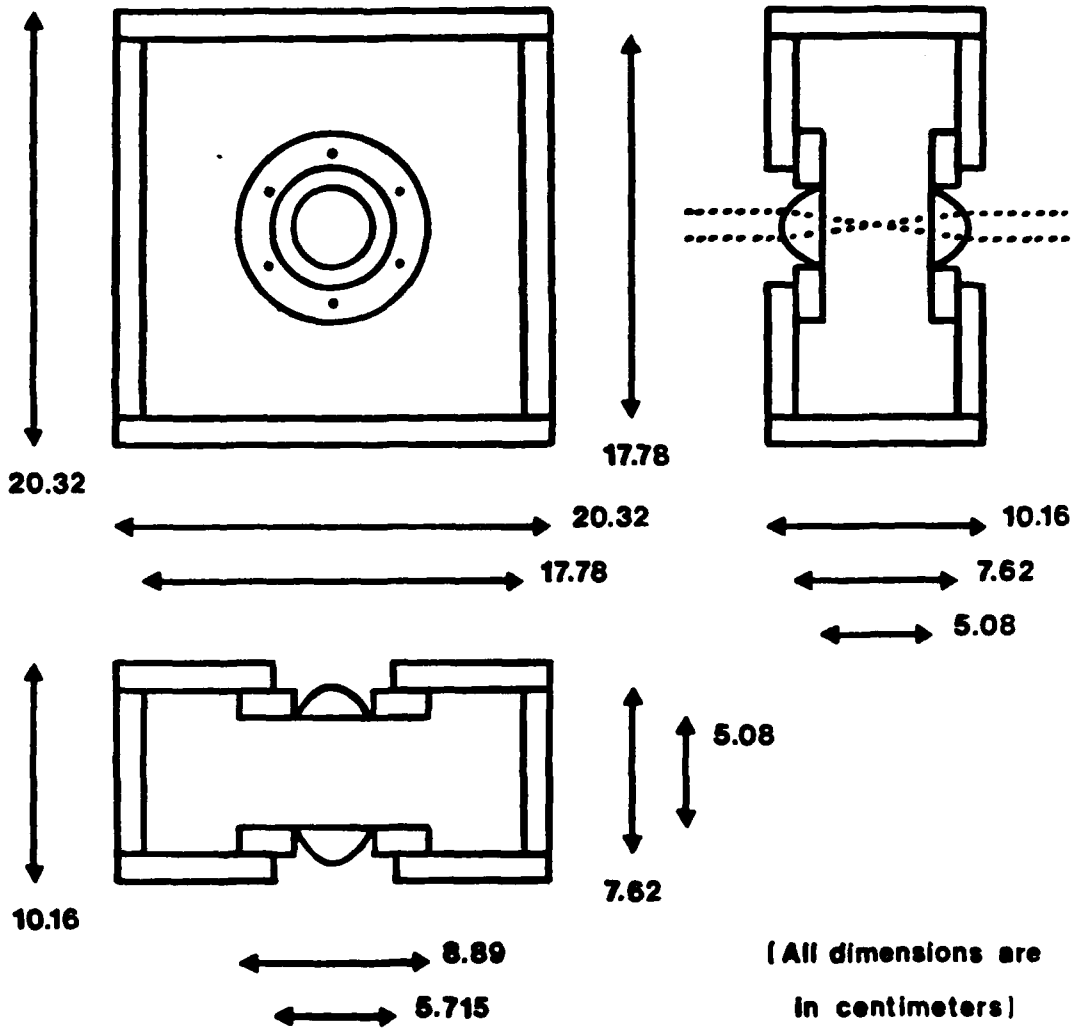

FIGURE 3-5. Energy measurment test cell dimensions.

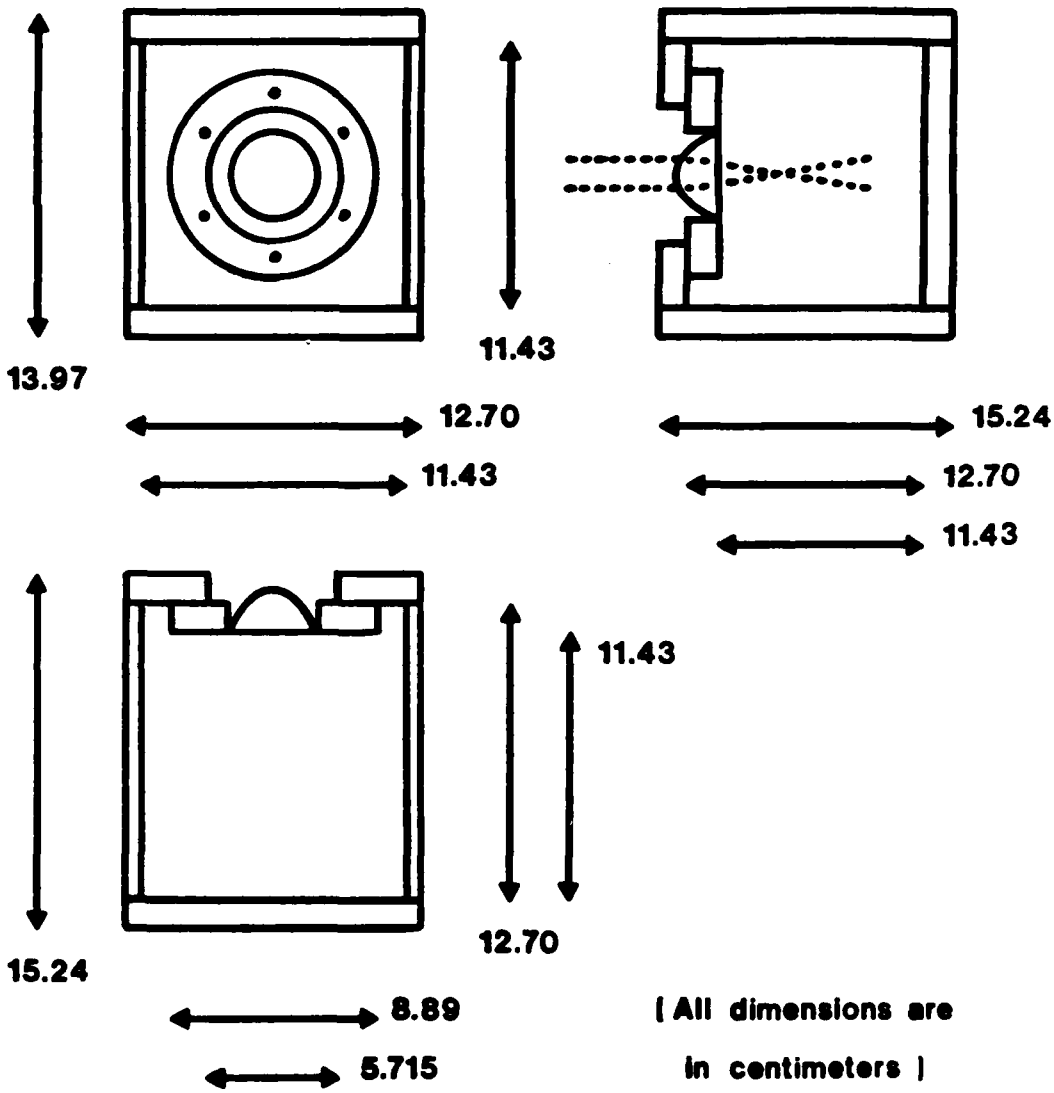

FIGURE 3-4. Quiescent fluid test cell dimensions.

density in the focal region was extremely high and as a result, electronic absorption, dielectric breakdown and bubble nucleation proceeded almost instantaneously (< 1 microsecond).

The simplest of the quiescent fluid cells was a polymethylmethacrylate (PMMA) cuvette with a single lens mount and a removable top (Figure 3-4). The interior of the chamber approximated a cube of dimension 11.5 centimeters. In this cell, spherical and nonspherical bubble dynamics in quiescent liquids were investigated. The second cell was designed to accommodate two lenses situated on opposite walls (Figure 3-5). In this coaxial configuration the laser pulse could be focussed and then collimated by matching the focal lengths of the lens to their separation. The energy of the emerging beam could be measured and referenced to reveal the energy used in the nucleation process (see Appendix A).

The constraints of the flow system dictated the choice of *cylindrical Couette* geometry over a *four-roller* or *belt-type* apparatus. These requirements included the production of a stable laminar flow field of sufficient strength to induce bubble deformations large enough for photographic analysis. In addition, enough free volume was necessary to allow bubble growth and collapse with negligible wall effects. Finally, temperature variation due to viscous dissipation had to be negligibly small.

To determine the system size, estimates of the effects of flow strength and liquid properties on bubble deformation were made. Numerical simulations based on Hara's model (1983) of a constant volume bubble deforming in a uniaxial extensional flow field were performed.

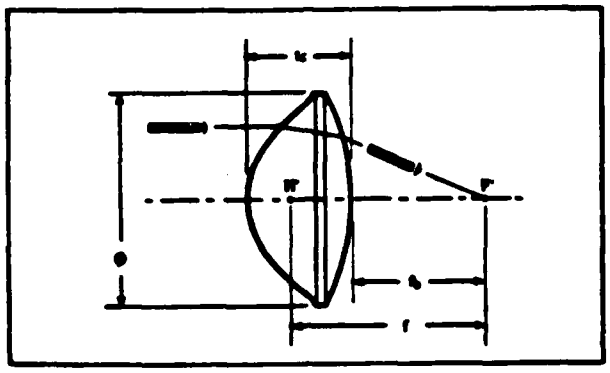

FIGURE 3-3. Typical aspheric laser focussing lens (Melles Griot, 1981).

For multimode laser operation the spot radius, s, is given by,

$$s = f' \tan(\theta) \approx f'\theta \approx n'f\theta \tag{3-1}$$

where f is the lens focal length in air, n' and f' are the refractive index and lens focal length, respectively, in the medium of interest and θ is the beam divergence which is small (see Table 3-1). The spot depth, d, is then given by,

$$d = \frac{2(sf')}{D} = \frac{2(n'f)^2\theta}{D} \tag{3-2}$$

where D is the beam diameter. With a small spot size, the energy

laser focussing lenses :

Melles Griot (1981) plano-back aspheric lenses with anti-reflective MgF_2 coating

product no.	f.l. (air)	diameter
01-LAG-002/066	12.0 mm	17.0 mm
01-LAG-005/066	18.0 mm	24.0 mm
01-LAG-117/066	25.0 mm	32.5 mm
01-LAG-007/066	26.5 mm	30.0 mm
01-LAG-010/066	33.0 mm	52.0 mm
01-LAG-012/066	34.5 mm	38.0 mm
01-LAG-013/066	35.0 mm	50.0 mm
01-LAG-123/066	37.0 mm	52.0 mm
01-LAG-011/066	42.0 mm	45.0 mm

TABLE 3-2. Laser focussing lens specifications.

In order to accomplish several specific experimental objectives, two quiescent fluid cells and a cylindrical Couette flow system were constructed. A design factor common to all three was the interchangeable flush mounting on an external wall of a single aspheric lens. These short focal length converging lenses (Table 3-2) were used to precisely focus the laser light into a small spot (Figure 3-3).

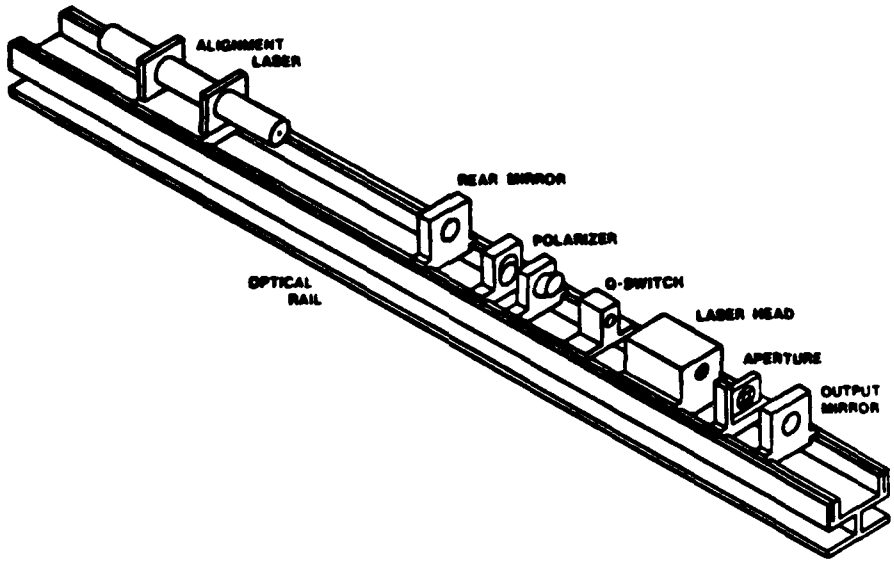

FIGURE 3-2. Optical components of the ruby laser system (Apollo Lasers).

The maximum output energy was about 1.5 joules and could be varied by two independent means. Coarse attenuation was achieved by the use of absorptive neutral density filters and fine adjustments were made by small changes in the charge voltage of the capacitor bank supplying the laser flashlamp. The output beam had a diameter of about one centimeter, which could be focussed down to about 100 microns, and a duration of 10 to 30 nanoseconds. The refrigerated bath circulator maintained a constant laser head temperature of 20 ± 0.1 C for improved *shot-to-shot* reproducibility. A low power helium-neon laser was used to align the optical components which were mounted on a stress-relieved aluminum rail.

pulsed laser :

Apollo Lasers Model 5H (No. 31002)
Q-swithched ruby laser system

maximum energy :	1.5 J
pulse width :	10-30 nsec
peak power :	100 MW
beam divergence :	3-5 mrad

alignment laser :

Hughes Model 3225H-PC
5mW polarized HeNe laser

Hughes Model 4020(F)
laser power supply

refrigerated circulating bath :

Neslab RTE-4

heating capacity :	800 W
cooling capacity :	400 W
reservoir volume :	5 ℓ
circulation rate :	13 ℓ/min

absorptive filters :

Schot glass neutral density filters

filter	thickness	transmittance
NG5-1	1 mm	55%
NG4-2	2 mm	15%
NG4-3	3 mm	6%

TABLE 3-1. Experimental laser system components.

reproducible nonspherical vapor cavities in a quiescent liquid (Hara, 1983).

2. Experimental Apparatus

The primary goal of this experimental program has been to investigate the effects of polymer additives on the growth, collapse and simultaneous deformation of model cavitation bubbles in a well defined flow field. Thus the design criteria for the experimental system were quite clear-cut and yet relatively flexible. Reproducible bubbles of variable size were to be optically induced and photographically recorded nonintrusively within a system of fairly strong straining or shearing flow.

The experimental equipment for this research can be neatly divided into four subsystems, each with its own set of performance criteria. These four include the laser system for bubble production, the test cells and flow system, the photographic systems for data acquisition and the associated electronic systems. The components of each subsystem were either designed and constructed or specified and purchased, modified as was necessary and ultimately adapted for integrated operation.

The focus of the research apparatus was the laser subsystem which was comprised of the laser components, the refrigerated bath circulator and the laser power supply. The specifications of this subsystem are given in Table 3-1. The laser system consisted of a pulsed ruby oscillator which was actively Q-switched by a Pockels cell (Figure 3-2).

using a submerged lens of short focal length (Lauterborn, 1974). In addition, slightly nonspherical bubbles, oblong bubbles and multi-bubble systems could be produced, although not repeatably (Lauterborn, 1976).

Upon initial examination, this vapor bubble formation from a high-energy plasma at the nucleation site would seem to necessitate the inclusion of an energy (or temperature) equation for the liquid in any realistic modelling effort. However, as Lauterborn (1972) has reported, these laser-induced spherical cavities in water realize Rayleigh's isothermal empty-bubble model. This somewhat unexpected agreement is due to the extremely fast nature of the nucleation and initial bubble growth phenomena. Initial vapor expansion proceeds so quickly (without time for heat transfer to the surrounding fluid) that the bubble contents rapidly cool to near ambient temperature. Thus, Lauterborn's observation leads to the conclusions that (a) for these laser-induced bubbles, inertial effects dominate thermal effects and that (b) these laser-induced cavities realistically model actual cavitation bubbles.

Laser-induced or optical cavitation, as it has come to be known, has been subsequently used in conjunction with ultra-high-speed photography and high-speed holography to examine the dynamics of cavitation bubbles in a myriad of experimental circumstances such as in a highly viscous liquid, near a solid boundary or a free surface and interacting with other bubbles (Lauterborn & Bolle, 1975; Lauterborn & Ebeling, 1977; Lauterborn, 1979). Most recently, optical cavitation has been used to investigate the effects of fluid viscoelasticity on

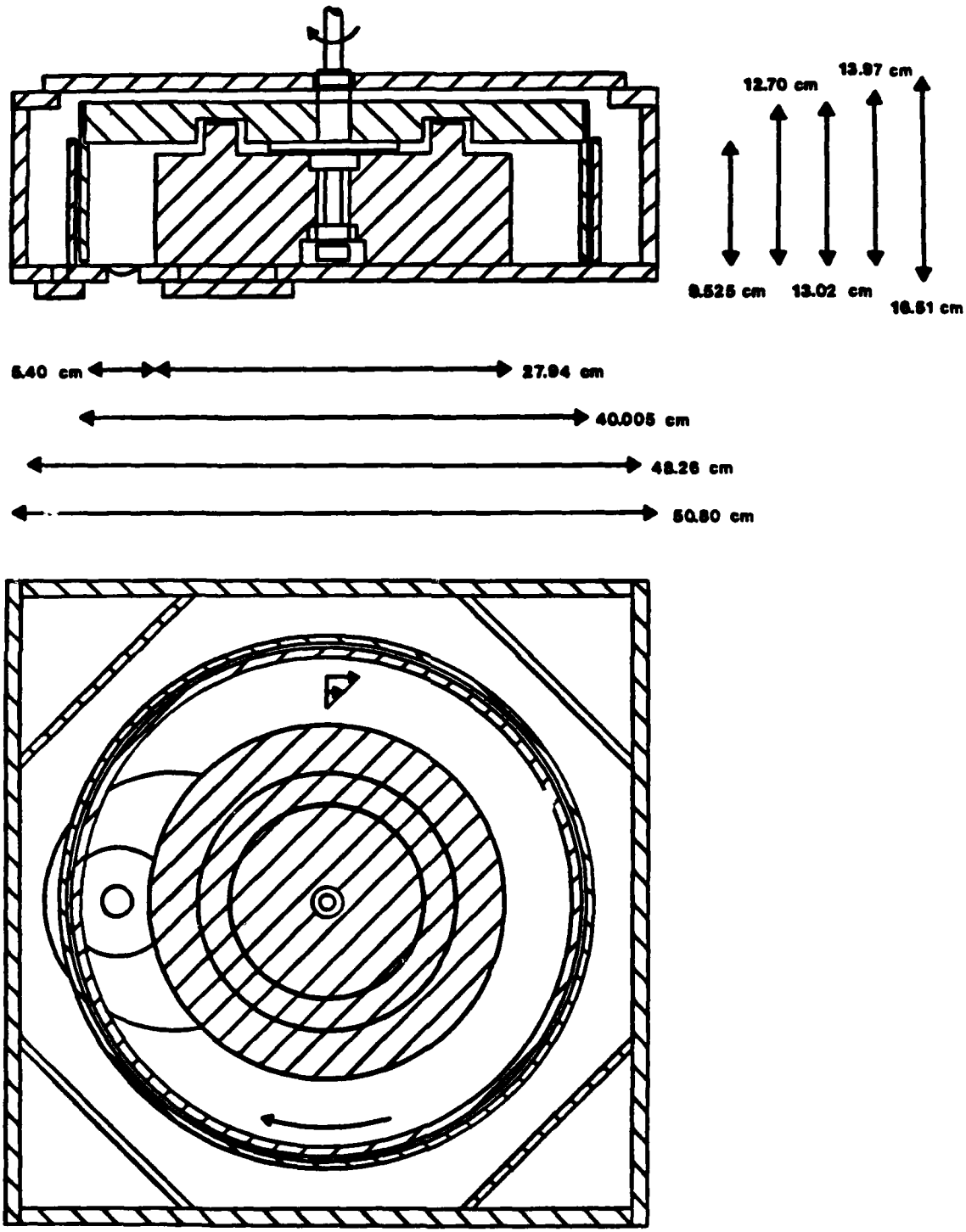

FIGURE 3-6. Cylindrical Couette flow system dimensions.

test section :

outer radius :	R_o = 19.37 cm
inner radius :	R_i = 13.97, (10.16) cm
gap ratio :	$\kappa \equiv (R_i/R_o)$
	= 0.72, (0.52)
gap width :	g = 5.4, (9.2) cm
gap height :	h = 9.525 cm
aspect ratio :	(h/g) ≈ 1.76, (1.04)

containment tank :

horizontal dimension :	S = 48.90 cm
vertical dimension :	H = 13.97 cm
fluid volume :	V ≈ 16.5, (19.5) ℓ

lens mounts :

focal radius :	r_f ≈ 16.51, (14.605) cm

drive systems :

Leyland Faraday M278
1 hp AC electric motor

Staco Energy Products 3PN1510
0 - 120/140 V variable autotransformer

General Electric 184T
5 hp 3-phase AC electric motor

General Electric AFTROL II
variable frequency drive controller

TABLE 3-3. Cylindrical Couette flow system specifications.

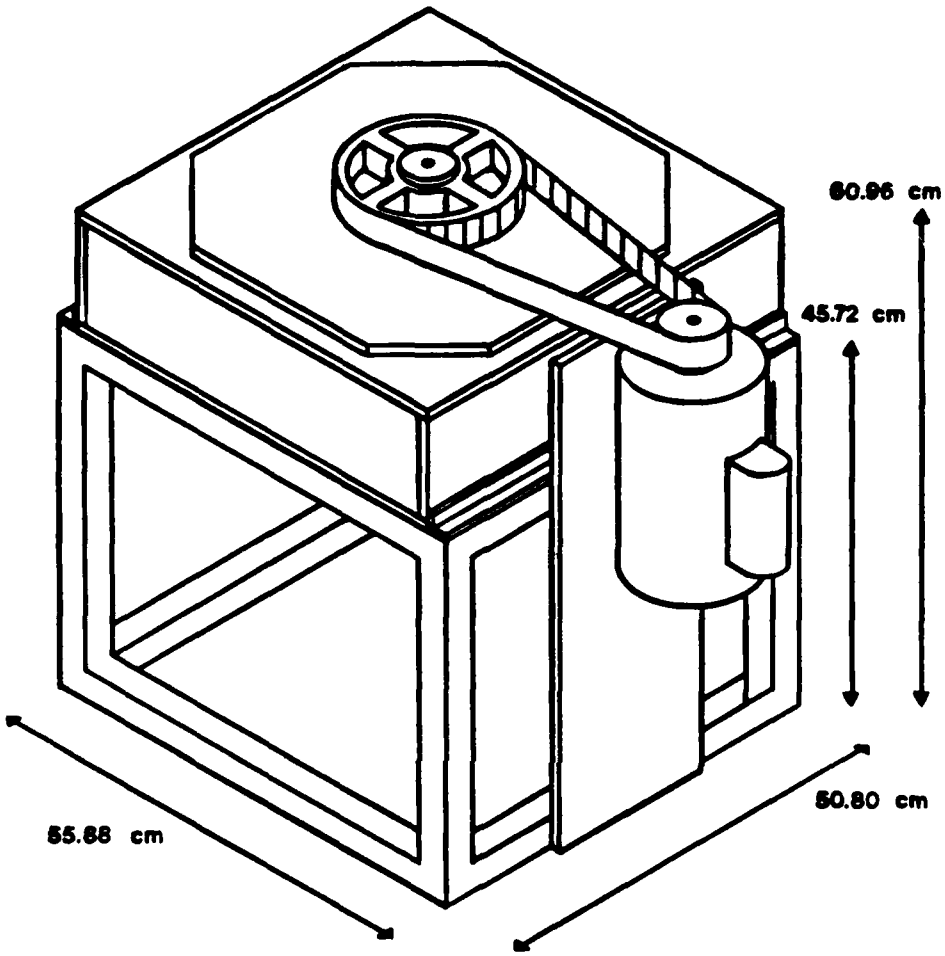

FIGURE 3-7. Flow system support lattice and positive drive apparatus.

also supported the drive motor (Figure 3-7). Rotation of the outer cylinder was accomplished by a positive drive system comprised of timing gears and belts. Rotation speed regulation and gradual start-up were achieved by supplying power to the motor from a variable frequency drive controller. Pertinent experimental system calculations

g(cm)	ω(rpm)	v_w(cm/s)	$\dot{\gamma}$(sec^{-1})	μ(poise)	P(hp)	ΔT(C/min)
-	0	0	0	-	0.00	0.00
9.20	360	750	85	0.01	0.06	-
5.40	360	750	105	0.01	0.06	-
"	"	"	"	0.06	0.25	0.02
"	"	"	"	0.16	0.40	0.05
"	"	"	"	1.05	0.85	0.29
5.40	480	1000	140	0.01	0.13	0.005
"	"	"	"	0.06	0.50	0.03
"	"	"	"	0.16	0.80	0.08
5.40	575	1200	170	0.01	0.25	0.01
"	"	"	"	0.06	1.00	0.05
"	"	"	"	0.16	1.60	0.12
5.40	720	1500	210	0.01	0.60	0.01
5.40	865	1800	255	0.01	1.00	0.015

TABLE 3-4. Sample flow system calculations.

are presented in Table 3-4.

Due to the extremely rapid nature of the phenomena under investigation, high-speed photographic techniques were required for data acquisition. Nominal experimental conditions were found to result in cavities whose total lifetime, including rebounds, was about one to two milliseconds. The duration of the period of greatest interest, from initiation to the first collapse, was much shorter, in the range of 500 to 1000 microseconds depending on bubble size and fluid properties.

Two distinct photographic systems were employed for data acquisition. The first was a single-exposure system of high resolution, while the second was a high-speed framing system. The single exposure system, which relied heavily on event reproducibility was used primarily in preliminary studies of spherical bubble dynamics in quiescent fluids. The high-speed system was used for the less repeatable experiments involving bubble deformation, flow system dynamics and bubble energy measurements.

The single exposure system consisted primarily of an SLR camera and a short-duration high-intensity flashlamp (Table 3-5). By synchronizing the flashlamp to the laser output pulse through the delay generator and maintaining the camera in an alert state, it was possible to record a single photograph of each laser induced bubble at any point in its lifetime. Thus, by systematically varying the delay period, a complete history of an average bubble could be assembled from the single exposures of individual bubbles. Reproducibility from shot-to-shot was therefore an essential feature of this experimental scheme. A typical exposure time was roughly one microsecond and regular

SLR camera :

Hasselblad Model 500C

w/Zeiss 80 mm planar f/2.8 lens

2½"-8" bellows extension

55 mm extension tubes (2)

Polaroid film magazine 100

flash unit :

EG&G Electro-Optics

FX-279 xenon flashbulb

FY-611 trigger module

PS-302 power supply

Melles Griot

02-RPM-008 paraboloidal reflector

02-REM-003 ellipsoidal reflector

01-LFP-035, 037 and 041 fresnel lenses

film :

Polaroid 667 (ASA 3000)

TABLE 3-5. Single-exposure photographic system components.

photograph intervals varied from 20 to 50 microseconds.

The principal components of the high-speed photographic system were the framing camera and the electronic flash unit (Table 3-6). The Dynafax unit, a rotating drum camera (Figure 3-8), recorded 224 frames (7.50 mm x 10.0 mm) on a single 860 mm length of standard 35mm film at a rate adjustable from 200 to 35,000 frames per second (fps). Once the camera was brought up to speed it remained alert until the film was exposed by the variable duration (8.60, 11.15, 14.85 or 22.35 msec) square wave pulse from the xenon flashlamp. This flash unit was also linked electronically to the the laser output for precise synchronization. As with the single exposure system, the transient vapor cavities were backlit and appeared dark against a light background in printed exposures.

As previously mentioned, synchronization of flash pulses to experimental events was accomplished and varied through the use of a digital delay generator (Table 3-7). Typical delay times ranged from 0 to 10 milliseconds with resolutions of 0.1 to 1.0 microseconds. Laser bubble energy measurements were made by using a laser calorimeter (Table 3-7). This unit was used to record energies of 0-2 joules with a sensitivity of 1-10 millijoules. In addition, two electronic trigger devices, one for each flashlamp, were constructed and used to couple the delay generator to the backlighting systems.

high-speed framing camera :

Cordin Dynafax Model 350

w/Canon 18-108 mm f/2.5 zoom lens

Fujinon 105 mm f/4.5 close-up lens

40 mm, ½" and ¼" extension tubes

electronic flash unit :

Cordin Model 357

maximum output : 10^6 pbcp

minimum pulse : 8.6 msec

Melles Griot (see Table 3-5)

08-MLB-003 high-energy laser mirror

ellipsoidal and paraboloidal reflectors

acrylic fresnel lenses

film :

Eastman Kodak

Technical Pan 2415 (ASA 125)

TRI-X Pan (ASA 400)

2475 Recording (ASA 1250)

TABLE 3-6. High-speed photographic system components.

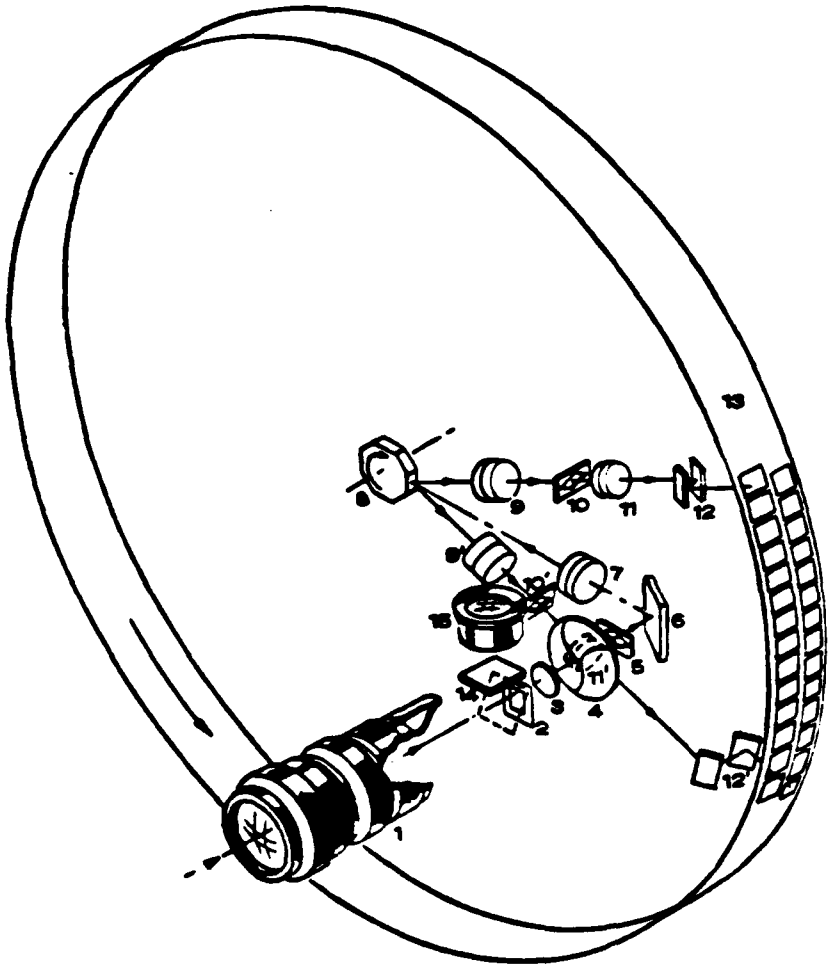

1. Objective Lens
2. Mask
3. Field Lens
4. Capping Shutter
5. Entrance Diamond Stop
6. Entrance Relay Mirror
7. Entrance Relay Lens
8. Rotating Mirror
9. Collimating Relay Lens
10. Exit Diamond Stop
11. Imaging Relay Lens
12. Exit Relay Mirrors
13. Film
14. Focusing Mirror and Ground Glass
15. Focusing Eyepiece

FIGURE 3-8. Optical schematic diagram of the high-speed framing camera (Cordin, 1965).

digital delay generator :

Berkeley Nucleonics Model 7010

delay ranges:

0-10 ms ± 100 ns

0-100 ms ± 1 μs

0-1 sec ± 10 μs

0-10 sec ± 100 μs

0-100 sec ± 1 ms

laser calorimeter :

Apollo Lasers digital energy meter

energy ranges:

0-200 mJ ± 1 mJ

0-2 J ± 10 mJ

0-20 J ± 100 mJ

TABLE 3-7. Additional experimental electronic components.

EXPERIMENTAL RESULTS AND DISCUSSION

1. Preliminary Experiments

Initial experimentation with laser-induced cavitation in liquids was focussed on the dynamics of reproducible spherical bubbles in quiescent viscous and viscoelastic fluids. For these early tests, the quiescent fluid cell and single-exposure photographic system were employed in the configuration shown in Figure 4-1. A typical sequence of experimental events was as follows :

(a) preparation

- test cell filled with fluid of interest
- camera and flashlamp aligned and focussed
- camera loaded and shutter cocked
- delay period and laser voltage set

(b) experimentation (firing sequence)

- laser capacitor bank charged
- camera shutter opened
- main trigger fired
  (laser and flashlamp fired in synch)

(c) post-experimentation

- camera shutter closed
- Polaroid photogaph developed

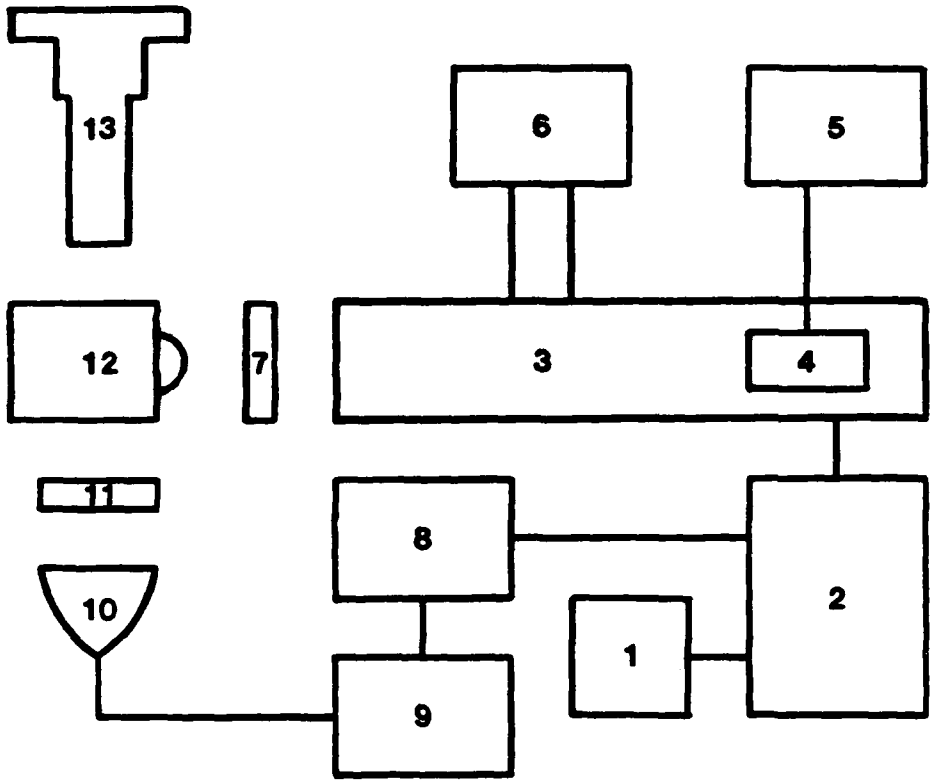

1 SYSTEM TRIGGER
2 LASER POWER SUPPLY
3 RUBY LASER
4 HeNe LASER
5 HeNe LASER
6 COOLING SYSTEM
7 LASER FILTER
8 DELAY GENERATOR
9 FLASH POWER SUPPLY
10 FLASHLAMP HEAD
11 FRESNEL LENS AND/OR FLASH DIFFUSER
12 QUIESCENT TEST CELL
13 SLR CAMERA

FIGURE 4-1. Schematic diagram of the experimental configuration for single-exposure quiescent fluid tests.

From several such experiments, with constant laser output and varying delay periods, complete bubble lifetime sequences (from initiation to collapse) were assembled. Two typical sequences of model cavitation bubbles in distilled water (DH2O) are shown in Figures 4-2A and 4-2B.

From these tests, the results of previous workers (Lauterborn, 1972; et al.) regarding the dynamics of spherical laser-induced bubbles in quiescent Newtonian fluids were confirmed. It had been concluded that these spherical cavities closely follow the dynamic behavior predicted by the somewhat idealized Rayleigh-Plesset equation (see Chapters 2 and 3). In particular, the linear theoretical relationship between bubble collapse time, t_c, and maximum bubble size, R_0, predicted by Rayleigh's original analysis (equation 2-2) was again substantiated by these experimental data. For example,

$$(t_c/R_0) = (225/0.23) \qquad \text{(Figure 4-2A)}$$
$$\approx 978.3\ \mu s/cm$$

$$= (350/0.36) \qquad \text{(Figure 4-2B)}$$
$$\approx 972.2\ \mu s/cm$$

The success of that inviscid analysis demonstrates the dominance of inertial effects over viscous effects in such phenomena. Furthermore, the addition of dilute polymer solutes (polyacrylamide : $0 \leq C(wppm) \leq 1000$) was found to have only a minimal effect on spherical bubble dynamics in an otherwise quiescent fluid. This result had been previously predicted (Ting, 1975) and also experimentally

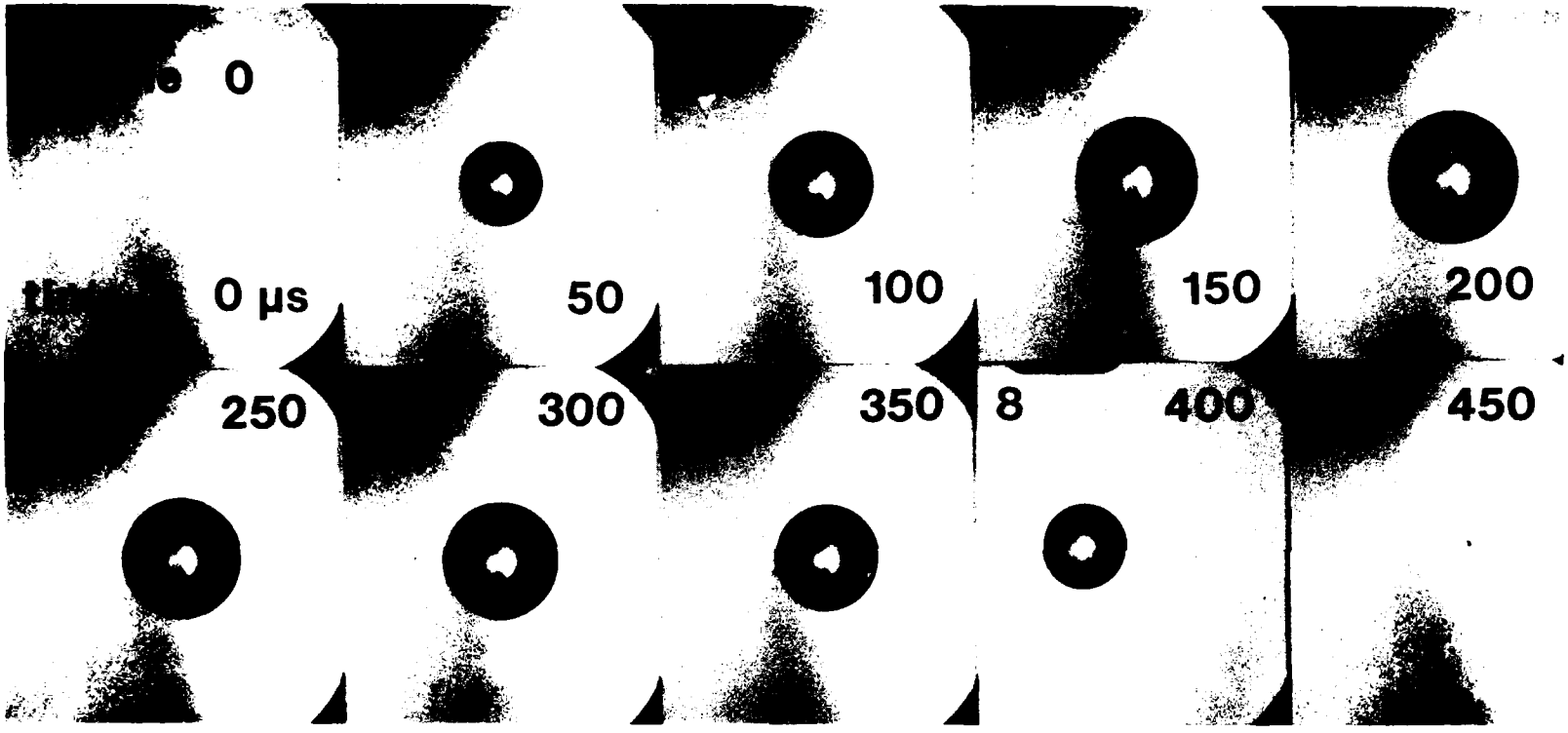

FIGURE 4-2A. Single-exposure photographic sequence of a laser-induced model cavitation bubble in quiescent distilled water ($R_0 \approx 0.23$ cm).

frame	α (mm)	β (mm)	r (mm)
1 *	50 ± ½	14 ± ½	21.4 ± 0.5
2	62½	32	40.0
3 *	65	40	47.0
4	69½	48	54.3
5 *	66½	51	55.7
6	66½	56½	59.7
7 *	63	56	58.2
8	62	59	60.0
9 *	57½	56½	56.8
10	53½	57	55.8
11 *	43	50½	47.9
12	35	47	42.6
13 *	21	36	30.1

* - the data from these frames must be multiplied by a correction factor of 1.03 due to a camera magnification inconsistency which resulted in an alternating frame size difference

TABLE 4-3A. Raw data from enlargements (see Figure 4-5).

bubble shape : ellipsoid of revolution

V - bubble volume

r, R - equivalent spherical radii

prolate spheroid :

α, a - major semiaxes

β, b - minor semiaxes

oblate spheroid :

α, a - minor semiaxes

β, b - major semiaxes

relationships :

$$V = (4/3)\pi R^3 = (4/3)\pi ab^2$$

therefore, $R^3 = ab^2$

similarly, $r^3 = \alpha\beta^3$

deformation amplitude :

$$a_2 \equiv A = a - R = 2(R - b)$$

TABLE 4-2. Deformation analysis relationships.

(α, β and r are measurements from photos
a, b and R are actual values for bubbles)

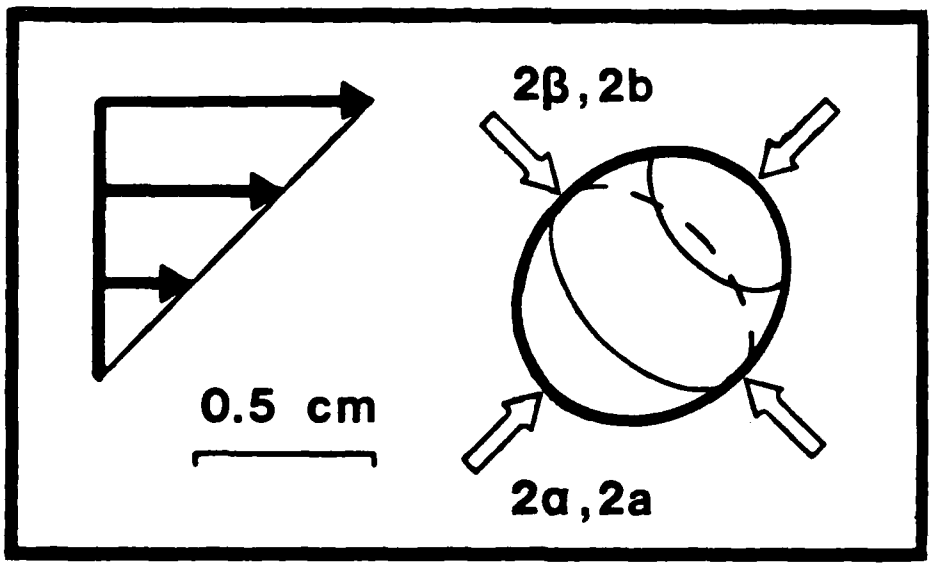

FIGURE 4-8B. Flow-induced nonspherical bubble shape from the experimental shear field.

for small amplitude deformations ($A \equiv a_2$), bubble shape has been approximated by an ellipsoid of revolution with orientation described above (Figure 4-8B). The equations describing the deformation amplitude (A) are presented in Table 4-2, as are the geometric relationships for the two cases of prolate and oblate spheroids. These data analyses have been used to quantify the photographic results displayed in Figure 4-5. Raw data from the enlargements are presented in Table 4-3A and reduced data describing the actual cavity are presented in Table 4-3B.

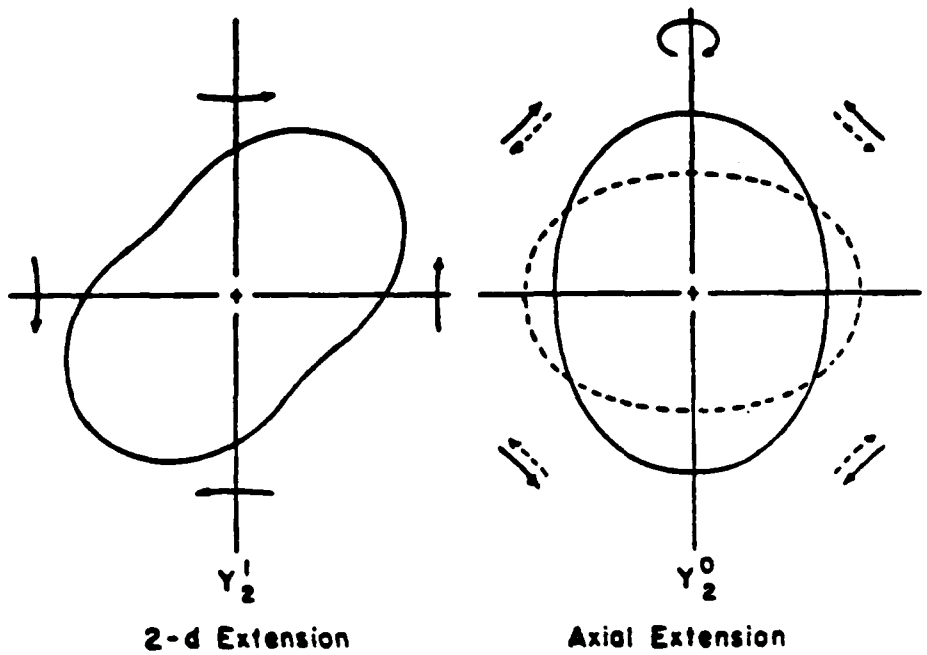

FIGURE 4-8A. Bubble shapes created by two and three-dimensional flow fields (Hara, 1983).

by one-half the original shear rate ($\frac{1}{2}\dot{\gamma}$). Since bubble growth and collapse are extremely rapid, very little bubble rotation is expected to occur over the short time scale of experimental interest. Thus, bubble deformation is expected to follow that which would be induced by the extensional flow field alone. In addition, Hara has demonstrated that the bubble shapes created by two- and three-dimensional extensional flows are indeed similar (Figure 4-8A), and for small values of bubble nonsphericity (A/R), the shapes become nearly identical. Therefore,

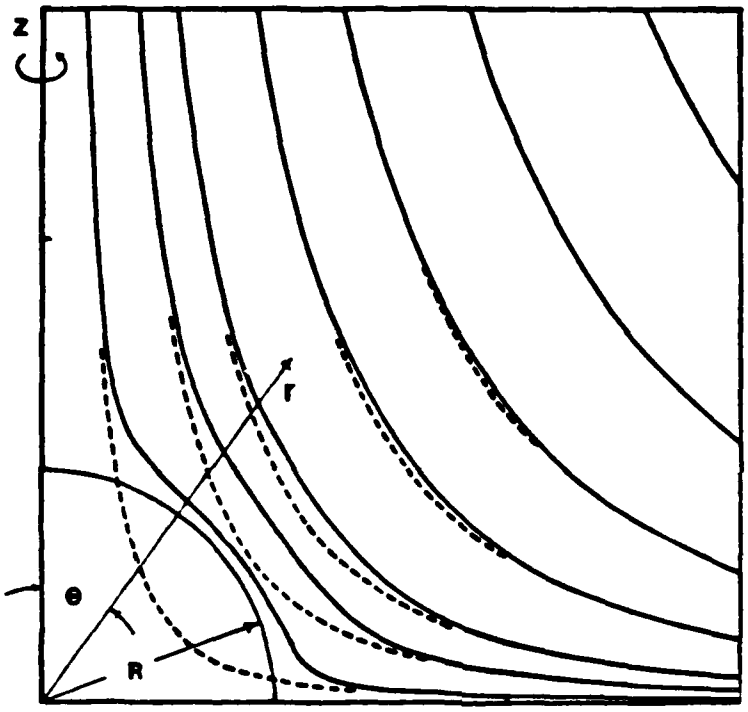

FIGURE 4-7. Uniaxial extensional flow field streamlines with and without model bubble presence (Hara, 1983).

Rotational symmetry of the bubble shape, about its axis of initiation for tests in quiescent liquids or about the axis of shear (extension) for experiments (theory) involving flowing fluids has been assumed. For the experimental situation of a two-dimensional imposed flow field, this assumption was not strictly correct. However, the experimental shear field can be represented by the linear addition of a purely extensional field and a purely rotational field (all two-dimensional). For these component flow fields the strain rate and rotation rate are both given

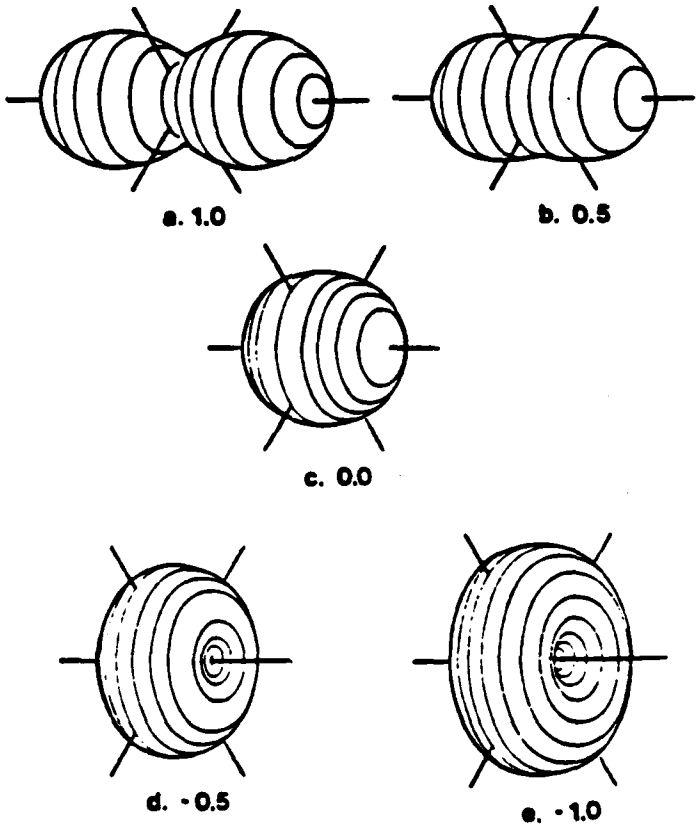

FIGURE 4-6. Nonspherical bubble shapes for several values of (a_2/R) (Hara, 1983).

and minor bubble axes (the largest horizontal and vertical dimensions). Neither the measurements of bubble axes at additional angles nor the inclusion of additional spherical harmonic terms, $a_3(t)Y_3^0(\theta,\phi)$ and/or $a_4(t)Y_4^0(\theta,\phi)$, in the theoretical description were found to improve the self-consistency of experimental data or the applicability of the theoretical model (Hara, 1983).

In the present research a similar approach has been adopted.

2. Data Analysis Techniques

Quantitative analysis of the raw data was accomplished through a straightforward extension of the method used by Hara (1983). In both the interpretation of model predictions and the fitting of experimental data, Hara adopted a slight variation of the standard expansion in terms of spherical harmonics (equation 2-10) to describe nonspherical bubble shapes. Hara assumed an axisymmetric shape given by,

$$r(\theta,\phi,t) = R(t) + a_2(t)\, Y_2^0(\theta,\phi) \tag{4-1}$$

where $r(\theta,\phi,t)$ describes the shape of the bubble surface for the specified spherical coordinates (θ,ϕ) and time (t), R(t) is the time-dependent *equivalent spherical radius* (that of a spherical bubble of equivalent volume) and $a_2(t)$ is the time-dependent amplitude of the spherical harmonic, $Y_2^0(\theta,\phi)$. Computed bubble shapes for a wide range of the ratio (a_2/R) were presented by Hara (Figure 4-6).

This technique was particularly applicable to the analyses of uniaxially imposed bubble deformations resulting from either nonspherical bubble initiation or from an external flow field. Hara's imposed model flow was a uniaxial extensional field (Figure 4-7) which resulted in small amplitude (a_2) deviations from sphericity (relative to R). Bubbles which were initiated nonspherically exhibited somewhat greater deformation amplitudes (though still less than R).

Hara also concluded that the bubble shape could be acceptably analyzed from experimental photographs simply by measuring the major

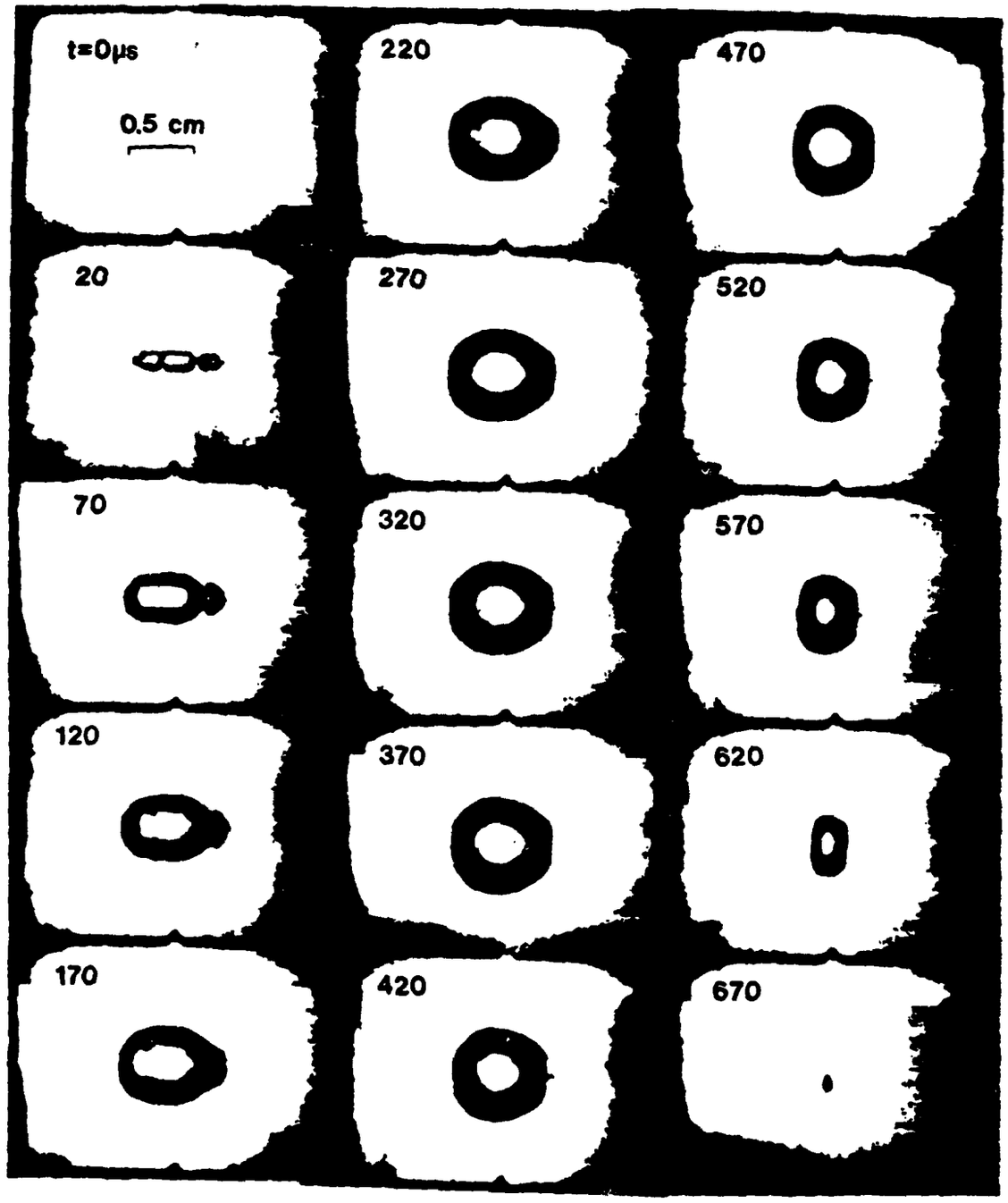

FIGURE 4-5. High-speed sequence of nonspherical bubble dynamics in a quiescent glycerol/water solution.

framing rate :	20,000 fps
recording time :	11.2 msec
exposure time :	2.7 μsec
frame separation :	50 μsec
F/stop :	2.5
shutter speed :	B
flash duration :	8.6 msec
flash intensity :	10^6 pbcp

TABLE 4-1. Typical high-speed photographic parameters.

were enlarged roughly 18.5 times and automatically photocopied. The quality of these *prints* was adequate for quantitative analysis and the effort and cost involved were small in comparison to those for *frame-by-frame* photographic enlarging.

A small number of trials involving nonspherically initiated cavities in quiescent Newtonian liquids were carried out. These experiments revealed surface tension driven oscillations imposed on spherical bubble growth and collapse, as previously predicted theoretically (Hara & Schowalter, 1984) and demonstrated experimentally (Hara, 1983). A typical sequence of nonspherical bubble dynamics in a quiescent glycerin solution (85 weight-percent glycerol in water) is shown in Figure 4-5. This bubble history was produced by making microfilm enlargements of each frame, then collating and reducing the prints.

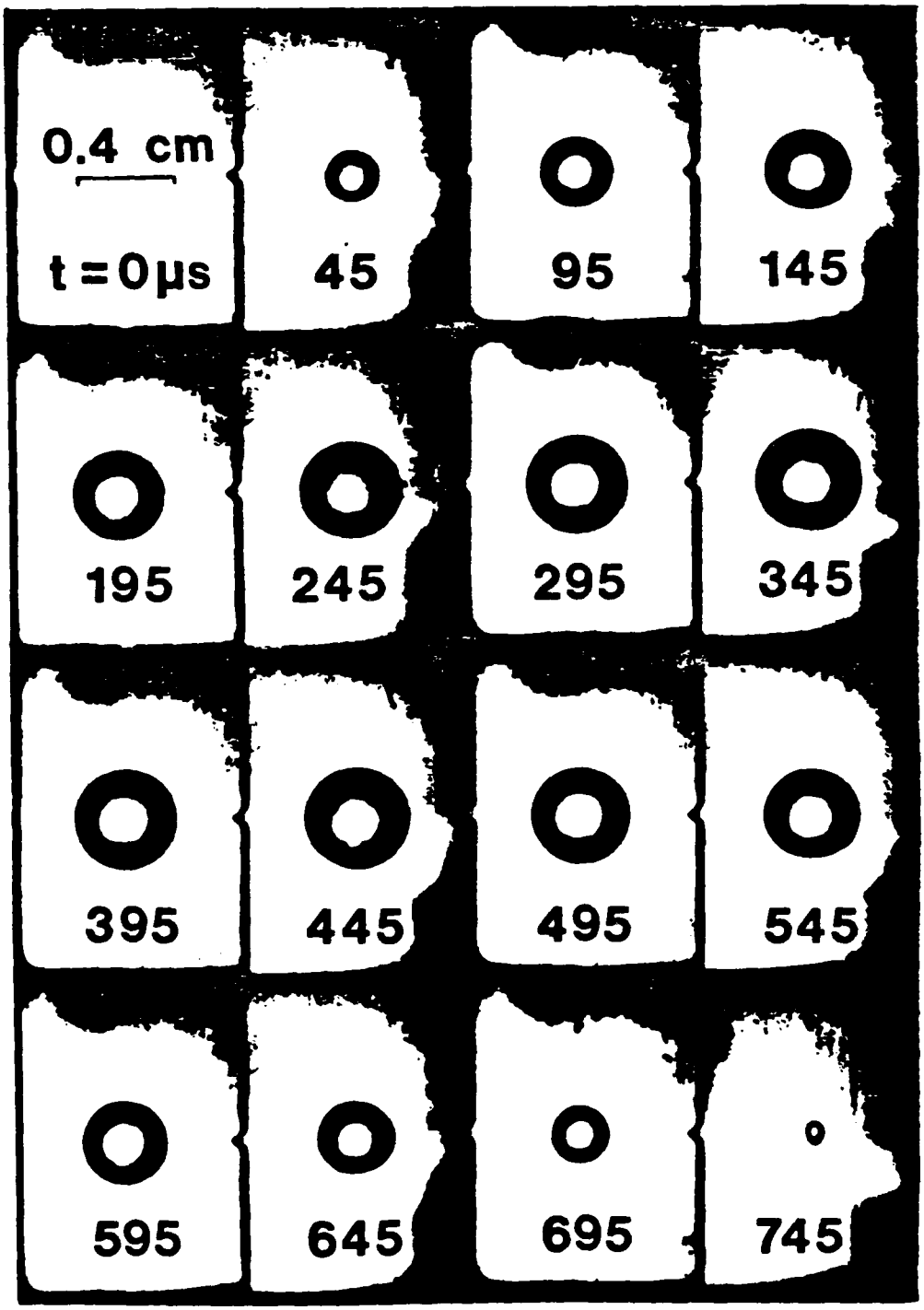

FIGURE 4-4. Typical high-speed photographic sequence of a nearly spherical cavity in quiescent distilled water.

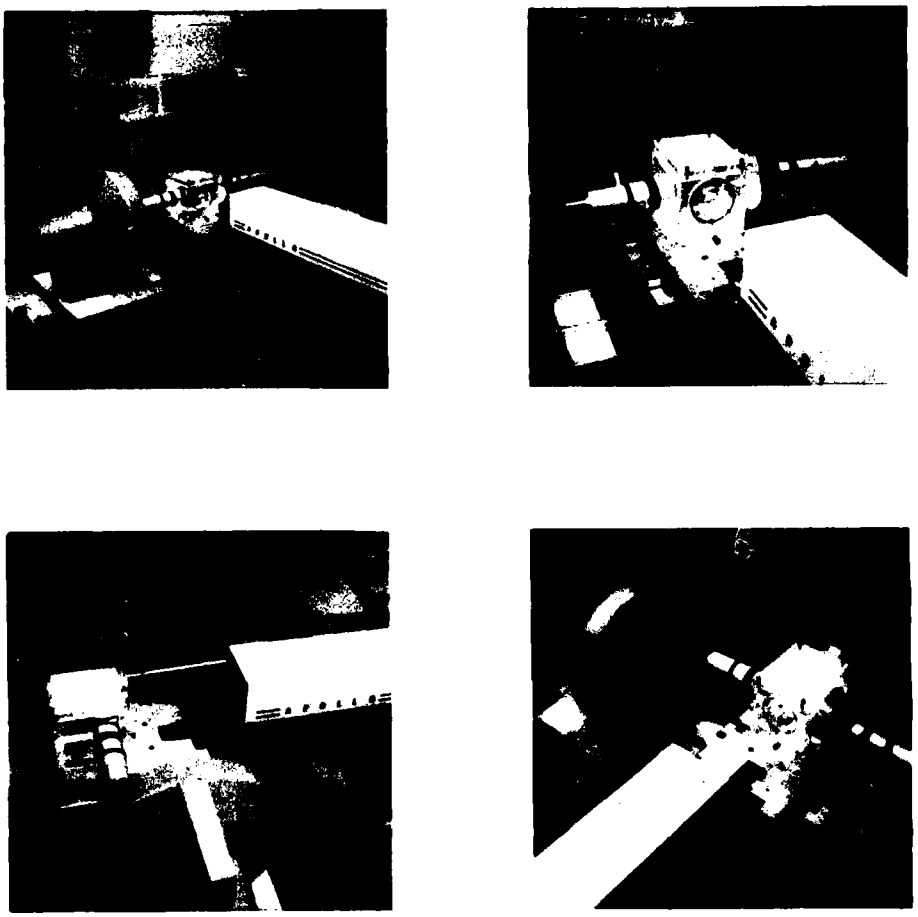

FIGURE 4-3. Experimental configuration with the high-speed photographic system for quiescent fluid tests.

confirmed (Chahine & Fruman, 1979; Hara, 1983).

The next steps involved the adaptation of the high-speed framing camera and electronic flash unit to the bubble production system. A somewhat new experimental configuration was required for the high-speed photographic system (Figure 4-3). For pilot experiments in quiescent fluids, the sequence of events was similar to that for the single-exposure system with one exception. Prior to starting the firing sequence, the high-speed framing camera had to be gradually brought up to the proper framing (rotation) rate. Parametric runs were then carried out to test the effects of various lighting, exposure, developing and printing techniques on the quality of the raw photographic data.

It was determined that the single most important quality of the photographic images was high contrast between bubble and background. The best results were achieved by using Kodak Technical Pan Film 2415 with a wide open camera aperture (f/2.5) and the maximum intensity flash setting available (8.6 msec duration at 1,000,000 peak beam candlepower). Although this film was slower than those used in other trials (Kodak TRI-X and 2475), its extremely fine grain and high contrast index (2.6 when processed with Kodak D-19 developer) resulted in high-resolution negative images. A sample high-speed sequence of a slighty nonspherical bubble in distilled water is shown in Figure 4-4. In addition, typical values for several high-speed photographic parameters are presented in Table 4-1.

It was further discovered that the analysis of the high-speed sequences (10 to 25 frames of interest) could be facilitated by the use of a microfilm reader/printer (3M Model 500). The 7.5 by 10 mm frames

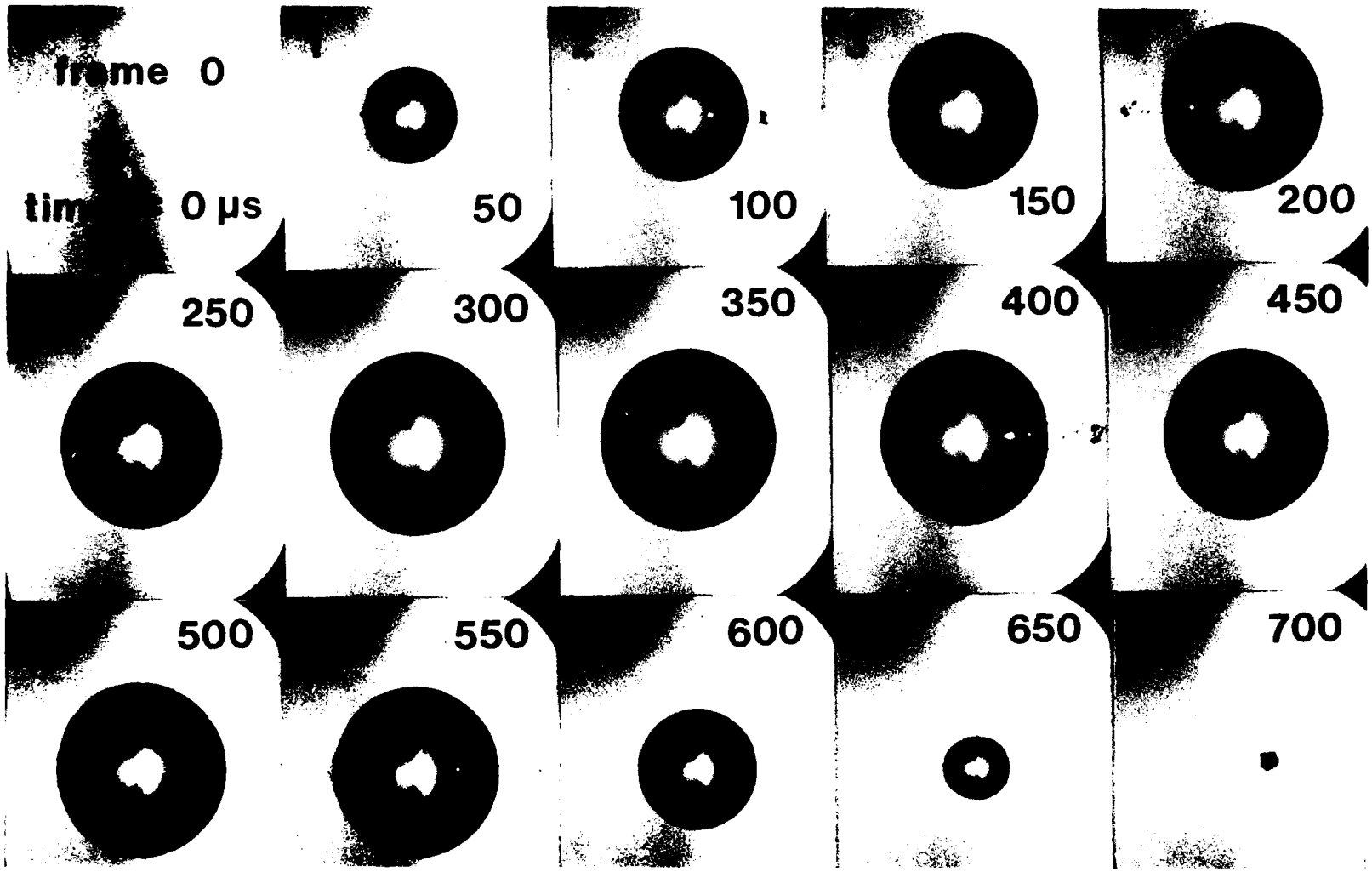

FIGURE 4-2B. Typical sequence of a spherical bubble in DH2O ($R_0 \approx 0.36$ cm).

frame	t (μsec)	R (cm)	A (cm)
	0	0.00	
1	30	0.114 ± 0.004	+.153 ± 0.002
2	80	0.207	+.117
3	130	0.251	+.096
4	180	0.281	+.079
5	230	0.297	+.058
6	280	0.309	+.035
7	330	0.311	+.025
8	380	0.311	+.010
9	430	0.303	+.004
10	480	0.289	-.012
11	530	0.255	-.026
12	580	0.221	-.039
13	630	0.160	-.048
	680	0.00	

TABLE 4-3B. Reduced data from analysis (see Figure 4-5).

3. Flow System Experiments

The experimental investigation of shear flow induced bubble deformation has constituted the major fraction of this research effort. To this extent the high-speed framing camera and electronic flash unit were adapted for use with the cylindrical Couette flow system (Figures 4-9A and 4-9B). To properly enter the flow system test region from below, the laser output pulse was modified from horizontal to vertical by reflection from a high-energy laser mirror. A coaxial configuration of several components was required to insure undistorted, backlit imaging of the cavities in the test region (Figure 4-10).

Preliminary experimentation using the flow system was undertaken with a highly viscous ($\eta \approx 1.05$ poise) glycerol/water solution. Bubbles which were produced and photographed in a quiescent test region ($\omega = 0$ rpm) grew and collapsed spherically (within the limits of measurement error). In addition, these model cavitation bubbles closely followed the aforementioned dynamic Rayleigh behavior. These observations confirmed that no serious asymmetric effects had been introduced by the flow system design.

Next, experiments were carried out with an outer-cylinder rotation rate (ω) of 360 rpm (shear rate : $\dot{\gamma} \approx 100$ sec^{-1}). As expected, bubble deformation (elongation along the axis of shear) was observed and measured. The deformation amplitudes (A) were found to be small relative to the steady-state deformation (equation 3-3) predicted by the constant volume bubble modelling (0.01 cm versus 0.20 cm). As a result, the uncertainty in the deformation amplitude measurements was large, up to ± 20% (± 0.002 cm).

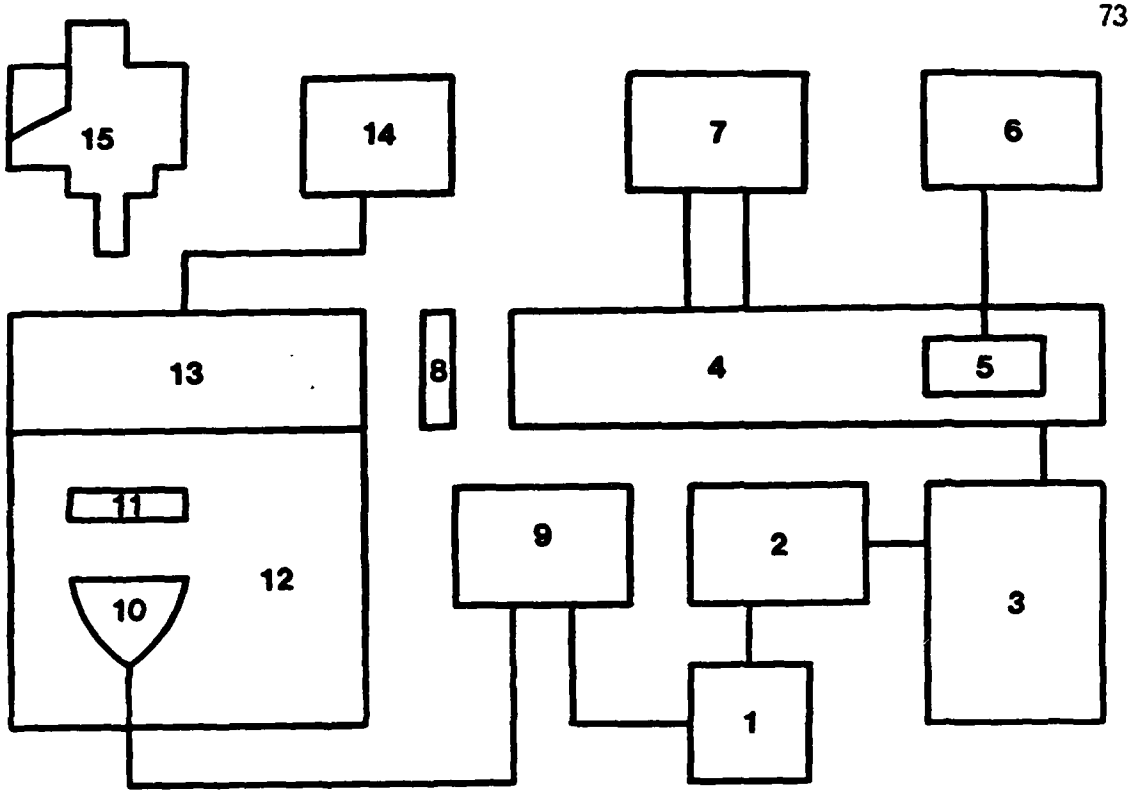

1 SYSTEM TRIGGER
2 DELAY GENERATOR
3 LASER POWER SUPPLY
4 RUBY LASER
5 HeNe LASER
6 HeNe POWER SUPPLY
7 COOLING SYSTEM
8 LASER FILTER
9 FLASH POWER SUPPLY
10 FLASHLAMP HEAD
11 FRESNEL LENS AND/OR FLASH DIFFUSER
12 FLOW SYSTEM SUPPORT
13 COUETTE FLOW SYSTEM
14 FLOW SYSTEM MOTOR
15 HIGH-SPEED CAMERA

FIGURE 4-9A. Schematic diagram of the equipment configuration for flow experiments.

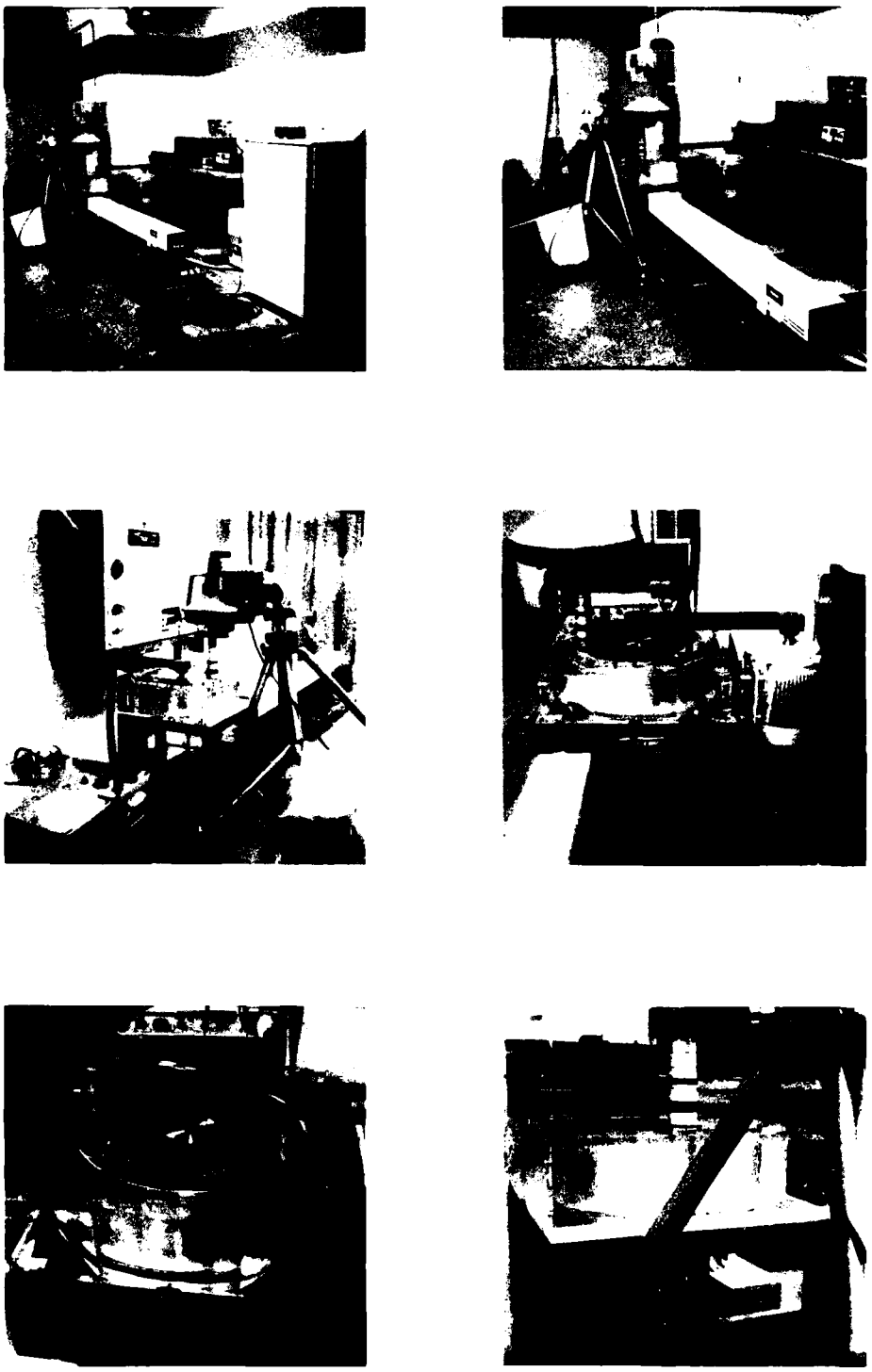

FIGURE 4-9B. Photographs of the experimental system in shear flow test configuration.

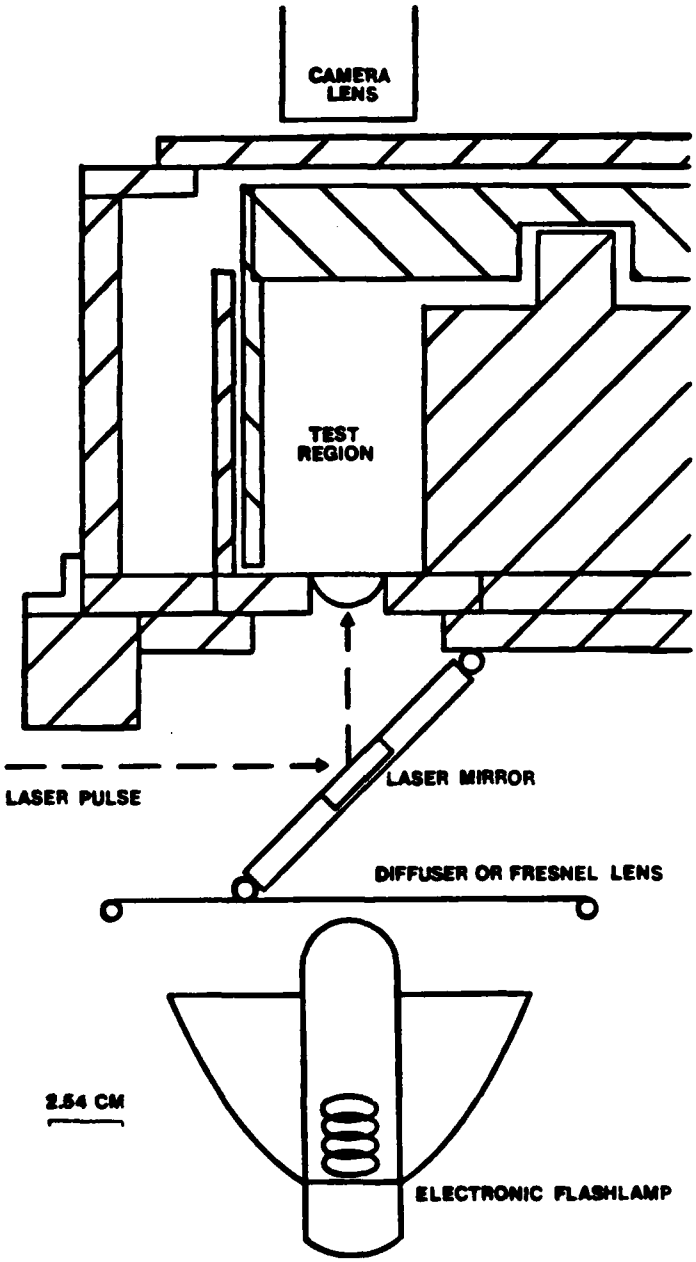

FIGURE 4-10. Coaxial configuration of the experimental components near the flow system test region.

To minimize this uncertainty, an averaging scheme was introduced under which several (usually five) bubble sequences were photographed under identical experimental conditions. These were then nondimensionalized with respect to maximum bubble radius [R/R_0] and a pseudo-Rayleigh collapse time [t/τ]. The collapse time (τ), used to determine this dimensionless time, is defined as the *experimental collapse period*. The details of its determination and use are described below. The reduced data were then averaged to produce composite sequences of (a) dimensionless radius versus dimensionless time and (b) deformation amplitude (dimensional) versus dimensionless time. The resulting composites were much smoother than the individual sequences of reduced data. As a result, they were more easily compared to one another and to theoretical predictions. In addition, the amplitude measurement scatter for the composites was reduced to approximately ± 10% (± 0.001 cm). For both the reduced data and the composite sequences, the bubble radius measurement uncertainty was minimal (less than ± 2%).

Rayleigh's *empty bubble* analysis has shown the collapse time, t_c to be a linear function of maximum bubble radius (equation 2-2). Since these laser induced cavities closely followed this symmetric behavior, the total bubble lifetime, Δt, was very nearly equal to twice the Rayleigh collapse time. Thus, an experimental collapse period, τ, normalized by the maximum bubble radius, was determined from the average ratio of total lifetime to maximum radius for several bubbles

under identical experimental conditions,

$$(\tau/R_0) = (1/n) \sum_{i=1}^{n} [\Delta t/2R_0]_i \qquad (n \approx 5) \qquad (4\text{-}2)$$

The uncertainty in the maximum bubble radius (±1%) was found to be significantly less than the uncertainty in the total bubble lifetime (see Table 4-4). Therefore, the maximum bubble radius values $[R_0]_j$ were used to determine the experimental collapse period values (τ_j) from the normalized collapse period (τ/R_0). By using the appropriate value of τ_j for each bubble sequence,

$$\tau_j \equiv (\tau/R_0)\ [R_0]_j \qquad (4\text{-}3A)$$

$$= ([R_0]_j/2n) \sum_{i=1}^{n} [\Delta t/R_0]_i \qquad (n \approx 5) \qquad (4\text{-}3B)$$

the results for several bubbles of different (but similar) sizes were temporally normalized and averaged to produce a composite sequence (equation 4-4).

In addition, the ranges of the dimensionless parameters were seen to be,

$$0 \le (R/R_0) \le 1$$

$$0 \le (t/\tau) \le 2$$

with,

$$(R/R_0) \equiv 0 \quad \text{at} \quad (t/\tau) = 0$$
$$(R/R_0) \approx 1 \quad \text{at} \quad (t/\tau) = 1$$
$$(R/R_0) \approx 0 \quad \text{at} \quad (t/\tau) = 2 \ .$$

Relative to the experimental uncertainty, the effect of maximum bubble size on the deformation amplitudes of these model bubbles was practically insignificant. The measurements of maximum bubble radius and maximum deformation amplitude were found to be completely uncorrelated for otherwise identical experiments. The range of maximum bubble sizes was fixed for all flow experiments,

$$0.4 \leq R_0 \text{ (cm)} \leq 0.5$$

The composite maximum bubble radius ($\overline{R}_0$) for a set of (i) identical experiments was defined as the arithmetic mean of the (i) individual maximum bubble radii.

Significant quantitative results were first obtained for flow experiments using distilled water (DH2O). Composites of bubble sequences (five) were made for several rotation speeds between 0 and 1000 rpm. The spherical dynamics of all these bubbles were essentially identical. A profile of average dimensionless radius (equivalent spherical radius) versus dimensionless time is presented in Figure 4-11. Dimensional spherical parameters for these experiments

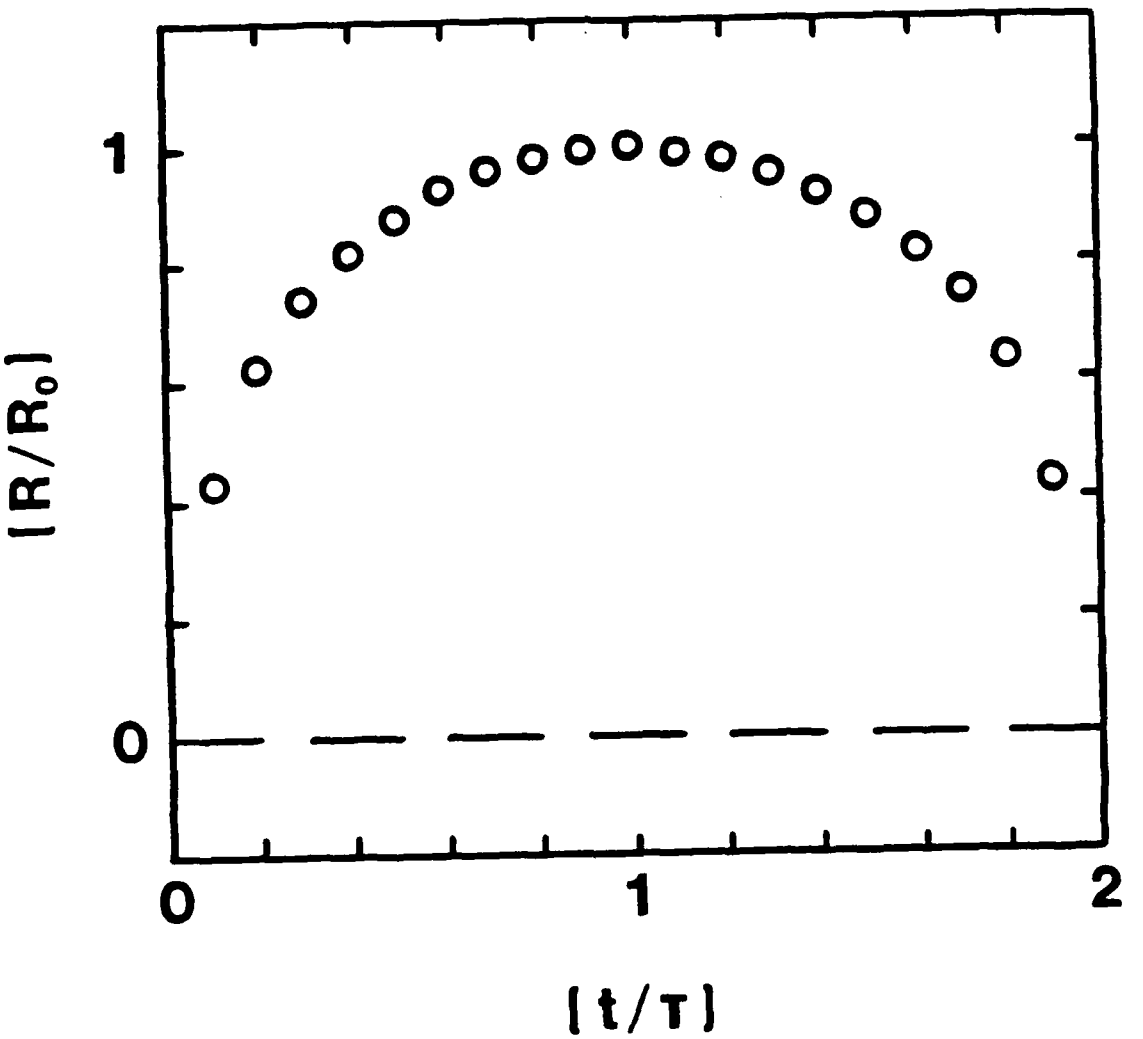

FIGURE 4-11. Dimensionless radial profile composite for bubbles in distilled water. (all rotation/shear rates - see Table 4-4)

ω(rpm)	$\overline{R}_0$(cm)	$2\tau/\overline{R}_0$(μsec/cm)
0	0.448 ± .004	1965 ± 60
360	0.463 ± .004	1949 ± 53
480	0.458 ± .004	1944 ± 30
575	0.474 ± .004	1921 ± 34
720	0.446 ± .004	1955 ± 28
865	0.427 ± .004	1902 ± 30

TABLE 4-4. Dimensional spherical parameters for DH2O experiments.

are presented in Table 4-4. Average deformation amplitude $[\overline{A}]$ versus dimensionless time for four composite cases is presented in Figure 4-12 (the results for 480 and 720 rpm were omitted simply for graphic clarity).

This average amplitude was arrived at by interpolating and averaging the individual values over the range of dimensionless time as follows,

$$\overline{A}(t/\tau) = (1/n) \sum_{i=1}^{n} A_i(t_j) \qquad (4\text{-}4)$$

with $t_j \equiv [t/\tau]\ \tau_j$

for $0 \le [t/\tau] \le 2$.

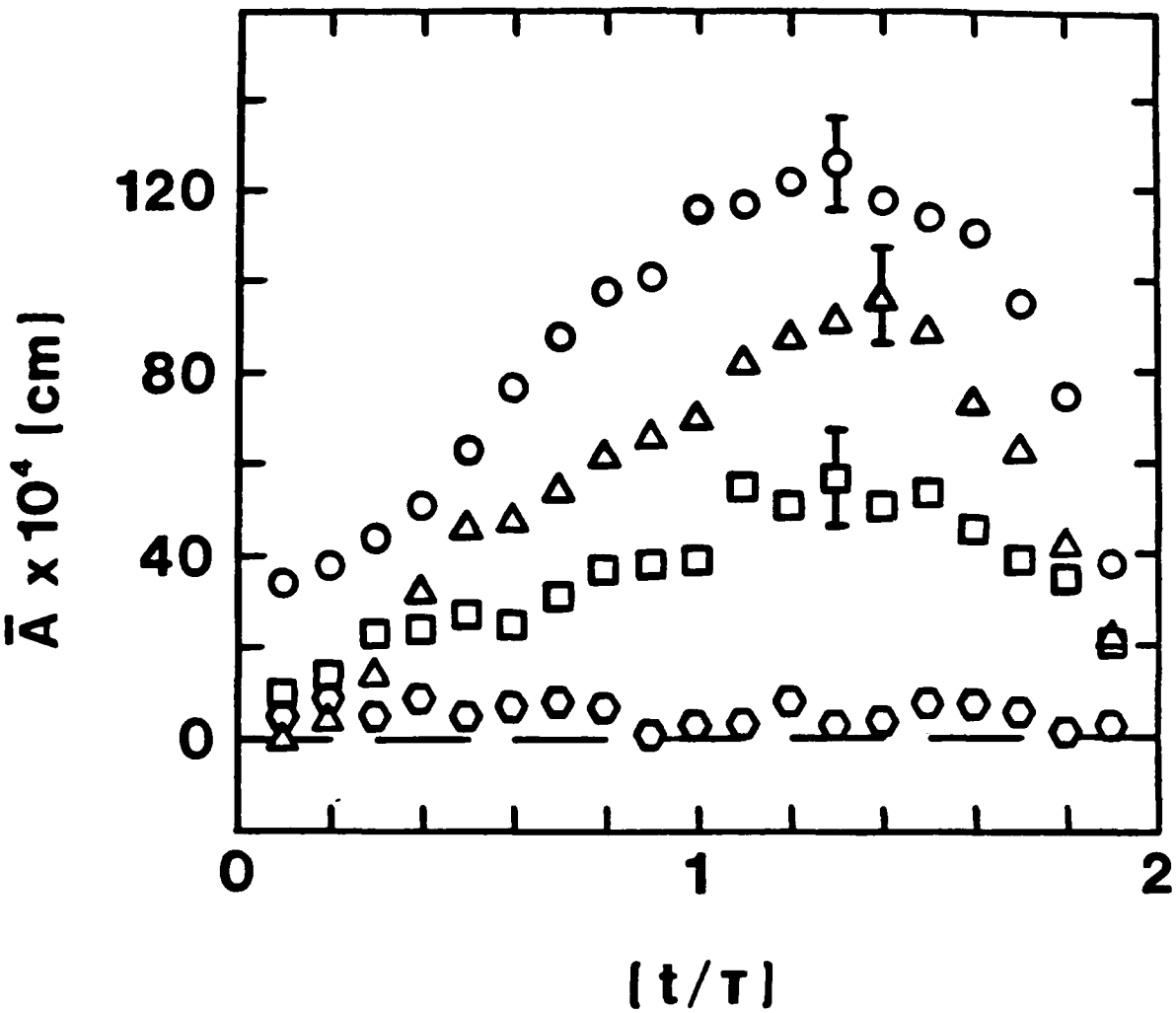

FIGURE 4-12. Composite deformation amplitudes versus dimensionless time for bubbles in DH2O.

symbol	ω(rpm)	$\dot{\gamma}$(sec^{-1})
⬡	0	0
□	360	105
△	575	170
○	865	255

where A_i is the deformation amplitude of each sequence at the particular dimensional time, t_j, corresponding to the appropriate dimensionless time $[t/\tau]$. The average dimensionless bubble radius $\overline{(R/R_0)}$ is determined similary from the dimensionless radial profiles (R/R_0) of each particular bubble sequence.

As seen in Figure 4-12, the flow induced deformation amplitude grew fairly smoothly from inception until maximum deformation was reached near a time $[t/\tau]$ of about 1.4. Interestingly, this point occured well after maximum bubble size was reached, near a time of about 1.0. As bubble collapse continued, the deformation amplitude quickly decayed to nearly zero at complete collapse ($[t/\tau] \approx 2.0$). As expected, the deformation amplitude grew more rapidly and to a larger maximum value as the flow strength was increased. Figures 4-13A and 4-13B show the effect of flow strength on maximum deformation [max $\bar{A}$] and deformation growth rate $[d\bar{A}/d\tau]$ respectively. Deformation growth rate was defined as the linear least squares slope from the origin through the data during bubble growth. It is given by,

$$[d\bar{A}/d\tau] \equiv \frac{\sum_{i=1}^{10} (t/\tau)\, \bar{A}(t/\tau)}{\sum_{i=1}^{10} (t/\tau)^2} \qquad (4\text{-}5)$$

for $\quad 0 \le [t/\tau] \le 1$

where $\quad [t/\tau] = (i/10)$.

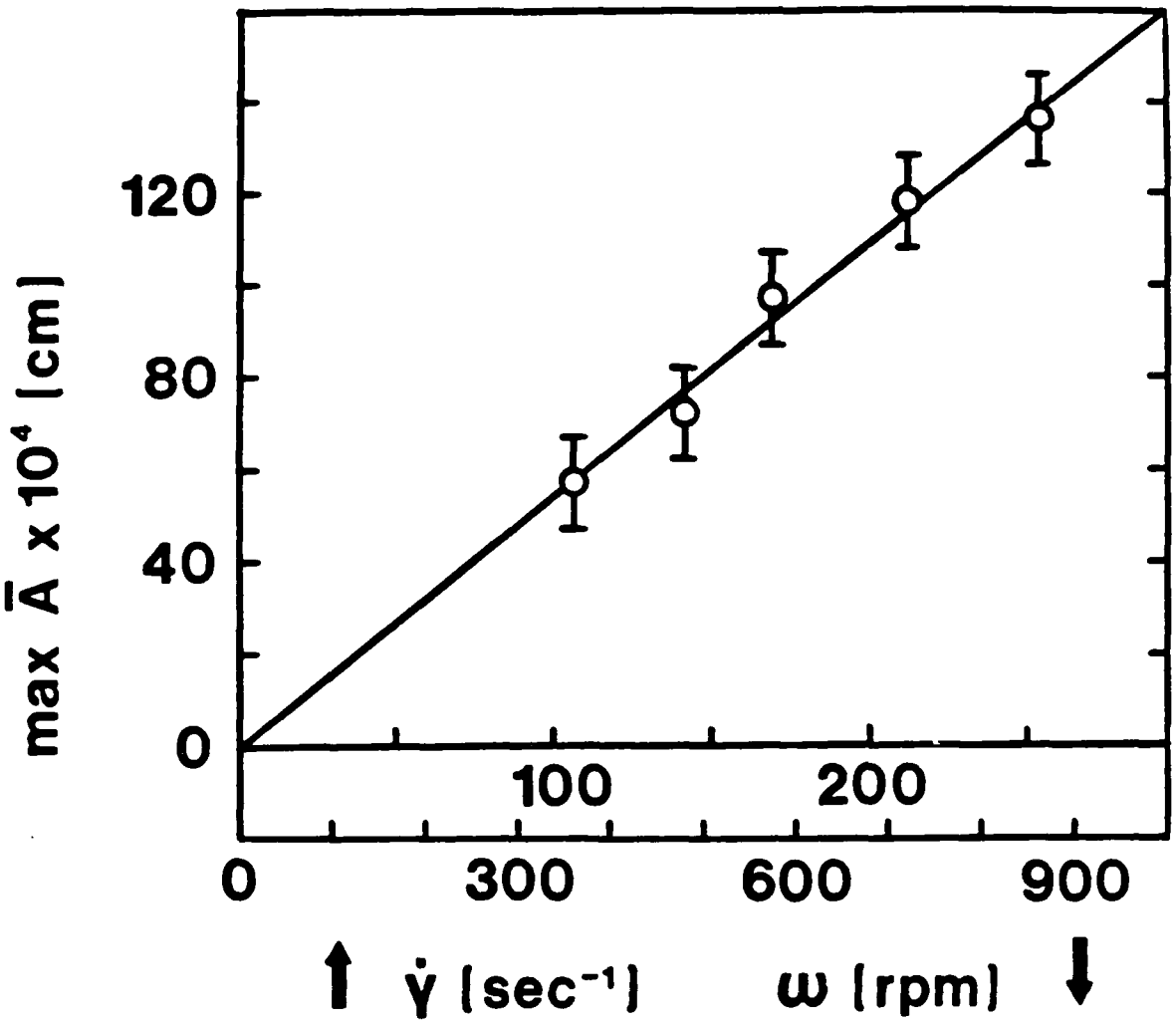

FIGURE 4-13A. Maximum deformation amplitude versus flow strength for bubbles in DH2O.

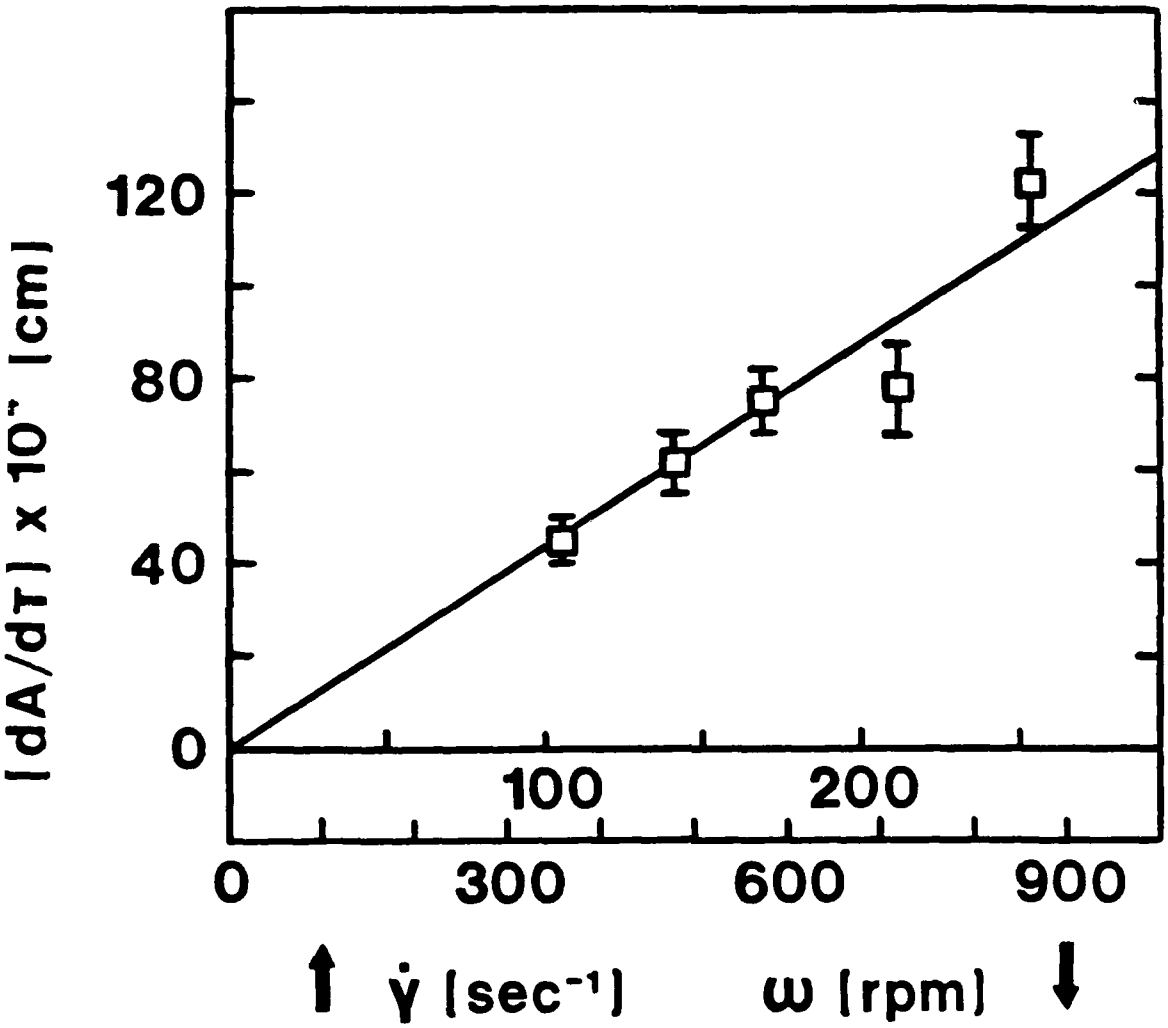

FIGURE 4-13B. Deformation amplitude growth rate versus flow strength for bubbles in DH2O.

AD-A154 575 BUBBLE DYNAMICS IN POLYMER SOLUTIONS UNDERGOING SHEAR 2/2
(U) PRINCETON UNIV NJ DEPT OF CHEMICAL ENGINEERING
P S KEZIOS 01 APR 85 160-6076-4 N00014-79-C-0385

UNCLASSIFIED F/G 20/4 NL

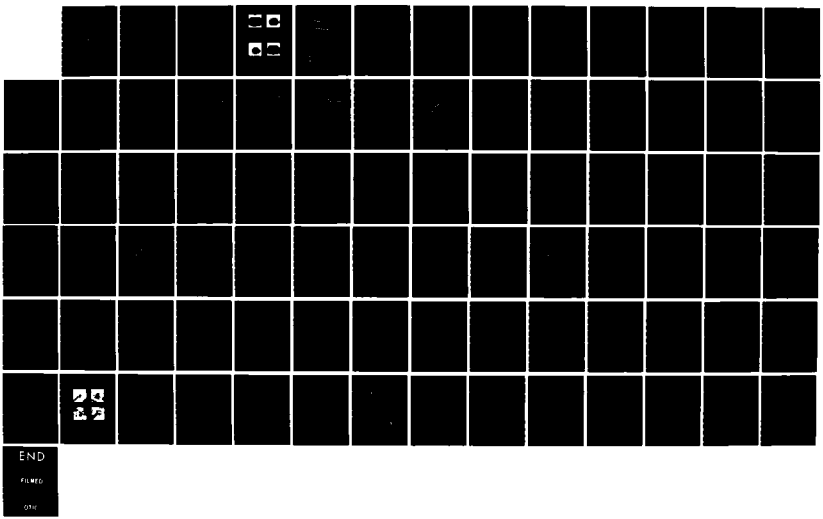

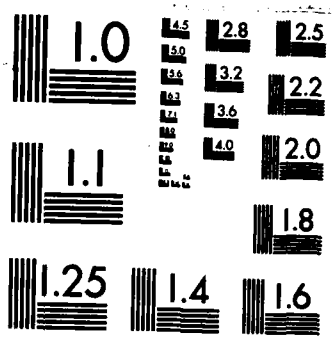

MICROCOPY RESOLUTION TEST CHART
NATIONAL BUREAU OF STANDARDS-1963-A

In both cases the data displayed linear relationships. These are,

$$[\max \bar{A}](10^4) = 0.160(\omega)$$
$$= 0.547(\dot{\bar{\gamma}}) \qquad (4\text{-}6)$$

$$[d\bar{A}/d\tau](10^4) = 0.128(\omega)$$
$$= 0.4365(\dot{\bar{\gamma}}). \qquad (4\text{-}7)$$

For an impulsive rotation under these experimental conditions of concentric cylindrical geometry and Newtonian rheology, the flow field dynamics, except for the quiescent case, were predicted (Bird, Stewart & Lightfoot, 1960; Schlichting, 1968) to lie in the turbulent regime, at least until a steady-state flow was achieved (see Chapter 3). The transition speed for cylinder rotation was defined as the constant angular velocity for which an impulsive flow start-up would (temporarily) result in turbulent flow conditions. For this experimental geometry it is given by,

$$\omega_t = 3400(\nu)$$
$$= 34 \text{ rpm} \qquad (DH2O) \qquad (4\text{-}8)$$

for this situation where ν is the fluid kinematic viscosity (η/ρ) in (cm^2/sec). Despite the possible persistence of turbulent flow conditions within the test region, the radial shear rate profile was assumed to

approximate that for the laminar situation (equations 3-6). It was anticipated that any turbulent velocity component(s) in the r- and/or z-direction(s) would be insignificant relative to the dominant θ-component and that the streamlines would remain essentially unidirectional, as in laminar flow. Flow visualization experiments of entrained air bubbles gave qualitative support to these assumptions (Figure 4-14). Quantitatively, the experimental results (turbulent flow field velocity measurements) of Wendt (1933) (see Chapter 3) were interpolated for the present experimental geometry ($\kappa \approx 0.72$). Close to the center of the annular gap, laminar and turbulent shear rate values were the same (to within ± 5%).

To further investigate the dynamic flow-induced bubble deformations, particularly the effects of additives, an experimental scheme involving several solvents and polymer solutions was conceived. The essence of this program is presented in Figure 4-15 and a summary of the experiments is given in Table 4-5. Figure 4-15 represents the possible space of simplified fluid rheology (described by ν) as a function of flow strength (given by ω and $\dot{\gamma}$). The vertical dashed lines indicate the experimental rotation speeds (shear rates). The horizontal dashed lines describe the Newtonian rheology of the constant viscosity solvents. Shear-thinning polymer solution behavior is displayed by the sloping sets of points representing actual rheological measurements. These measurements were performed using a Rheometrics System IV Mechanical Spectrometer in a *cone-and-plate* geometry. The criterion for the laminar/turbulent flow transition (equation 4-8) is also superimposed as a solid, straight line in Figure 4-15. In addition, the flow field for these dilute polymer solutions was assumed to approximate that for the

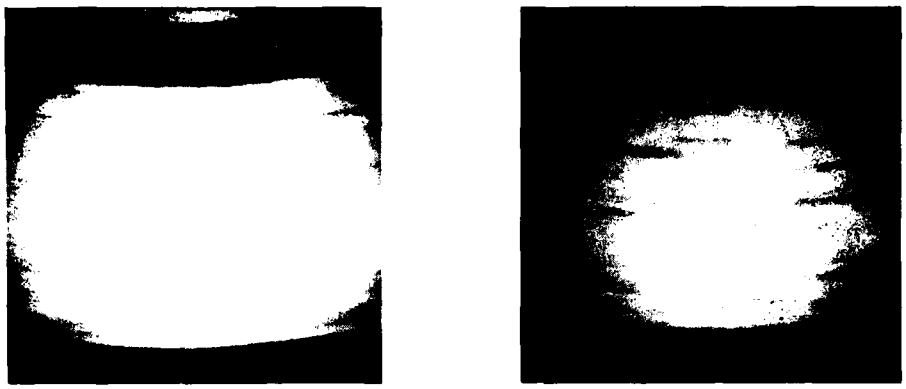

ω = 360 rpm

ω = 575 rpm

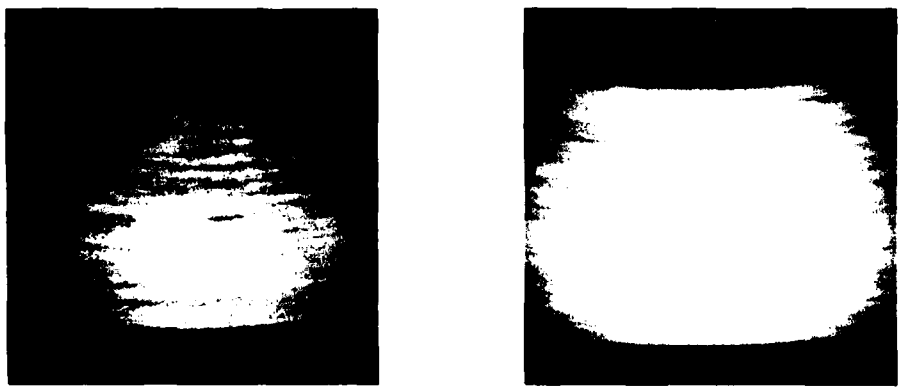

FIGURE 4-14. Flow visualization streaks of entrained air bubbles in the annular region of the cylindrical Couette flow system.
(test fluid : distilled water)

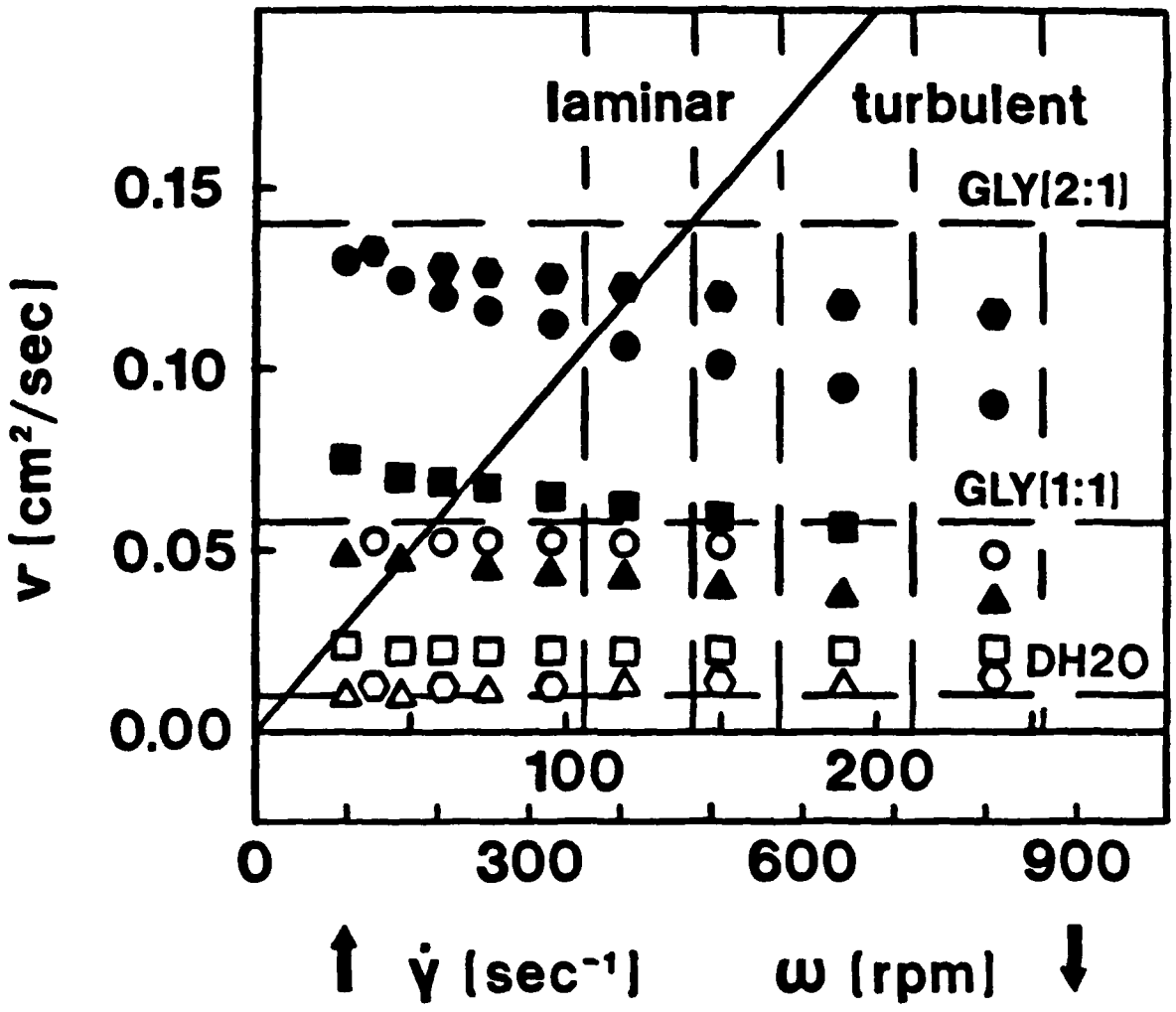

FIGURE 4-15. Experimental flow space diagram (simplified fluid rheology as a function of experimental flow strength).

symbol	fluid	symbol	fluid
⬢	GLY(1:1)+500PAM	○	DH2O+2000PEO
●	DH2O+2000PAM	□	DH2O+1000PEO
■	DH2O+1000PAM	⬡	DH2O+1000PEO*
▲	DH2O+500PAM	△	DH2O+500PEO

fluids	0	105	140	170	210	255
		(↑) $\dot{\gamma}$ (sec^{-1})				
				ω (rpm)	(↓)	
	0	360	480	575	720	865
DH2O	X	X	X	X	X	X
DH2O+500PAM	X	-	-	X	-	-
DH2O+1000PAM	X	-	-	X	-	-
DH2O+2000PAM	X	-	-	X	-	-
DH2O+500PEO	X	-	-	X	-	-
DH2O+1000PEO	X	-	-	X	-	-
DH2O+2000PEO	X	-	-	X	-	-
DH2O+1000PEO*	X	-	-	X	-	-
GLY(1:1)	X	X	X	X	-	-
GLY(1:1)+500PAM	X	X	X	X	-	-
GLY(2:1)	X	X	X	X	-	-

TABLE 4-5. Summary of experiments.

Newtonian solvents under identical experimental conditions.

From this graphic representation of the simplified experimental space it was seen that the effects of polymer solutes on flow experiment results could be examined by two related comparisons. First, the experimental data for a polymer solution could be compared directly to the data for its pure solvent under similar conditions. This comparison, especially for several polymer solutions of different concentrations, could demonstrate the competition between Newtonian (viscous) and non-Newtonian (elastic) effects. Alternatively, the polymer solution results could be compared to the appropriate results for a Newtonian solvent of similar kinematic viscosity. This second comparison would possibly better isolate and elucidate the effects of elasticity since any additional viscous effects of a polymer solution would be accounted for by an increased viscosity of the *reference* solvent. Also, the flow regimes for these comparisons would be more similar. However, the shear thinning behavior of most polymer solutions would necessitate the use of a different Newtonian solvent for each flow strength investigated. Additionally, this experimental *flow space* graph allowed fluids and flow strengths to be determined such that the effects of the laminar/turbulent flow transition could be investigated. This would be important for the solution/solvent comparisons since these fluids would almost never lie in identical regimes of the *flow space*.

The most important results involved the observations and measurements of the dramatic reduction in bubble deformation amplitudes caused by the addition of small amounts of water-soluble polymer to an

polyacrylamide :

$$[\ -CH_2\underset{CONH_2}{CH}-\ ]_n$$

Polysciences, Inc.

$M \approx 5\text{-}6 \times 10^6$
cat. no. 2806
lot no. 12762

polyethylene oxide :

$$[\ -CH_2CH_2O-\ ]_n$$

Aldrich Chemical Company

$M \approx 5 \times 10^6$
cat. no. 18,947-2
lot no. 1819KH

$M \approx 1 \times 10^5$
cat. no. 18,198-6
lot no. 0923HH

TABLE 4-6. Polymer product information.

aqueous system. Two high molecular weight linear polymers, polyacrylamide (PAM) and polyethylene oxide (PEO), were chosen for investigation. This choice was made because of the extensive use of these polymers in hydraulic cavitation inhibition/suppression research (see Chapters 1 & 2). Both samples were polydisperse and of similar molecular weight (see Table 4-6). In addition, a polyethylene oxide

sample of much lower molecular weight (PEO*) was studied for comparison.

Three dilute aqueous solutions of different concentrations (C = 500, 1000 and 2000 wppm) of both higher molecular weight samples were used in experiments. Only one solution (C = 1000 wppm) of the lower molecular weight sample was used. A single solution of polyacrylamide (C = 500 wppm) in a glycerol/water solvent (1:1 by weight) was also examined. All these solutions were prepared by the addition of the appropriate amount of dry polymer powder to 18 liters of solvent. The powder was dispersed by slow pouring into the vortex of the stirred fluid. This dispersion was then slowly *rolled* in a large carboy until the solute was completely dissolved (usually 24-72 hours). This low-shear preparation minimized the effects of mechanical polymer degradation.

Rheological measurements on the polymer solutions were made both before and after experimentation. Only a small reduction in solution viscosity was observed ($\Delta\eta \leq 10\%$). Therefore, solution rheology was characterized by average values of these measurements. The surface tensions (σ) of the solvents and solutions were obtained experimentally from measurements of the maximum equilibrium force on a vertical rod supporting a stable meniscus (Padday, Pitt & Pashley, 1975). Solvent densities (ρ) were obtained from the literature (Weast, 1974; Perry & Chilton, 1973). A summary of solvent and solution properties is presented in Table 4-7.

As expected, the dilute aqueous polymer solutions produced no significant changes in the equivalent spherical bubble dynamics

solvent	$\dot{\gamma}(sec^{-1})$	η_s(poise)	ρ(g/cc)	$\nu(cm^2/s)$	σ(dyne/cm)
DH2O	all	0.01	1.00	0.01	71.0
GLY(1:1)	all	0.064	1.125	0.057	67.7
GLY(2:1)	all	0.164	1.17	0.14	65.8

solution	$\dot{\gamma}(sec^{-1})$	η(poise)	ρ(g/cc)	$\nu(cm^2/s)$	σ(dyne/cm)
DH2O+500PAM	170	0.039	1.00	0.039	71.0
DH2O+1000PAM	"	0.058	"	0.058	"
DH2O+2000PAM	"	0.098	"	0.098	"
DH2O+500PEO	170	0.012	1.00	0.012	61.0
DH2O+1000PEO	"	0.022	"	0.022	"
DH2O+2000PEO	"	0.051	"	0.051	"
DH2O+1000PEO*	"	0.014	"	0.014	"
GLY(1:1)+500PAM	105	0.139	1.125	0.124	67.2
GLY(1:1)+500PAM	140	0.136	"	0.121	"
GLY(1:1)+500PAM	170	0.134	"	0.119	"

TABLE 4-7. Solvent and solution properties.

($[\overline{R/R_0}]$ versus $[t/\tau]$). A slight increase in the *normalized experimental collapse time* $[\tau/R_0]$ was observed, but it was less than the experimental standard deviation for that quantity.

The anticipated effects of the polymer solutes on bubble nonsphericity were threefold. First, the inherent increase in solution viscosity over solvent viscosity (Table 4-7) should promote flow-induced bubble deformation. Similarly, the decrease in solution surface tensions (Table 4-7) resulting from the macromolecular presence (only significant for PEO solutions) should increase deformation amplitudes. Opposing these effects was the solution elasticity which was a direct result of the polymer addition. As the experimental data clearly show (Figures 4-16A and 4-16B), this elastic effect was dominant and flow induced deformation was suppressed in the aqueous PAM and PEO solutions.

This suppression could be seen in both the maximum deformation amplitudes and the deformation growth rates of cavities in these solutions. For polyethylene oxide the reductions in these quantities were 0-15% for the 500 wppm solution and 30-35% for the 1000 wppm solution. The polyacrylamide solutions demonstrated even more pronounced effects with reductions for the 500 and 1000 wppm solutions of 30-50% and 45-55% respectively. Interestingly, this trend did not continue for either of the 2000 wppm solutions. At this concentration the deformation reductions were only 15-25% for the PAM solution and 25-30% for the PEO solution.

The competition between viscous and elastic effects was demonstrated by this upturn in maximum deformation amplitudes at the highest polymer concentration (Figure 4-17). With polyacrylamide the upturn

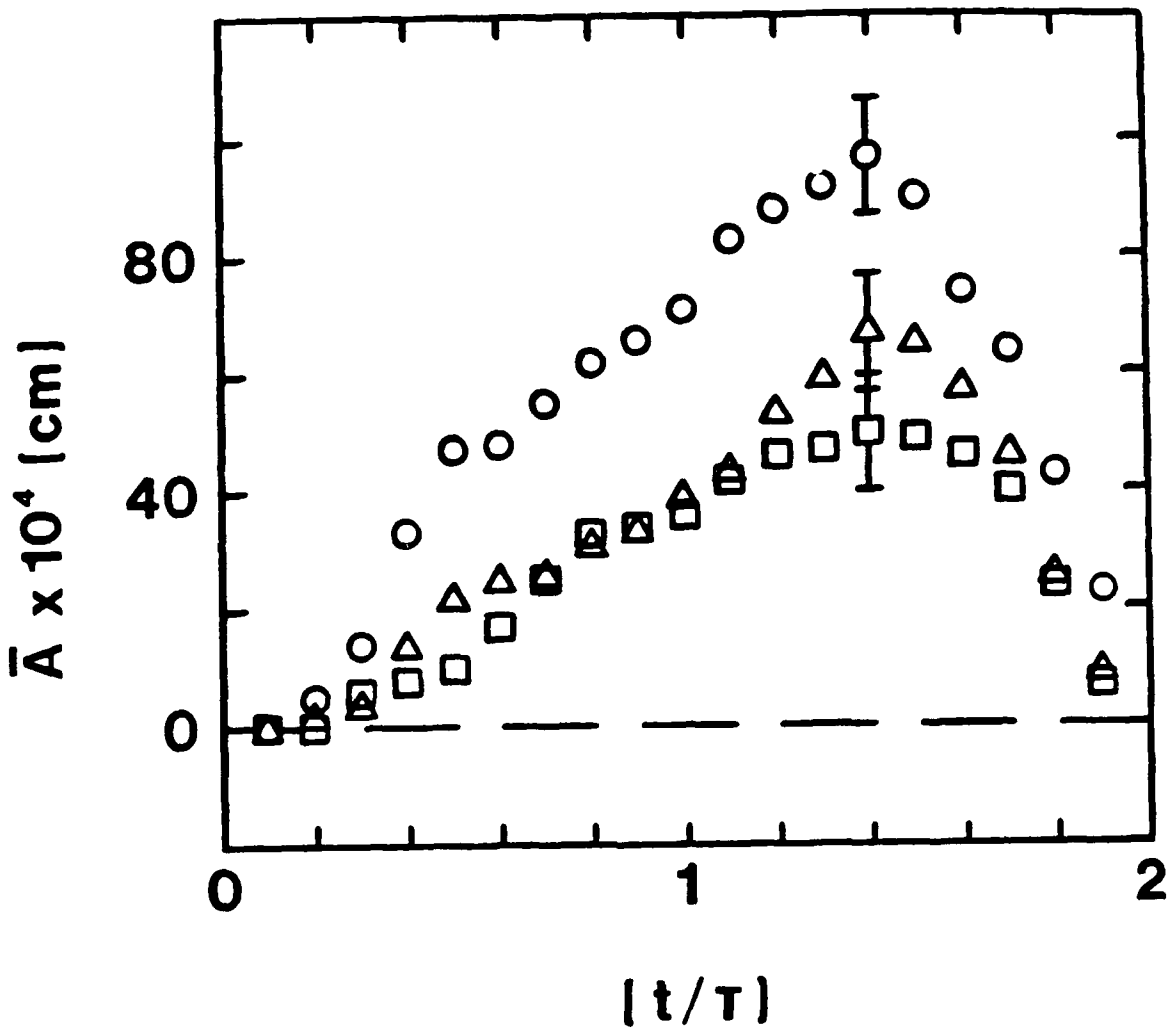

FIGURE 4-16A. Composite deformation amplitude versus dimensionless time for bubbles in DH2O and dilute aqueous PAM solutions.
(ω = 575 rpm , $\dot{\gamma}$ = 170 sec^{-1})

symbol	fluid
○	DH2O
△	DH2O+500PAM
□	DH2O+1000PAM

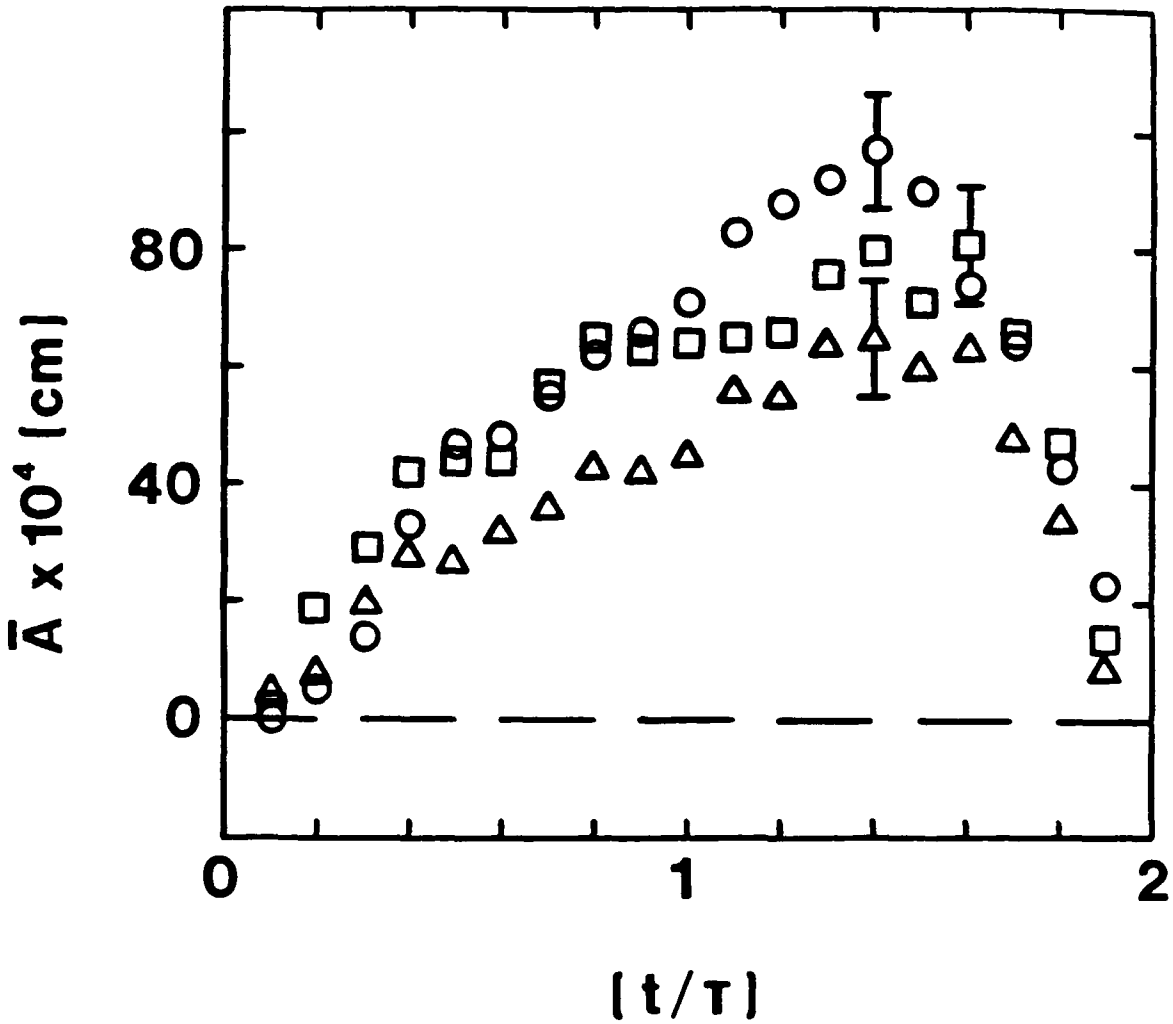

FIGURE 4-16B. Composite deformation amplitude versus dimensionless time for bubbles in DH2O and dilute aqueous PEO solutions.
(ω = 575 rpm , $\dot{\gamma}$ = 170 sec^{-1})

symbol	fluid
○	DH2O
□	DH2O+500PEO
△	DH2O+1000PEO

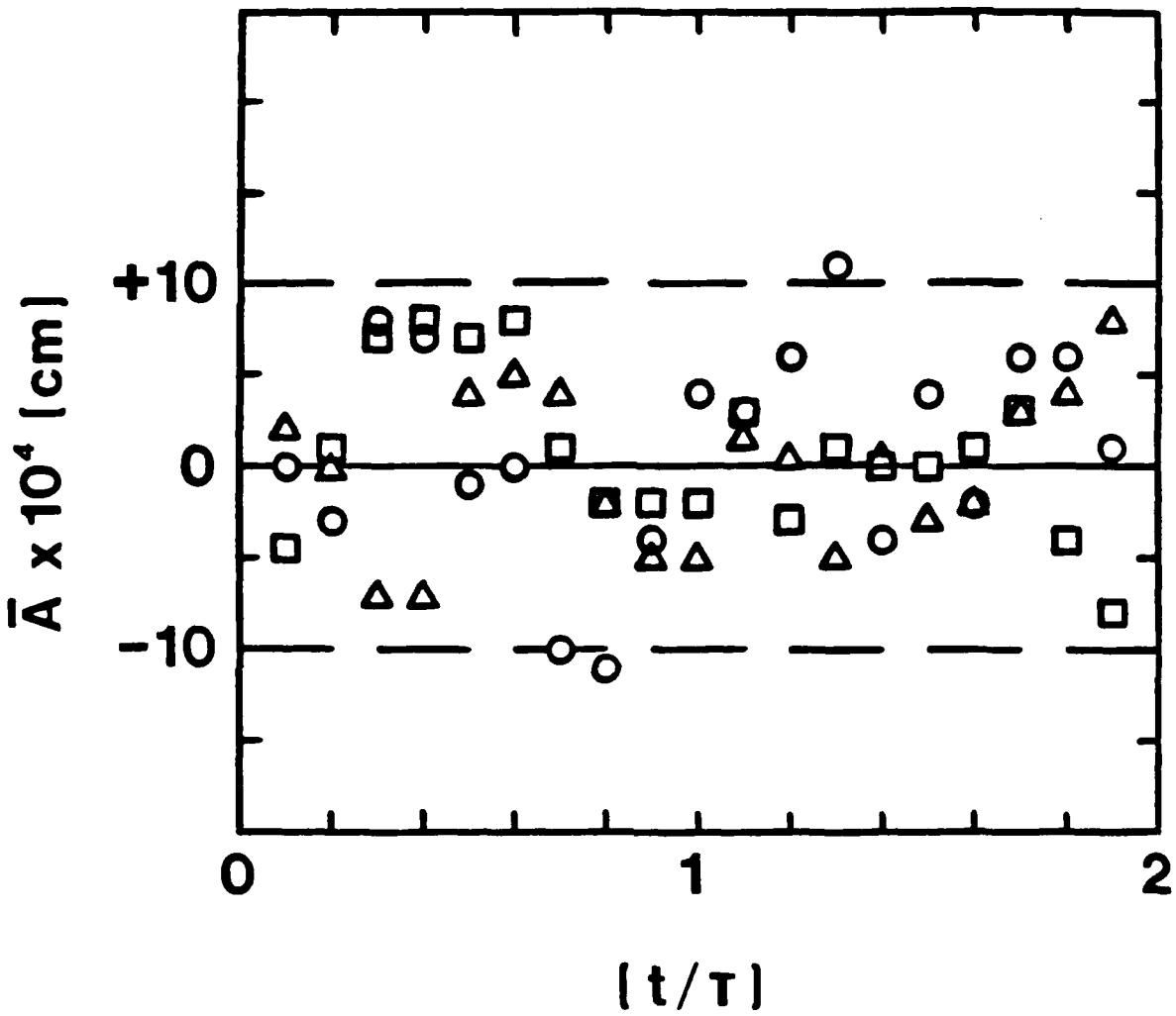

FIGURE 4-23. Composite deformation amplitudes versus dimensionless time for bubbles in quiescent GLY(1:1), GLY(1:1)+PAM and GLY(2:1).

symbol	fluid
○	GLY(1:1)
△	GLY(1:1)+500PAM
□	GLY(2:1)

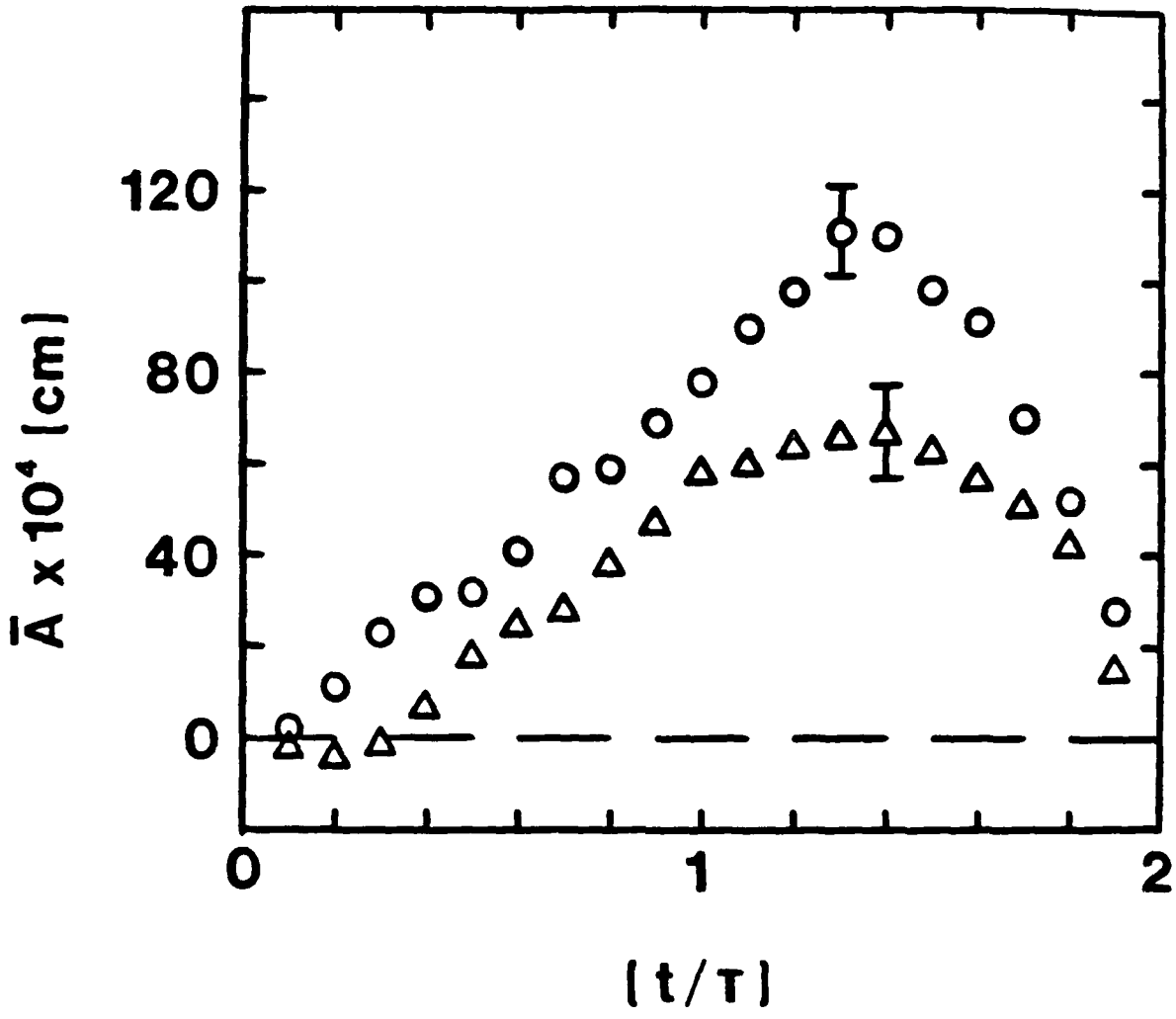

FIGURE 4-22C. Composite deformation amplitude versus dimensionless time for bubbles in GLY(1:1) and GLY(1:1)+PAM.
(ω = 575 rpm , $\dot{\gamma}$ ≈ 170 sec^{-1})

symbol	fluid
○	GLY(1:1)
△	GLY(1:1)+500PAM

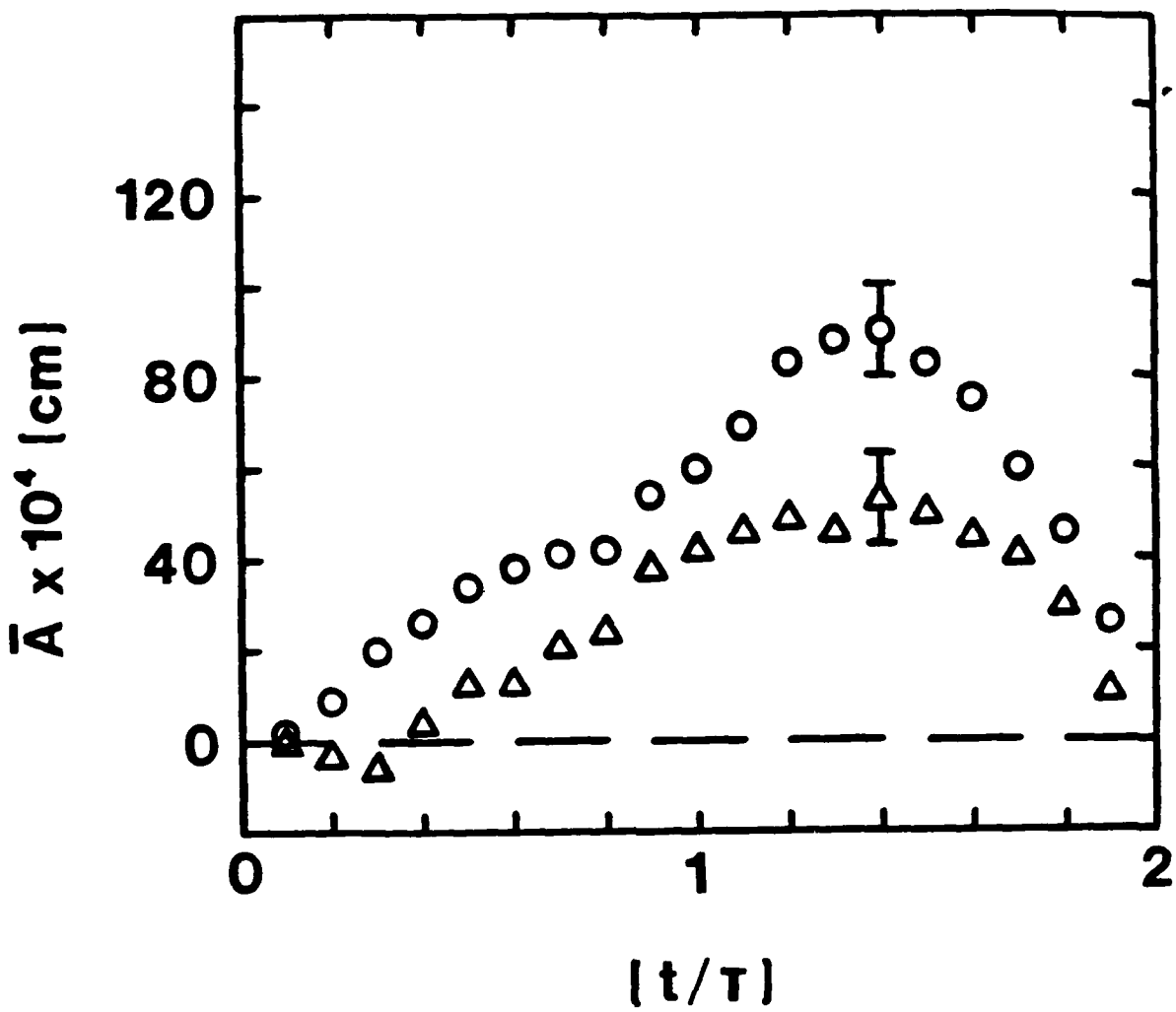

FIGURE 4-22B. Composite deformation amplitude versus dimensionless time for bubbles in GLY(1:1) and GLY(1:1)+PAM.
(ω = 480 rpm , $\dot{\gamma}$ = 140 sec^{-1})

symbol	fluid
○	GLY(1:1)
△	GLY(1:1)+500PAM

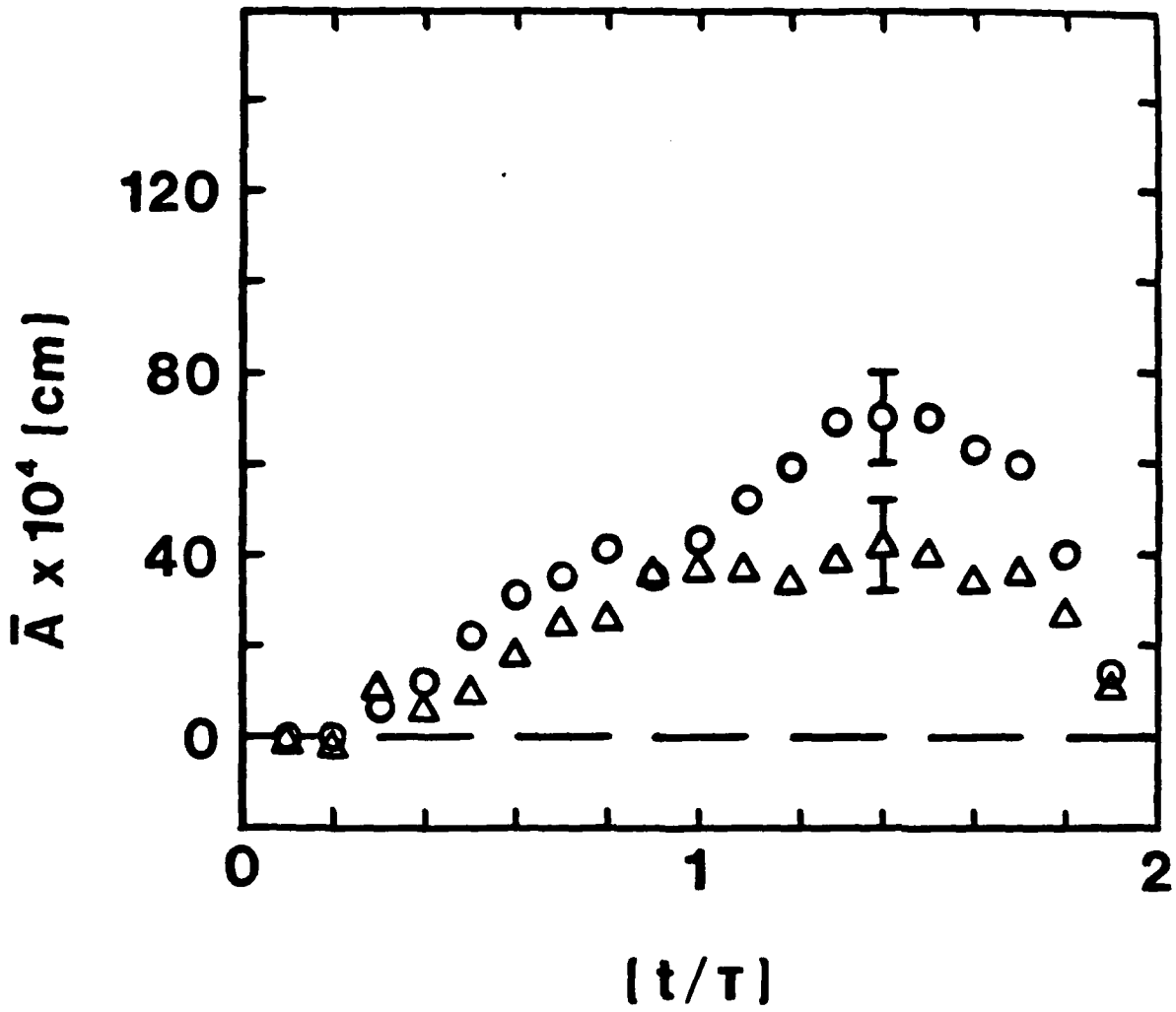

FIGURE 4-22A. Composite deformation amplitude versus dimensionless time for bubbles in GLY(1:1) and GLY(1:1)+PAM.
(ω = 360 rpm , $\dot{\gamma}$ = 105 sec^{-1})

symbol	fluid
○	GLY(1:1)
△	GLY(1:1)+500PAM

The 500 wppm polyacrylamide/glycerol solution exhibited a greater viscosity increase (from 0.064 to 0.134 poise) than the corresponding aqueous solution (from 0.01 to 0.04 poise). Again, this was taken to indicate a stronger elastic component of the fluid rheology for GLY(1:1)+500PAM relative to DH2O+500PAM. As expected, the experimental results for all three flow strengths clearly demonstrated a significant suppression of flow-induced bubble deformation.

The development of deformation amplitudes with time for both the viscoelastic solution and Newtonian solvent are shown in Figures 4-22A, 4-22B and 4-22C. Maximum deformation amplitude was found to be a linear function of flow strength in both cases. The relationships were,

$$[\max \bar{A}](10^4) = 0.1915(\omega) = 0.653(\dot{\gamma}) \qquad (4\text{-}11)$$

for the GLY(1:1) solvent and,

$$[\max \bar{A}](10^4) = 0.1145(\omega) = 0.390(\dot{\gamma}) \qquad (4\text{-}12)$$

for the GLY(1:1)+500PAM solution. Again, the control experiments indicated no appreciable bubble nonsphericity in either the glycerin solvents or solution under quiescent fluid conditions (Figure 4-23).

Quantitatively, the addition of a small amount of polymer solute

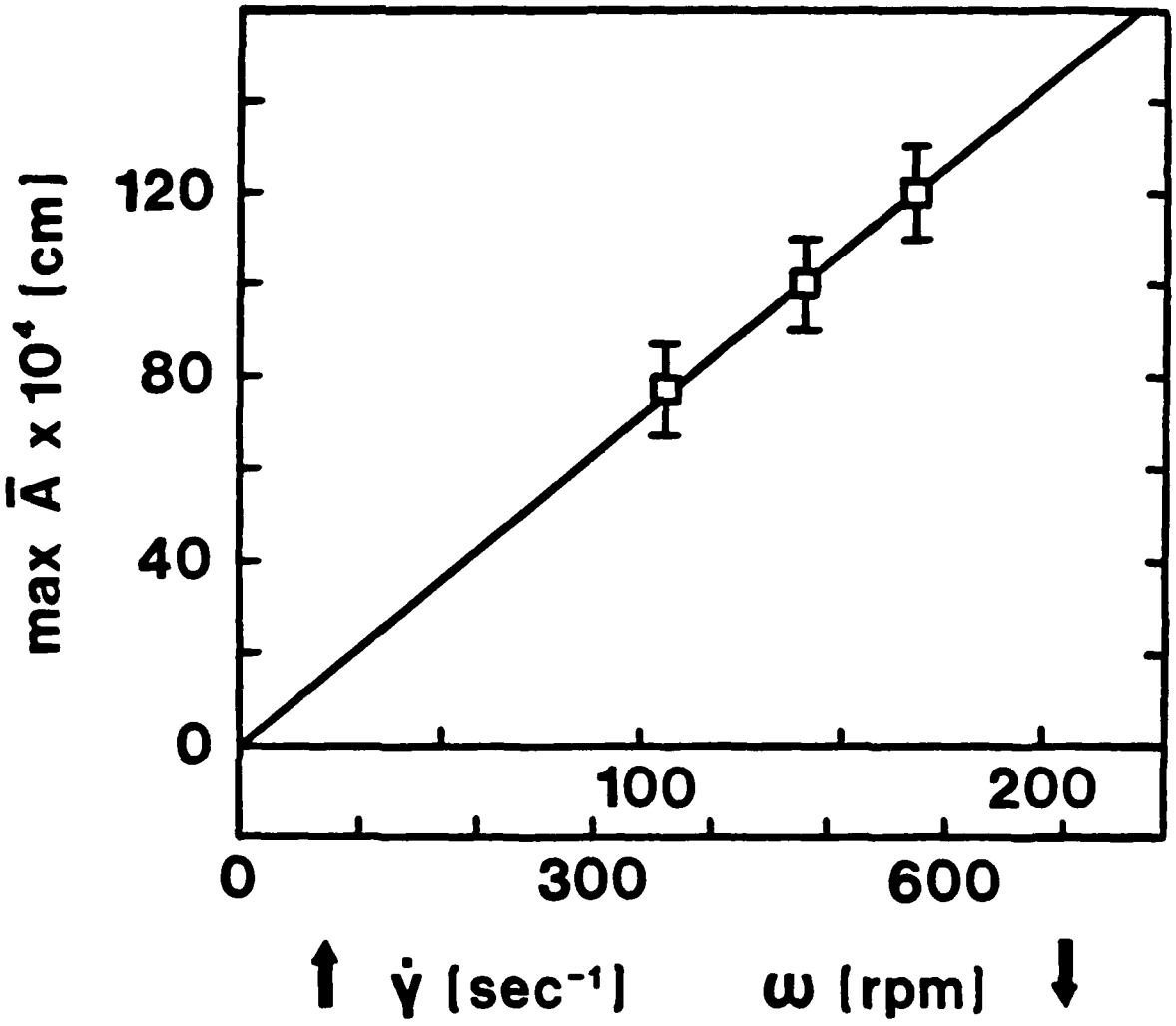

FIGURE 4-21. Maximum deformation amplitude versus flow strength for bubbles in GLY(2:1).

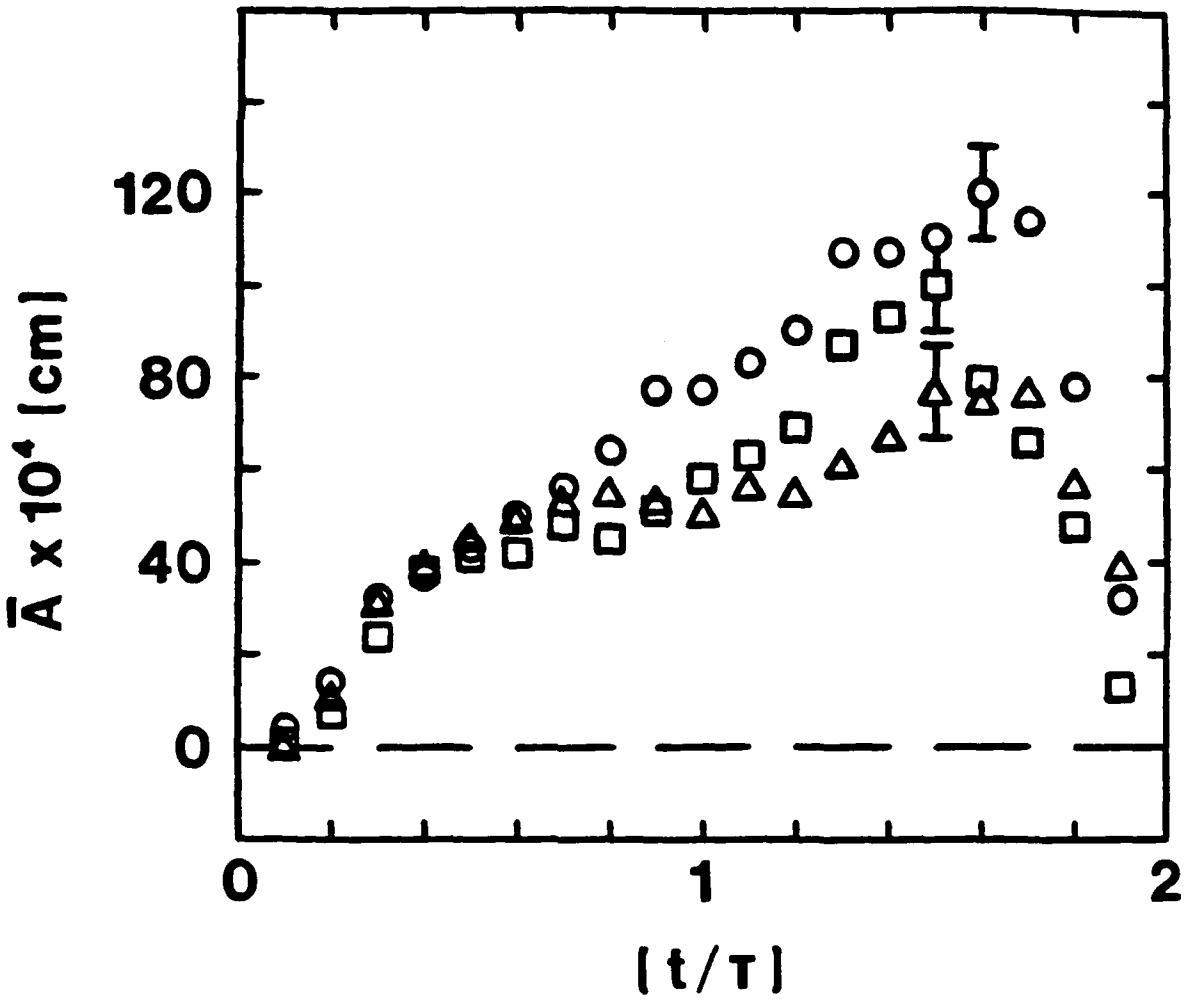

FIGURE 4-20. Composite deformation amplitudes vs. dimensionless time for bubbles in GLY(2:1).

symbol	ω(rpm)	$\dot{\gamma}$(sec^{-1})	flow
△	360	105	laminar
□	480	140	transition
○	575	170	turbulent

kinematic viscosity, ν, of this fluid was such that for the three experimental rotation speeds ($\omega \approx 360$, 480 and 575 rpm) the flow behavior went from laminar to transitional to turbulent (Figure 4-15). Despite this change in flow stability, the behavior of the bubble deformation amplitudes with time remained unaffected (Figure 4-20). The maximum deformation amplitude again followed a linear relationship with flow strength (Figure 4-21). A linear least squares fit from the origin lead to the expression,

$$[\max \bar{A}](10^4) = 0.2095(\omega)$$
$$= 0.714(\dot{\gamma}) \qquad (4\text{-}10)$$

for the GLY(2:1) solution. These results strengthened the previous conclusion (from flow visualization) that the small velocity profile modifications due to turbulence (relative to the dominant θ-component) would have no measurable effect on the experimental results or their interpretation.

Finally, the effect of solvent properties on viscoelastic deformation reduction was investigated. For these experiments the polyacrylamide solute ($C \approx 500$ wppm) was again used, however, the solvent was a glycerol/water mixture (1:1 by weight). The GLY(1:1)+500PAM solution was chosen because it was known to be highly elastic (Chang, 1974) and has been studied in several other contexts (Bird, Armstrong & Hassager, 1977). (Interestingly, polyacrylamide is substantially insoluble in nearly all organic liquids. Glycerol and ethylene glycol are two of the few exceptions (Mark et al., 1966).)

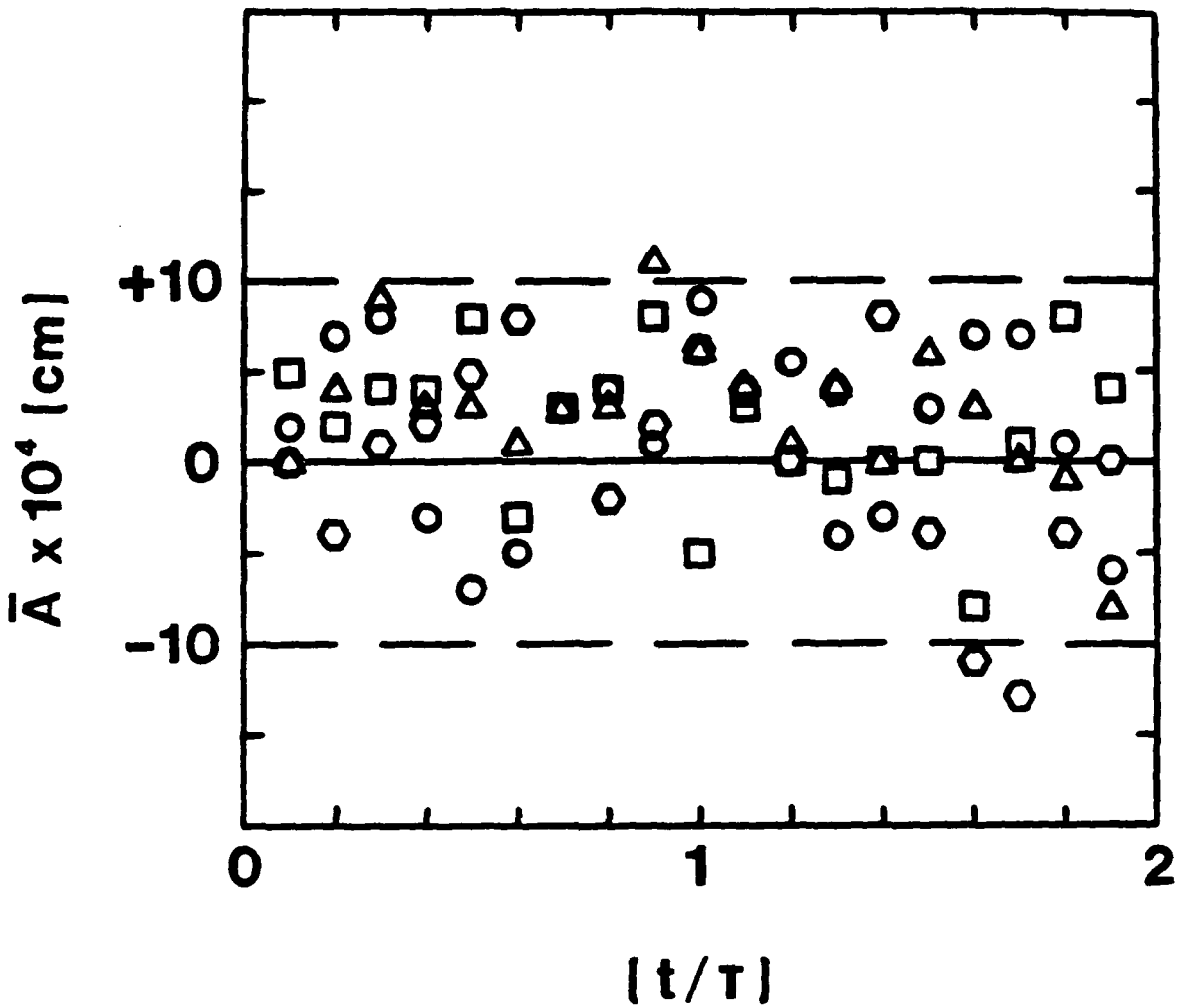

FIGURE 4-19B. Composite deformation amplitude versus dimensionless time for bubbles in quiescent dilute aqueous PEO and PEO* solutions.

symbol	fluid
□	DH2O+500PEO
△	DH2O+1000PEO
⬡	DH2O+1000PEO*
○	DH2O+2000PEO

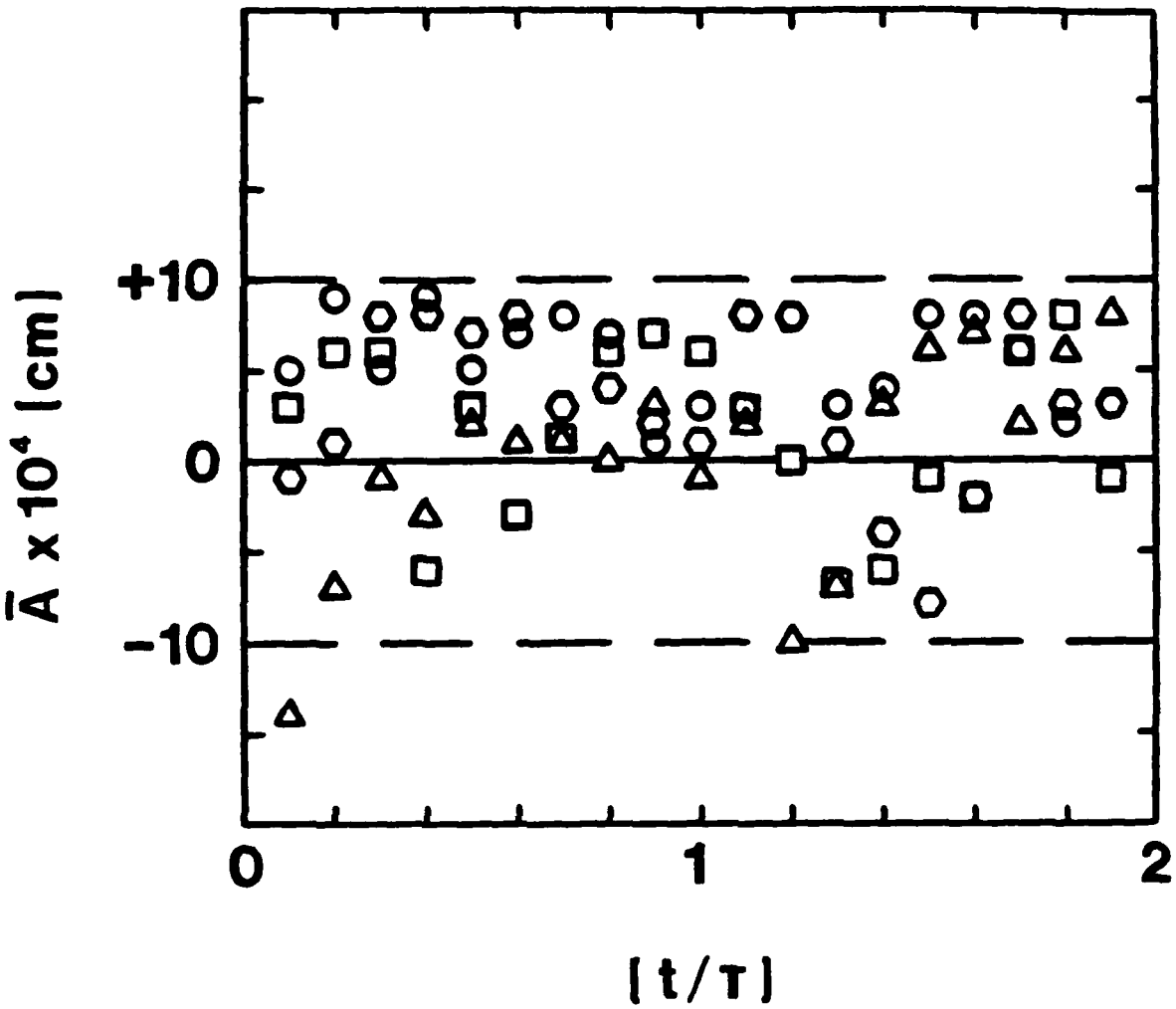

FIGURE 4-19A. Composite deformation amplitude versus dimensionless time for bubbles in quiescent DH2O and dilute aqueous PAM solutions.

symbol	fluid
○	DH2O
△	DH2O+500PAM
□	DH2O+1000PAM
⬡	DH2O+2000PAM

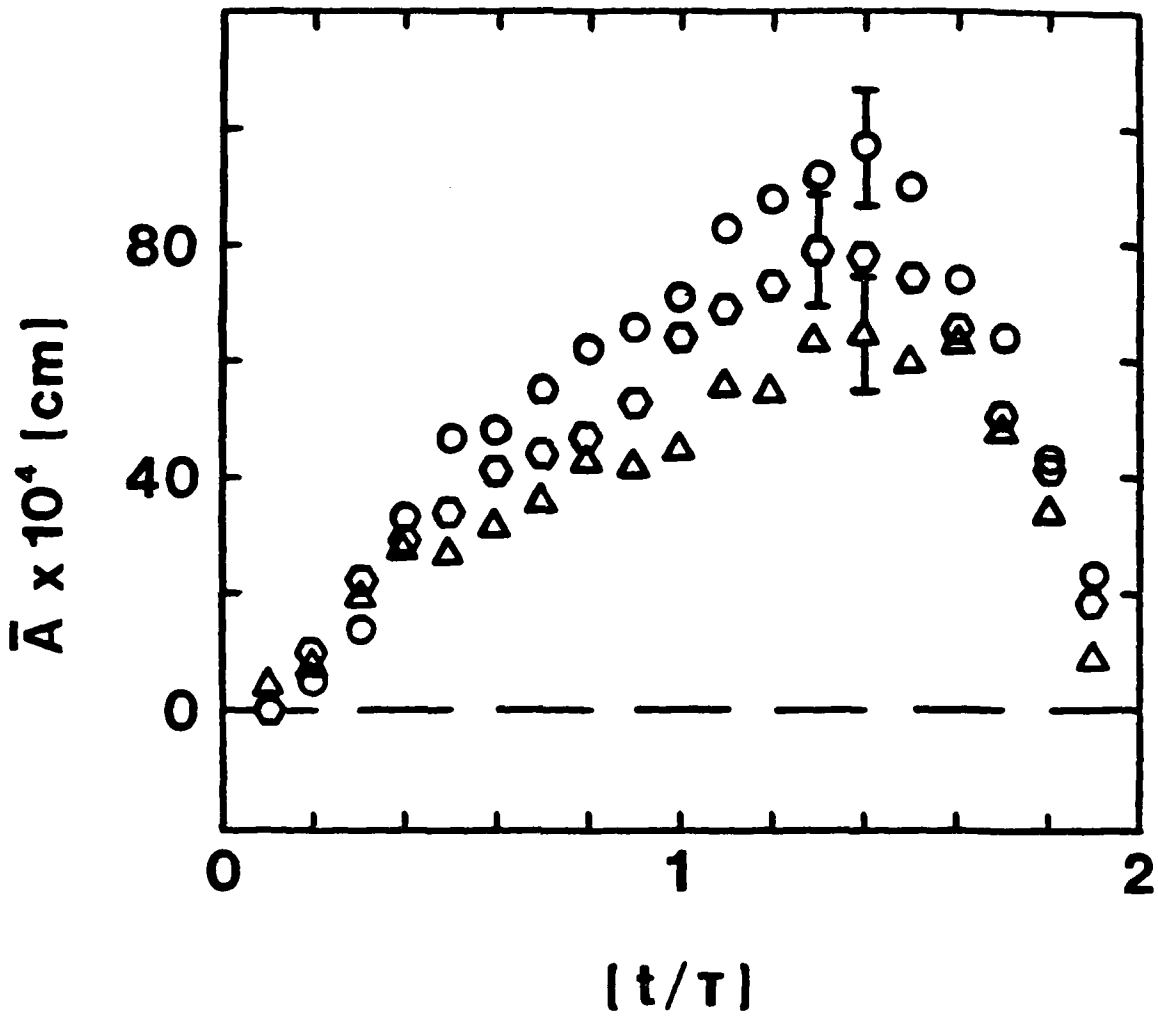

FIGURE 4-18. Composite deformation amplitudes versus dimensionless time for bubbles in DH2O and dilute aqueous PEO and PEO* solutions. (ω = 575 rpm , $\dot{\gamma}$ = 170 sec^{-1})

symbol	fluid
○	DH2O
⬡	DH2O+1000PEO*
△	DH2O+1000PEO

PAM solutions exhibited much higher viscosities than the PEO solutions, it is implied that in these dilute ($0 \leq C(\text{wppm}) \leq 1000$) aqueous solutions, the addition of polyacrylamide solutes resulted in greater fluid elasticity than did polyethylene oxide.

Similarly, kinetic thoery results based on viscosity, molecular weight and concentration data substantiated experimental results comparing different molecular weight samples of the same polymer (Figure 4-18). As expected, for similar concentrations (C = 1000 wppm), the higher molecular weight PEO solution exhibited stronger deformation suppression than the lower molecular weight PEO* solution. Reductions in both maximum amplitude and amplitude growth rate for the more elastic (higher λ) PEO solution were twice those for the less elastic (lower λ) PEO* solution.

For each flow experiment conducted, a quiescent *control* experiment was also performed in the cylindrical Couette apparatus. The results of those tests for both polyacrylamide and polyethylene oxide solutions are presented in Figures 4-19A and 4-19B respectively. The deformation amplitude (versus dimensionless time) is presented on an enlarged scale with the measurement uncertainty superimposed. As can be seen, virtually all of the data for these quiescent trials fell within the experimental bounds of sphericity ($\bar{A} = 0.000 \pm 0.001$ cm). This further demonstrated the absence of either wall or polymer effects on the spherical dynamics of these model bubbles in quiescent fluids.

Next, the effect of the laminar/turbulent transition on experimental flow deformation was examined. For these tests, a Newtonian glycerin solution (2:1 glycerol and water by weight) was prepared. The

occurred at a concentration between 500 and 1500 wppm while for polyethylene oxide this happened between 1000 and 2000 wppm. The difference seems to have resulted from distinct polymer concentration dependences of the viscous promotion and elastic suppression of flow-induced deformations. Possible behaviors for these two polymer samples are depicted by the solid curves. In all cases, however, the overall elastic effect was dominant and deformation reductions were observed.

In comparison to the polyethylene oxide solutions, these experimental results indicated stronger elastic properties for the dilute polyacrylamide solutions. This interpretation is supported by the predictions polymer kinetic theory for a Hookean dumbbell model (Bird, Armstrong, Hassager & Curtiss, 1977). In this simple model, non-Newtonian (elastic) properties are represented by a relaxation time, λ given by,

$$\lambda \simeq \frac{\eta - \eta_s}{nkT} \tag{4-9A}$$

$$\simeq (\eta - \eta_s)\left(\frac{M}{\rho C N_{av} kT}\right) \tag{4-9B}$$

where η and η_s are the solution and solvent viscosities respectively, n is the polymer number density, M is the polymer molecular weight, C is the polymer concentration, ρ is the solution density, N_{av} is Avagadro's number, k is Boltzmann's constant and T is the absolute temperature. Since for similar concentrations of similar molecular weight samples the

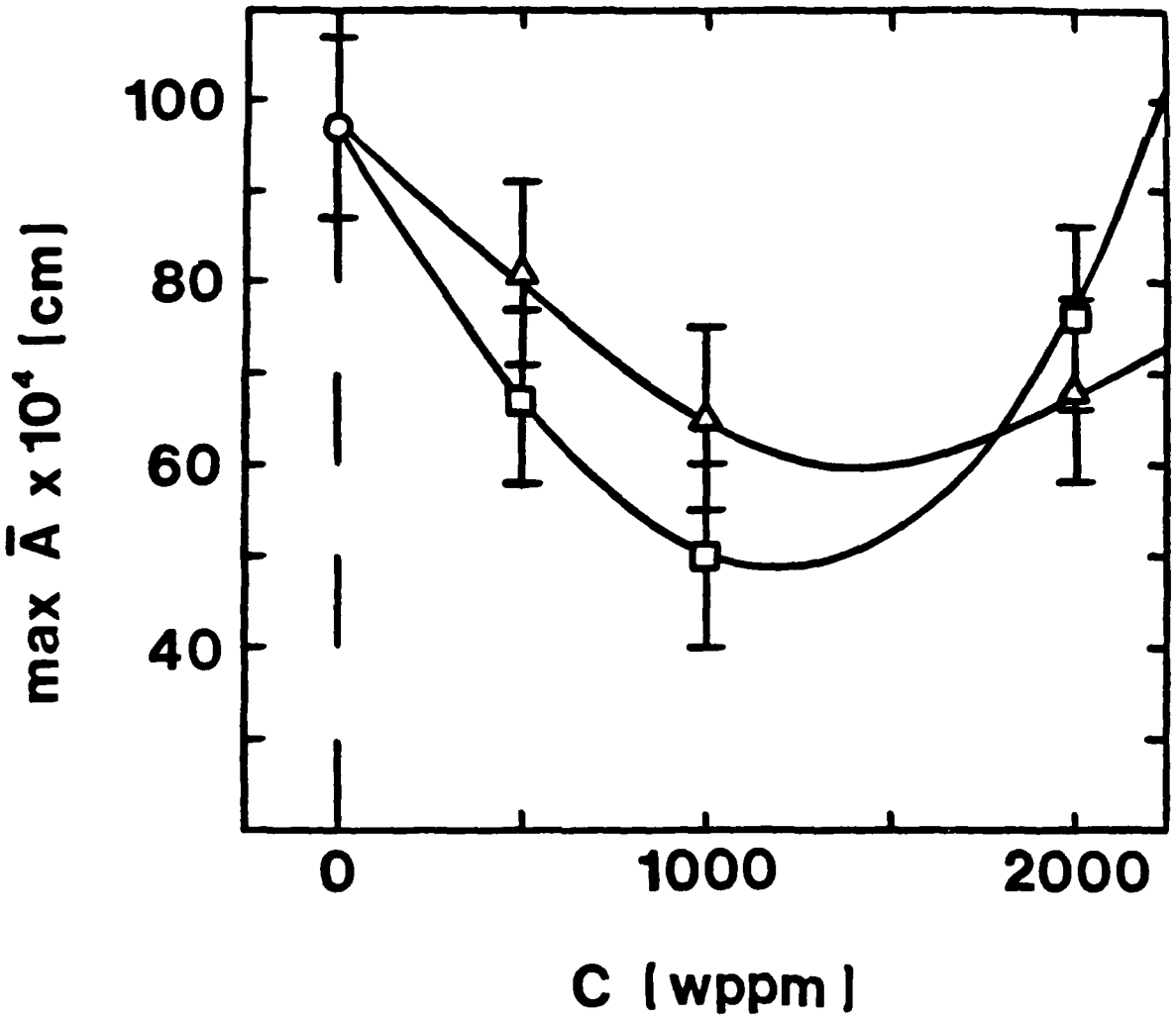

FIGURE 4-17. Maximum deformation amplitudes versus polymer concentration for bubbles in dilute aqueous PAM and PEO solutions. ($\omega \approx 575$ rpm , $\dot{\gamma} \approx 170$ sec^{-1})

symbol	fluid
○	DH2O
□	DH2O+PAM
△	DH2O+PEO

resulted in a 40% reduction of the maximum deformation amplitude (also of the deformation growth rate) for this GLY(1:1) solvent (Figure 4-24). For an aqueous solution of similar concentration the reduction of the maximum deformation amplitude was only 30%. This result is in line with the previously discussed kinetic theory (Hookean elastic dumbbell) interpretation of the rheological data.

The qualitative success of this explanation can be shown by a comparison of deformation suppression in three polymer solutions exhibiting varying degrees of elasticity. As seen in Table 4-8A, for similar concentration, molecular weight and flow strength, the ratio of maximum amplitude for solution to solvent (max $\bar{A}$/max $\bar{A}_s$) implies greater deformation suppression with increasing elasticity (De). Similarly for identical concentration, flow strength and solvent, deformation amplitude reduction is seen to increase with fluid elasticity (Table 4-8B).

However, there are serious limitations to quantitative comparisons of deformation suppression which are based on this simplistic kinetic theory model. For example, the model predicted no shear-thinning of the polymer solutions. This inconsistency made comparisons of experiments under different flow conditions essentially meaningless. Also, the concentration dependence of the predicted relaxation times was found to be inconsistent. For aqueous polyacrylamide solutions the relaxation time was unrealistically predicted to decrease with increasing concentration. This is not surprising since the kinetic theory model assumes no interactions between polymer molecules. Because of this assumption, it is only rigorously valid for solutions at infinite dilution.

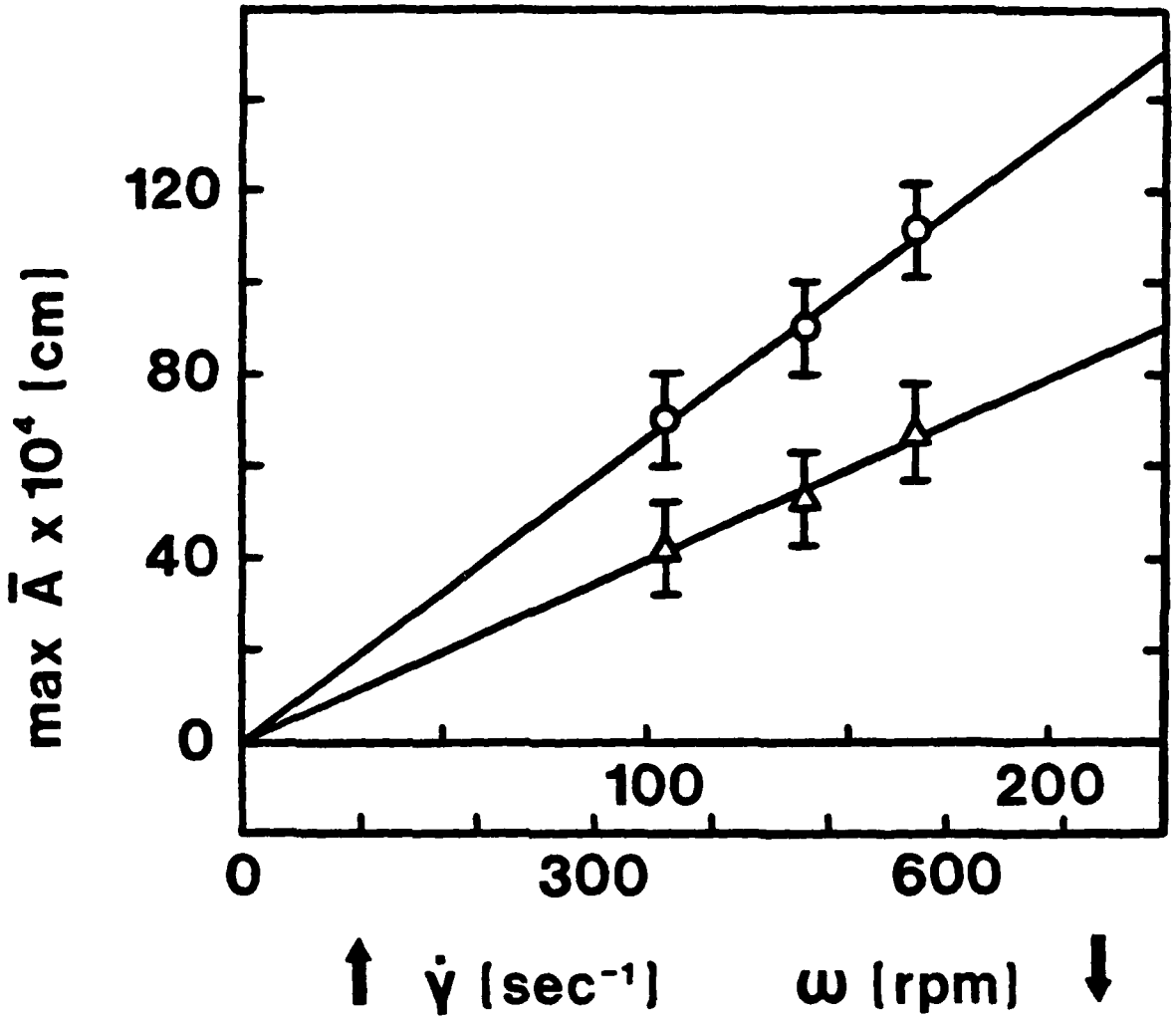

FIGURE 4-24. Maximum deformation amplitudes versus flow strength for bubbles in GLY(1:1) and GLY(1:1)+500PAM.

symbol	fluid
○	GLY(1:1)
△	GLY(1:1)+500PAM

solution	λ(sec)	De($\dot{\gamma}\lambda$)	(max $\bar{A}$/max $\bar{A}_s$)
DH2O+500PEO	0.001	0.16	81/97 ≈ 0.835
DH2O+500PAM	0.013	2.21	67/97 ≈ 0.691
GLY(1:1)+500PAM	0.027	4.65	67/111 ≈ 0.604

concentration : C ≈ 500 wppm

molecular weight : M ≈ 5-6 x 10^6

flow strength : ω ≈ 575 rpm , $\dot{\gamma}$ ≈ 170 sec^{-1}

TABLE 4-8A. Comparison of deformation reduction with elasticity for similar polymer concentration, molecular weight and flow strength.

solution	λ(sec)	De($\dot{\gamma}\lambda$)	(max $\bar{A}$/max $\bar{A}_s$)
DH2O+1000PEO*	0.00005	0.0025	79/97 ≈ 0.814
DH2O+1000PEO	0.0025	0.43	65/97 ≈ 0.670
DH2O+1000PAM	0.011	1.83	50/97 ≈ 0.515

concentration : C ≈ 1000 wppm

solvent : DH2O

flow strength : ω ≈ 575 rpm , $\dot{\gamma}$ ≈ 170 sec^{-1}

TABLE 4-8B. Comparison of deformation reduction with elasticity for similar polymer concentration, solvent and flow strength.

Thus, it has been concluded that direct comparisons of deformation suppression could only be made for closely related sets of experimental data (equivalent polymer concentration and flow strength).

These observations of the viscoelastic suppression of the flow-induced bubble deformation can be related to hydraulic cavitation phenomena through the theoretical results of Chahine and Bovis (1981). Those researchers modelled spherical and nonspherical bubble dynamics to obtain the liquid pressure field resulting from bubble collapse near a solid boundary. Their predictions indicated that nonspherical bubble collapse generates pressures at the wall which can be orders of magnitude higher than for the spherical case. The present research has shown bubble nonsphericity in an external flow field to be significantly diminished by fluid viscoelasticity. Thus for hydraulic cavitation, which combines strong external flow with the presence of a solid boundary, the implied effect of viscoelastic polymer solutes would be to decrease wall pressures upon bubble collapse This decrease could possibly result in the macroscopic observations of reduced non-Newtonian cavitation intensity, noise or even damage.

MODEL APPLICATION RESULTS

As previously discussed, an additional goal of this research program has been to apply the most recent modelling efforts of Hara (1983) to the present experimental situation. In this way, the independent theoretical predictions for flow-induced dynamic bubble deformation in both viscous and viscoelastic fluids could be compared to these significant experimental results. The initial model application by Hara dealt mainly with nonspherically initiated cavities in both quiescent distilled water and dilute polyacrylamide solutions (C ≈ 500 wppm). Good agreement between model predictions and experimental results were reported (see Chapter 2). The effects of fluid viscoelasticity in this situation were found to be small, though *non-negligible*.

As a starting point for the present work, the dynamics of nonspherically initiated bubbles in a quiescent viscous glycerol/water mixture ($\eta \approx 1.05$ poise) have been examined (see Figure 4-5). The reduced experimental data describing this cavity have been presented in Table 4-3B. This experiment differed from those of Hara because the high-speed photographic system used to record the data resulted in less experimental uncertainty for both bubble radius (± 1-2% versus ± 2-4%) and deformation amplitude (± 5-10% versus ± 10-20%).

Again following Hara's modelling procedure, a smooth fit of the experimental radius profile, $R_{fit}(t)$, was made using a Fourier sine

series approximation of the form,

$$R_{fit}(t) = \sum_{i=1}^{5} C_i \sin[(2i-1)\pi(t/\Delta t)] \tag{5-1A}$$

where C_i is the amplitude of the ith wave given by,

$$C_i = \frac{2}{\Delta t} \int_0^{\Delta t} R(t) \sin\left(\frac{(2i-1)\pi t}{\Delta t}\right) dt \tag{5-1B}$$

and Δt is the total bubble lifetime. For a composite sequence of several bubbles, the total bubble lifetime (Δt) is replaced with twice the experimental collapse period (2τ) in equations 5-1A and 5-1B. This composite quantity is determined from the relationship,

$$2\tau = 2\ (\tau/R_0)\ \overline{R_0} \tag{5-2}$$

where (τ/R_0) is the normalized experimental collapse time (equation 4-2) and $\overline{R_0}$ is the composite maximum bubble radius for the experiments of interest. The value of each coefficient (C_i) was determined by a numerical integration of the experimental data for the equivalent spherical bubble radius. From the series representation of the bubble radius, values of R were interpolated at points within the experimental domain ($0 \le t \le \Delta t$). The functions $\dot{R}(t)$ and $\ddot{R}(t)$ were generated from term-by-term integration(s) of the series. A sample calculation of this procedure is presented in Appendix B.

Using these functions, as well as the external flow field boundary condition, Hara's model predicted the amplitude of bubble nonsphericity (A) and the derivative of this amplitude with respect to time (dA/dt). For this quiescent case (no external flow), model initiation included the specification of both an initial deformation amplitude, a_0 and an initial amplitude velocity, $\dot{a}_0$. The values for these and other pertinent model and experimental parameters are given in Table 5-1. The possible ranges of values for the two initiation parameters,

$$0.10 \leq a_0 \text{ (cm)} \leq 0.15$$

$$-1500 \leq \dot{a}_0 \text{ (cm/sec)} \leq +500$$

were constrained by the uncertainty in extrapolating the experimental data back to time zero. The values which were chosen (Table 5-1) produced the numerical result which best followed the experimental data (Figure 5-1). Although variations in these *initial conditions* produced significant quantitative differences in the theoretical results (amplitude versus time), the qualitative behavior of the deformation amplitude with time remained unchanged.

As expected, this behavior was qualitatively similar to that observed and reported by Hara for cavities in both water and dilute polymer solutions (see Figures 2-6A and 2-6B). These similarities for solutions of such different rheological properties indicated the degree to which inertial effects dominate the cavitation phenomenon. However, quantitative differences arising from the viscous effects of the glycerol

spherical parameters :

maximum radius :	$R_0 \approx 0.313$ cm
bubble lifetime :	$\Delta t \approx 680$ μsec
Fourier coefficients :	$C_1 = 0.354$ cm
	$C_2 = 0.057$ cm
	$C_3 = 0.022$ cm
	$C_4 = 0.012$ cm
	$C_5 = 0.006$ cm

nonspherical parameters :

initial amplitude :	$a_0 = 0.130$ cm
init. amp. velocity :	$\dot{a}_0 = +500$ cm/sec

fluid properties :

density :	$\rho \approx 1.22$ g/cm^3
viscosity :	$\eta \approx 1.05$ poise
surface tension :	$\sigma \approx 64$ dyne/cm

TABLE 5-1. Numerical and experimental parameters for a nonspherically initiated bubble in glycerol/water. (see Figure 4-5)

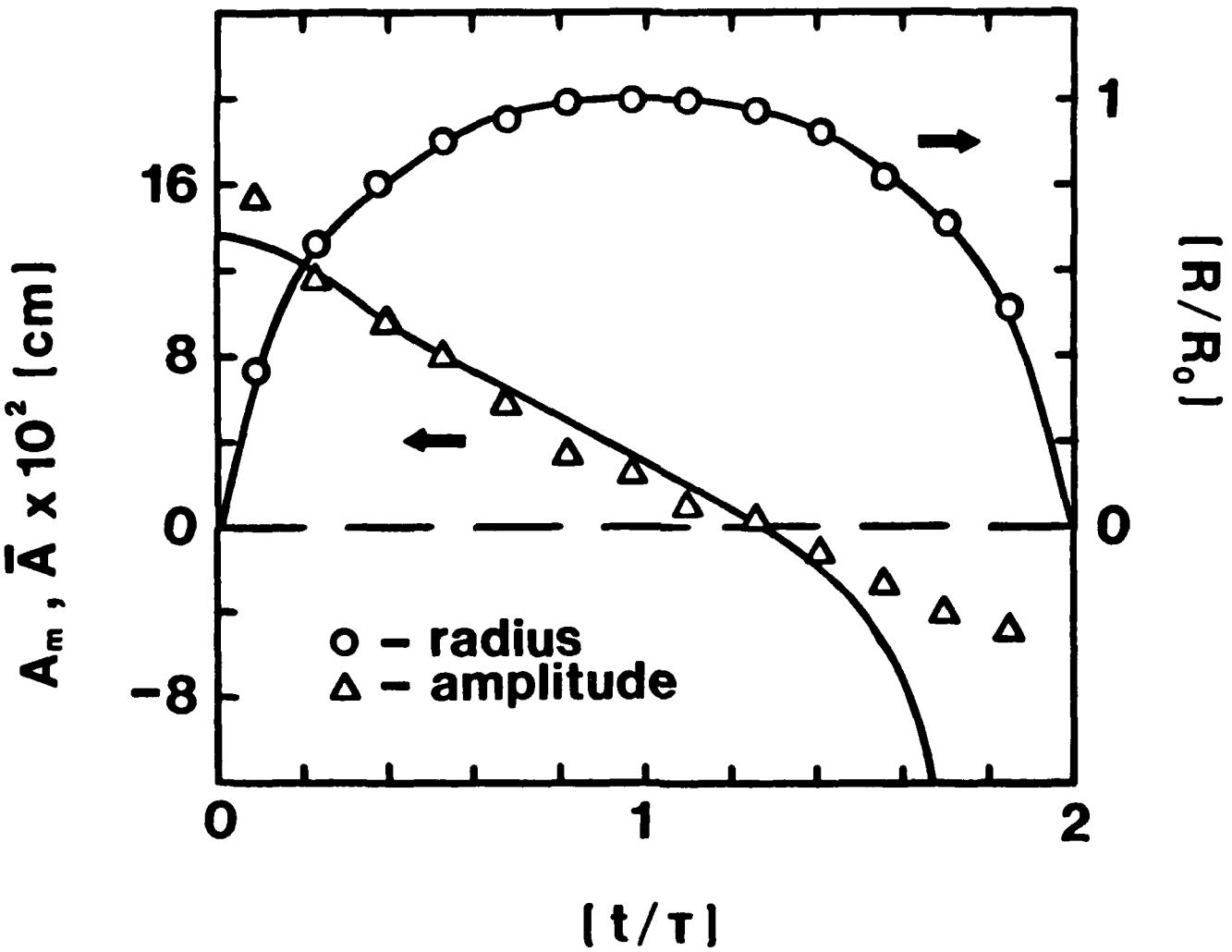

FIGURE 5-1. Comparison of experiment and theory for dimensionless radius and deformation amplitude versus dimensionless time of nonspherically initiated bubble dynamics in quiescent glycerol/water.

solution can be seen. In its relation to bubble oscillation, both spherical and nonspherical, the effect of viscosity has been interpreted as a damping mechanism (Lauterborn, 1976; Inge & Bark, 1982; Hara, 1983). In the context of Figure 5-1 compared to Figures 2-6A and 2-6B, the increased damping can be seen as (a) a steeper drop in deformation amplitude with time and (b) a less pronounced inflection in deformation amplitude near maximum bubble size ($[t/\tau] \approx 1$). These changes further demonstrate the increased sensitivity of the behavior of these nonspherical cavitation bubbles to fluid rheology over the simpler spherical bubble dynamics, even with no imposed flow. However, as Hara reported, an exterral flow field, acting as the sole source of system nonsphericities, strongly influenced bubble dynamics through fluid rheology. It is this most important aspect of Hara's model which has been applied to the aforementioned experimental results (see Chapter 4).

According to Hara (1983), the model could be used to generate a realistic fluid history by postulating a continuous external flow over all past times ($-\infty < t < 0$) which continued throughout the bubble lifetime ($0 \le t \le \Delta t$). This flow took the form of a sinusoidally oscillating uniaxial extensional field described by,

$$v \rightarrow A^*(t)\, e^{i\Omega t}\, \nabla[r^2 Y_2^0(\theta,\phi)] \qquad (5\text{-}3)$$

$$\text{as} \quad r \rightarrow \infty$$

where $A^*(t)$ is the complex model flow amplitude function and Ω is the flow oscillation frequency. In addition, the model flow strength

decayed exponentially from time zero for both positive and negative times according to,

$$A^*(t) = A^* \exp(+t/\zeta) \qquad (5\text{-}4A)$$

$$\text{for} \quad -\infty < t \leq 0$$

and

$$A^*(t) = A^* \exp(-t/t_{decay}) \qquad (5\text{-}4B)$$

$$\text{for} \quad 0 \leq t < \infty$$

where A^* is the complex flow amplitude constant and ζ and t_{decay} are the decay constants for negative and positive times respectively. The adaptation of this flexible model to the experimental flow conditions required the specification of most of the adjustable model parameters. The appropriate physical situation was a two-dimensional shear field of constant magnitude which resulted in bubble elongation along the axis of shear. The simulation of steady flow required that the flow decay constants (ζ and t_{decay}) had values of negative and positive infinity respectively. In addition, the flow frequency (Ω) had to be specified as positive and infinitesimally small. For the purpose of numerical

computation the values of these parameters were approximated as follows,

$$(1/\zeta) \approx 10^{-10}\ \mathrm{sec}^{-1}$$

$$(1/t_{decay}) \approx 10^{-10}\ \mathrm{sec}^{-1}$$

$$\Omega \approx 10^{-10}\ \mathrm{sec}^{-1}.$$

Finally the flow oscillation phase, given by the real and imaginary components of the complex flow amplitude constant (A*), was required to be zero. Thus, the flow amplitude constant had to be real. With these constraints, a steady flow could be specified by a single model parameter, Re(A*), the real flow amplitude.

Given the inherent geometric differences between the model flow field and the experimental flow system, this model flow parameter was assumed to be freely adjustable. As substantiated by experimental results, the predicted magnitude of the theoretical bubble deformation [A_m] was determined by numerical trials to be a linear function of the model flow strength parameter (Figure 5-3 and Table 5-2). However, in contrast to the experimental results, predictions of deformation amplitudes were found to depend on maximum bubble size. The steady-state deformation relationship (equation 3-3) suggested a quadratic dependence of deformation amplitude on bubble radius ($A \propto R^2$). It is possible that such behavior did occur experimentally, but that it was unobservable beause of (a) the small amount of bubble nonsphericity and/or (b) the large amount of scatter in the raw data. Thus to

facilitate comparisons of theoretically and experimentally generated bubble deformation profiles, a normalization of the model predictions (based on this suggested quadratic relationship) was made through variation of the model flow strength parameter with bubble size (equations 5-5 and 5-7).

To determine the anticipated linear relationship between theoretical and experimental flow strengths (Re(A*) and ω or $\dot{\gamma}$), *best fit curves* for the DH2O flow deformation results (see Figure 4-12) were obtained by varying Re(A*) to match the theoretical maximum deformation amplitudes [max A_m] to the experimental values [max $\overline{A}$]. Figure 5-2 shows one such best fit of the experimental flow deformation data for DH2O at a rotation rate of 575 rpm. These model parameters were then normalized with respect to the mean experimental maximum bubble radius ($R_m \equiv 0.45$ cm). The normalized flow strengths, ReN(A*) are given by,

$$\mathrm{ReN}(A^*) \equiv \mathrm{Re}(A^*)\ [R_0/R_m]^2 \tag{5-5}$$

where Re(A*) is the best fit model flow amplitude for each experimental DH2O flow composite. These normalized model flow parameters, when plotted against corresponding experimental flow strengths, depicted a linear relationship between model and experimental flow conditions (Figure 5-3). Linear least squares fits of ReN(A*) versus ω and $\dot{\gamma}$

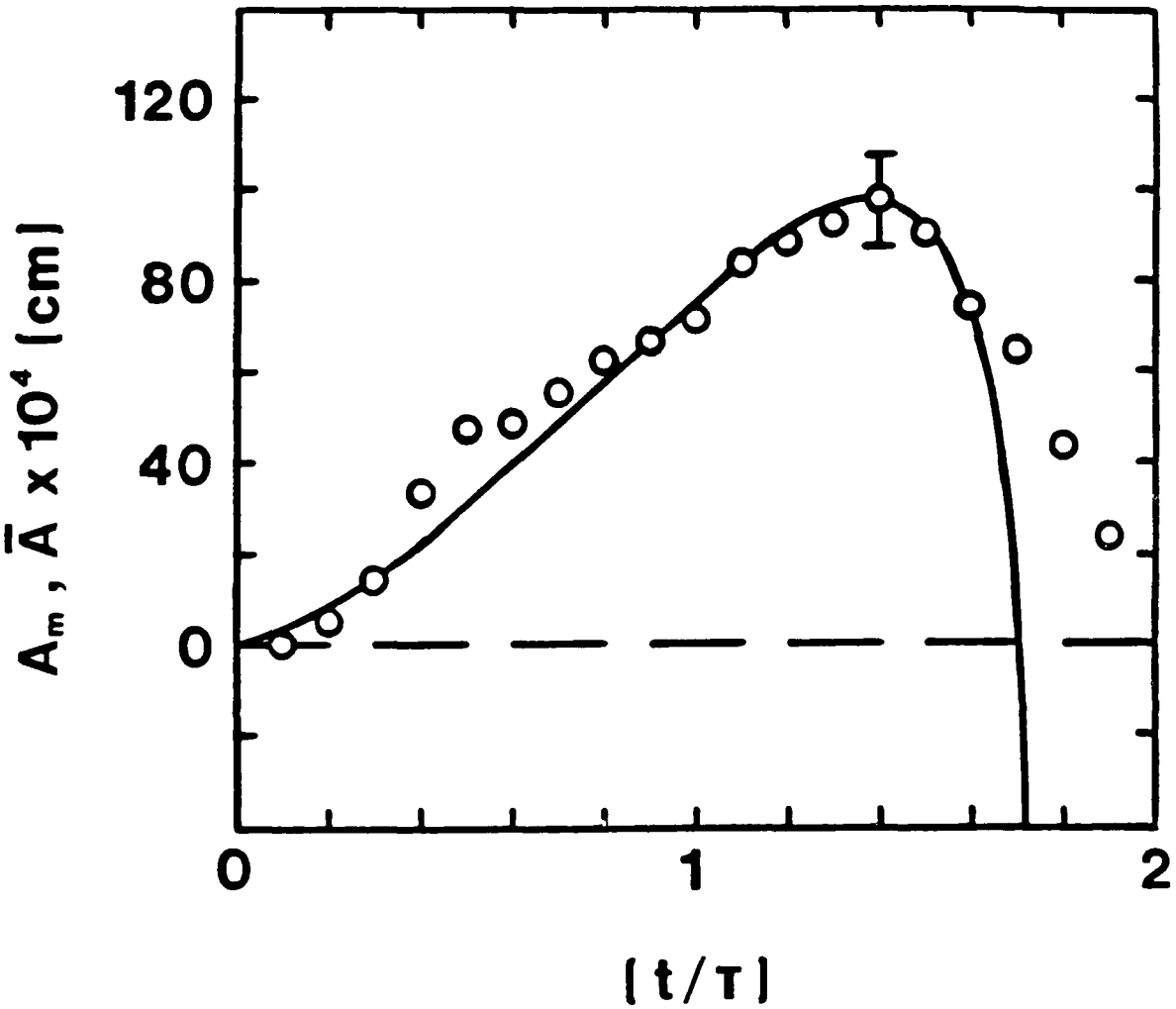

FIGURE 5-2. Comparison of experiment and best fit theory for deformation amplitude versus dimensionless time of bubbles in DH2O. (ω = 575 rpm , $\dot{\gamma}$ = 170 sec ^{1})

CONCLUSIONS AND RECOMMENDATIONS

In light of these experimental results and model application efforts, the conclusions of this research fall into two distinct (but related) areas. These are (a) Newtonian (or viscous) flow-induced cavitation bubble deformation and (b) non-Newtonian (or viscoelastic) suppression of flow-induced cavitation bubble deformation. In addition, the non-Newtonian observations have been extended, in conjunction with the results of other researchers to further explain the macroscopic effects of hydraulic cavitation inhibition in polymer solutions (see Chapter 4).

In the first category, experimental results demonstrated a linear relationship between bubble nonsphericity and imposed flow field strength. As a consequence of the transient nature of the phenomenon, observed deformations were quite small, particularly with respect to steady-state deformation predictions (0.01-0.015 cm versus 0.03-0.30 cm). Despite the small amplitudes and the extremely short time scale involved, bubble deformation dynamics displayed smooth behavior (within experimental measurement uncertainty). Model predictions of bubble nonsphericity based on an imposed uniaxial extensional flow field were in good qualitative agreement with the experimental results. The model flow amplitude (A*) was used as an adjustable parameter in developing a linear correlation between experimental and theoretical flow strengths from DH2O data and predictions. Based on this correlation, theoretical and experimental deformation results were in quantitative agreement to within ± 10-15% for all Newtonian fluids.

flow-induced deformation amplitudes displayed by these three sets of model predictions, paralleled a similar experimental relationship demonstrated by the data (see Tables 4-8A and 4-8B). As the fluid relaxation time increased, both experimental results (for solutions of similar concentration under equivalent flow conditions) and theoretical predictions (for relaxation time ranges and sets of similar solutions) exhibited stronger viscoelastic bubble deformation inhibition. However, limitations similar to those noted for the simplistic Hookean dumbbell model (see Chapter 4) were observed for these Maxwell element model predictions. In particular, this linear viscoelastic theory failed to predict the upturn in maximum deformation amplitude with increasing polymer concentration (see Figure 4-17). In this example, where increasing elasticity led to progressively decreasing nonsphericity, and in model predictions of bubble deformation in Newtonian solvents (Tables 5-2, 5-3A and 5-3B), viscous effects seem to have been underestimated. In this light, experiment and theory can only be interpreted as qualitatively consistent with each other.

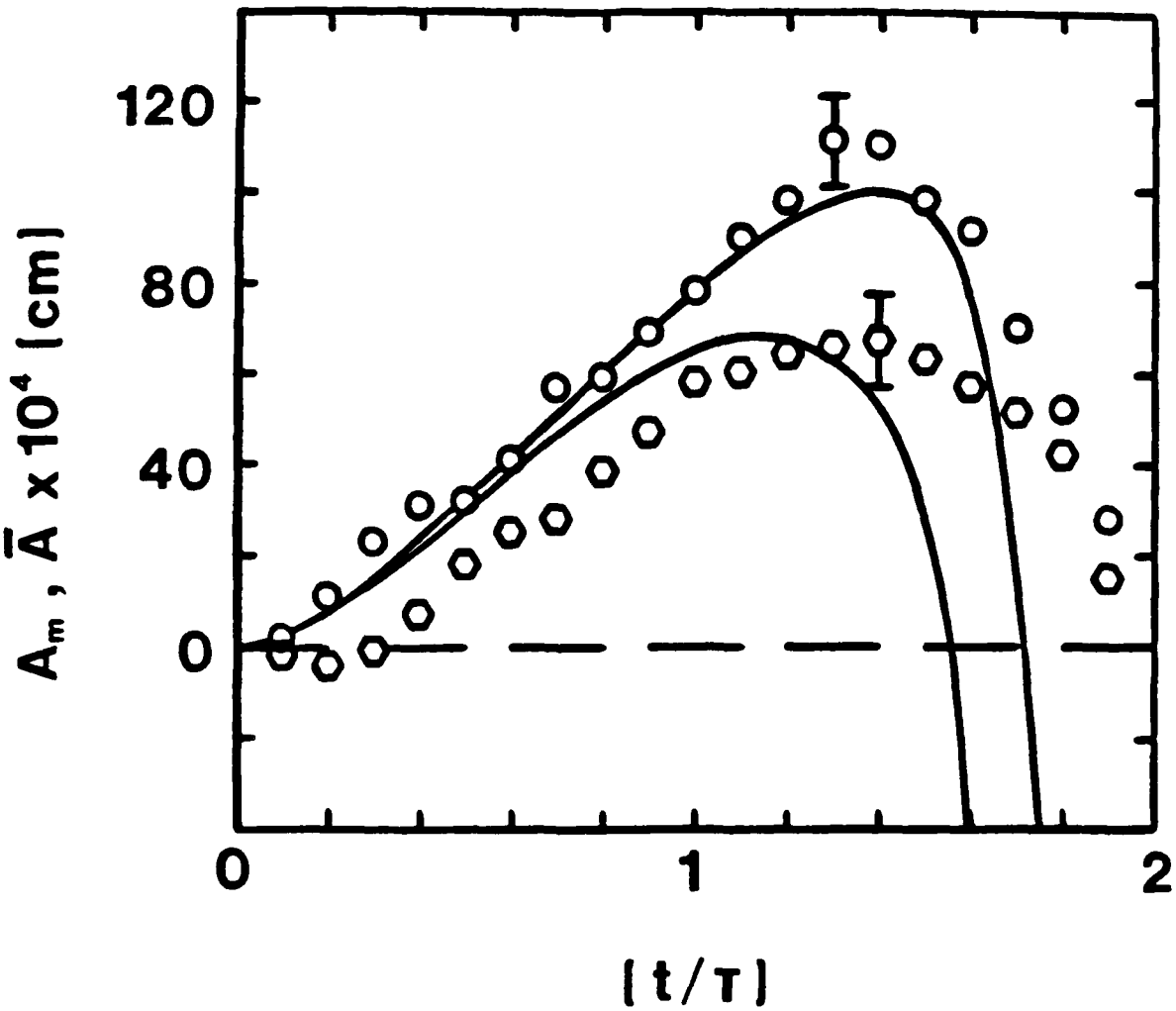

FIGURE 5-5C. Comparison of experiment and theory for deformation amplitude versus dimensionless time of bubbles in GLY(1:1) and dilute GLY(1:1)+PAM solutions.
(ω = 575 rpm , $\dot{\gamma}$ = 170 sec^{-1})

symbol	fluid
○	GLY(1:1)
⬡	GLY(1:1)+500PAM

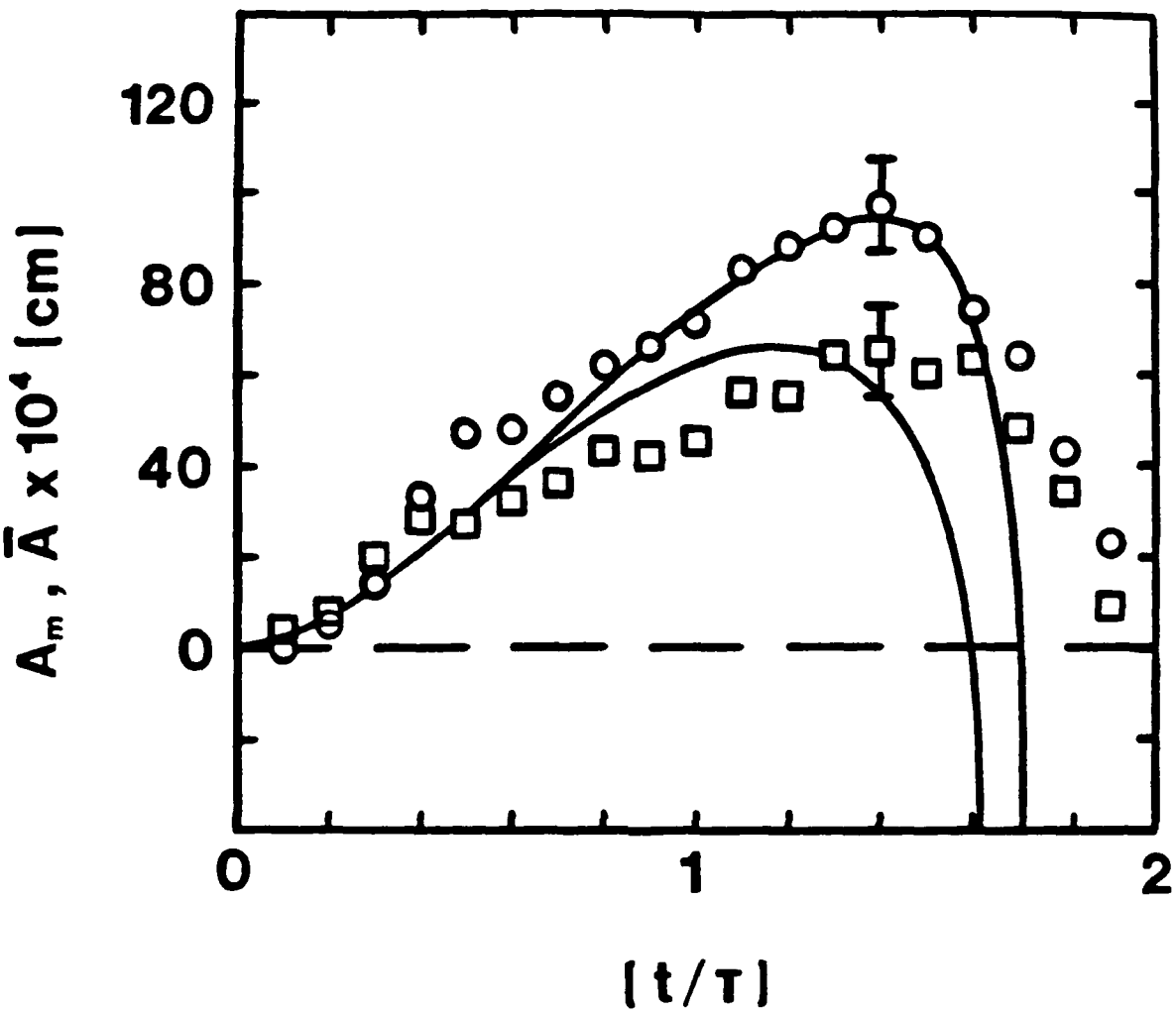

FIGURE 5-5B. Comparison of experiment and theory for deformation amplitude versus dimensionless time of bubbles in DH2O and dilute aqueous PEO solutions.
(ω = 575 rpm , $\dot{\gamma}$ = 170 sec^{-1})

symbol	fluid
○	DH2O
□	DH2O+1000PEO

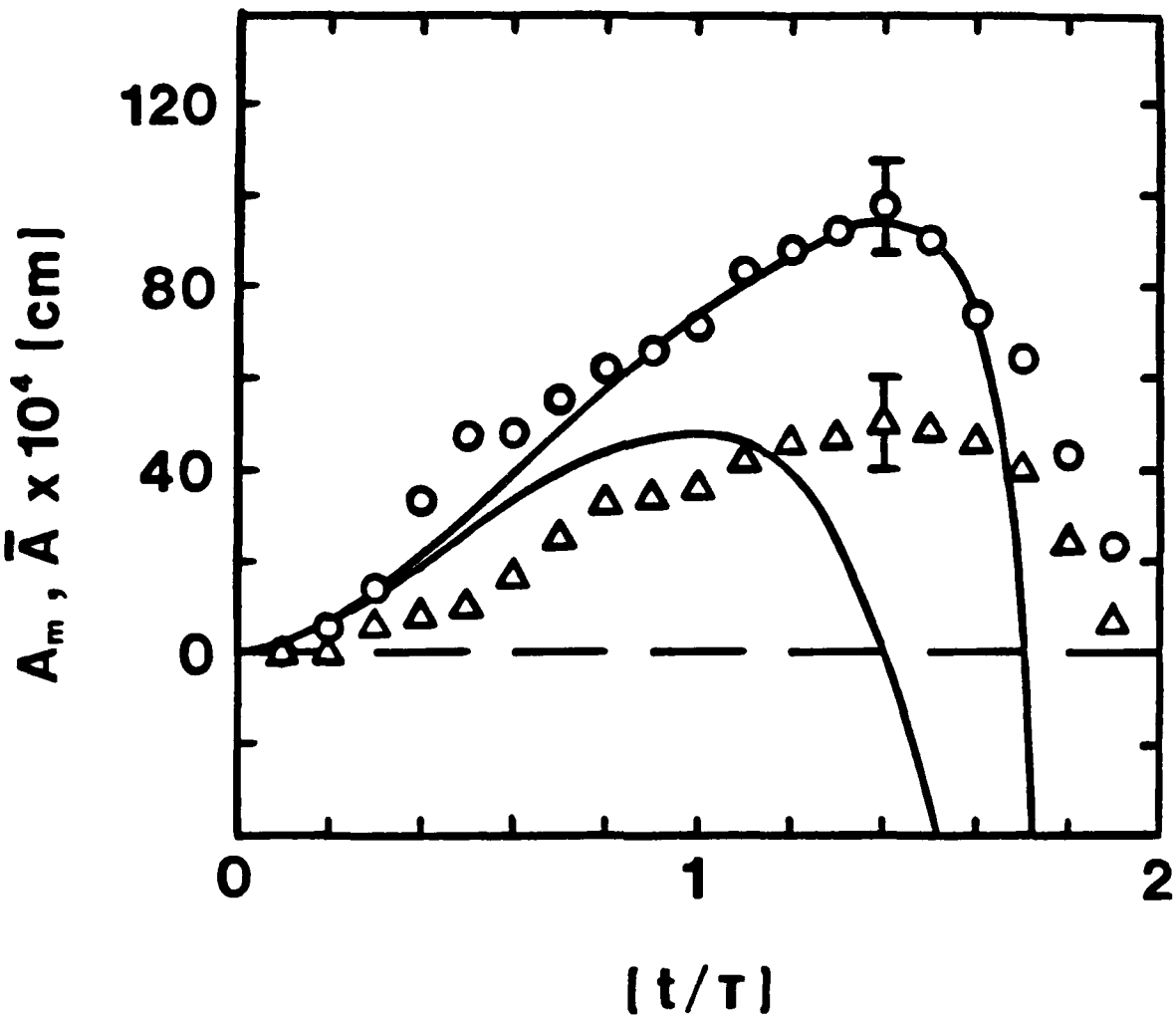

FIGURE 5-5A. Comparison of experiment and theory for deformation amplitude versus dimensionless time of bubbles in DH2O and dilute aqueous PAM solutions.
(ω = 575 rpm , $\dot{\gamma}$ = 170 sec^{-1})

symbol	fluid
○	DH2O
△	DH2O+1000PAM

adjusted relaxation times were within the range,

$$1.75 \leq \lambda \times 10^6 \text{ (sec)} \leq 2.25 \qquad \text{(DH2O+PAM)}.$$

For aqueous polyethylene oxide solutions including PEO* (four), the range of relaxation times was,

$$1.65 \leq \lambda \times 10^6 \text{ (sec)} \leq 2.00 \qquad \text{(DH2O+PEO,PEO*)}.$$

Finally, for polyacrylamide in glycerol, GLY(1:1)+500PAM, the appropriate relaxation times (three) were determined to be within,

$$2.00 \leq \lambda \times 10^6 \text{ (sec)} \leq 2.10 \qquad \text{(GLY+PAM)}.$$

Typical model/experiment comparisons for Newtonian predictions, non-Newtonian fits and experimental data are presented in Figures 5-5A, 5-5B and 5-5C. The figures show representative experimental and theoretical results of viscoelastic cavitation bubble deformation suppression for each of the three polymer solution groups investigated. Qualitatively, the viscoelastic model predictions displayed a temporal shift in the maximum deformation amplitude from a dimensionless time [t/τ] of about 1.4 to about 1.1, just past maximum bubble size. However, this shift was not observed experimentally. In a quantitative sense, the relationship between fluid elasticity and the reduction in

was experimentally observed) for a steady flow situation ($\tau_{flow} \rightarrow \infty$).

Modelling efforts, paralleling the experimental results for flow-induced bubble deformations in polymer solutions, required the specification of two additional fluid parameters. These were the elastic modulus (G_0) and the fluid relaxation time (λ). Reported values for polymer solution relaxation time, based on both theory and experiment, ranged from 10^{-2} to 10^{-6} sec. Therefore, the model relaxation time was assumed to be a freely adjustable parameter within these bounds for realistic values. In contrast, realistic values for the Maxwell element elastic modulus were not readily available. However, since Hara had investigated the effect of this parameter within the range of 10^{-2} to 10^{2} poise/sec, an intermediate value of unity was selected for all viscoelastic modelling efforts (G_0 = 1.00 poise/sec).

For a relaxation time value of zero, the model deformation predictions were qualitatively Newtonian (following the results for purely viscous solvents). Increased liquid viscosity and decreased surface tension resulted in slightly increased bubble deformation amplitudes. As anticipated, for small positive values of the fluid relaxation time ($\lambda \approx 10^{-5}$ - 10^{-6} sec), predicted nonspherical bubble amplitudes were significantly reduced. This qualitative agreement between theory and experiment was the most significant result of these model application efforts.

Quantitatively, viscoelastic deformation amplitude predictions were fit to the experimental results for the polymer solutions by adjusting the value of the relaxation time to match the predicted [max A_m] with the measured [max $\bar{A}$]. For aqueous polymer solutions (three), these

fluid : GLY(2:1)

physical properties :

density : $\rho = 1.17\ g/cm^3$

viscosity : $\eta = 0.164$ poise

surface tension : $\sigma = 66$ dyne/cm

experiment/model comparison :

ω(rpm)	$\dot{\gamma}(sec^{-1})$	R_0(cm)	ReN(A*)	Re(A*)	[max $\bar{A}$/max A_m]
360	105	0.480	19.3	17.0	+.0077/+.0065
480	140	0.460	25.7	24.6	+.0100/+.0087
575	170	0.453	30.8	30.4	+.0120/+.0103

experimental uncertainty :

[max $\bar{A}$] = X ± 0.0010 cm

TABLE 5-3B. Experimental/theoretical comparisons for GLY(2:1).

and 5-3B respectively. Although the predicted maximum deformation amplitudes fell within or nearly within the bounds of experimental uncertainty, the agreement between model predictions and experimental data worsened with increasing fluid viscosity. This progressive disparity was clearly displayed by comparisons of theoretical and experimental results for these three Newtonian solvents at a rotation rate of 575 rpm. Model prediction error (E) for that flow strength, defined as,

$$E \equiv \frac{[\max \bar{A}] - [\max A_m]}{[\max \bar{A}]} \tag{5-8}$$

increased from (-3%) to (-10%) to (-14%) as the viscosity increased from 1 cp to 6.4 cp to 16.4 cp for DH2O, GLY(1:1) and GLY(2:1) respectively. Despite these quantitative differences, the qualitative agreement was quite good.

Previous modelling efforts involving an oscillating external flow combined with flow decay and bubble collapse in a viscoelastic fluid (Hara, 1983) gave rise to somewhat ambiguous results. Depending on the flow frequency (described nondimensionally as τ_{flow}), fluid elasticity was found to result in either increased or decreased bubble nonsphericity. For the higher frequency case (smaller τ_{flow}), elastic effects caused increased bubble deformation upon collapse while for the lower frequency case (larger $\tau_{flow.}$), decreased bubble deformation was ultimately observed. An extrapolation of these results led to the qualitatively correct prediction of viscoelastic deformation reduction (as

fluid : GLY(1:1)

physical properties :

density : $\rho = 1.125\ g/cm^3$

viscosity : $\eta = 0.064$ poise

surface tension : $\sigma = 68$ dyne/cm

experiment/model comparison :

ω(rpm)	$\dot{\gamma}(sec^{-1})$	R_0(cm)	ReN(A*)	Re(A*)	[max $\bar{A}$/max A_m]
360	105	0.485	19.3	16.6	+.0070/+.0064
480	140	0.490	25.7	21.7	+.0090/+.0084
575	170	0.490	30.8	26.0	+.0111/+.0100

experimental uncertainty :

[max $\bar{A}$] = X ± 0.0010 cm

TABLE 5-3A. Experimental/theoretical comparisons for GLY(1:1).

fluid : DH20

physical properties :

density : $\rho = 1.00\ g/cm^3$

viscosity : $\eta = 0.01$ poise

surface tension : $\sigma = 71$ dyne/cm

experiment/model comparison :

ω(rpm)	$\dot{\gamma}(sec^{-1})$	R_0(cm)	ReN(A*)	Re(A*)	[max $\bar{A}$/max A_m]
360	105	0.463	19.1	18.0	+.0057/+.0059
480	140	0.458	25.5	24.6	+.0072/+.0079
575	170	0.474	30.6	27.6	+.0097/+.0094
720	210	0.446	38.2	38.9	+.0118/+.0114
865	255	0.427	45.8	50.9	+.0136/+.0139

experimental uncertainty :

[max $\bar{A}$] = X ± 0.0010 cm

TABLE 5-2. Experimental/theoretical comparisons for DH2O.

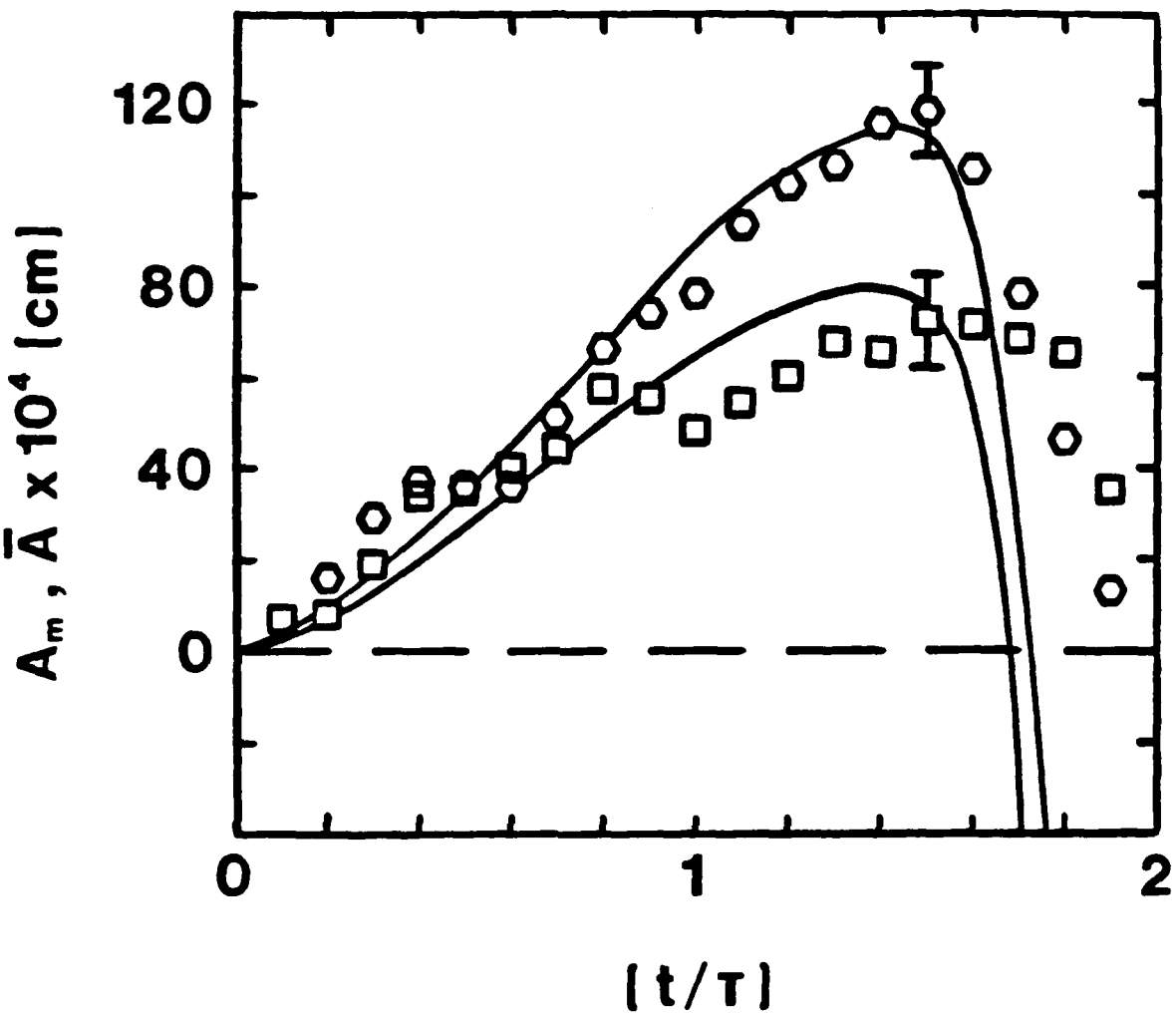

FIGURE 5-4. Comparison of experiment and model prediction for deformation amplitudes versus dimensionless time of bubbles in DH2O.

symbol	ω(rpm)	$\dot{\gamma}$(sec^{-1})
□	480	140
⬡	720	210

(from the origin) resulted in the following equations,

$$\begin{aligned} ReN(A^*) &\approx 0.0531(\omega) \\ &\approx 0.1800(\dot{\gamma}) \ . \end{aligned} \tag{5-6}$$

Appropriate model flow parameters, Re(A*), could thus be specified *a priori* for any of the experimental conditions (flow strengths and bubble sizes). First, the normalized model flow amplitude was determined from the particular experimental flow strength via either one of the above relationships. Then, this value was *renormalized* (corrected for the experimental bubble size) by the inverse relationship,

$$Re(A^*) = ReN(A^*)\ [R_m/R_0]^2 \tag{5-7}$$

to determine the model flow strength parameter for the experimental situation of interest (see Appendix B). Model predictions based on this approach were made for parameters corresponding to each of the five experimental DH2O flow composites. Comparisons of theory to experiment for two cases (ω = 480 and 720 rpm) are shown in Figure 5-4 and a summary of all five comparisons is presented in Table 5-2.

Similar theory/experiment comparisons for the two other Newtonian solvents, GLY(1:1) and GLY(2:1), are presented in Tables 5-3A

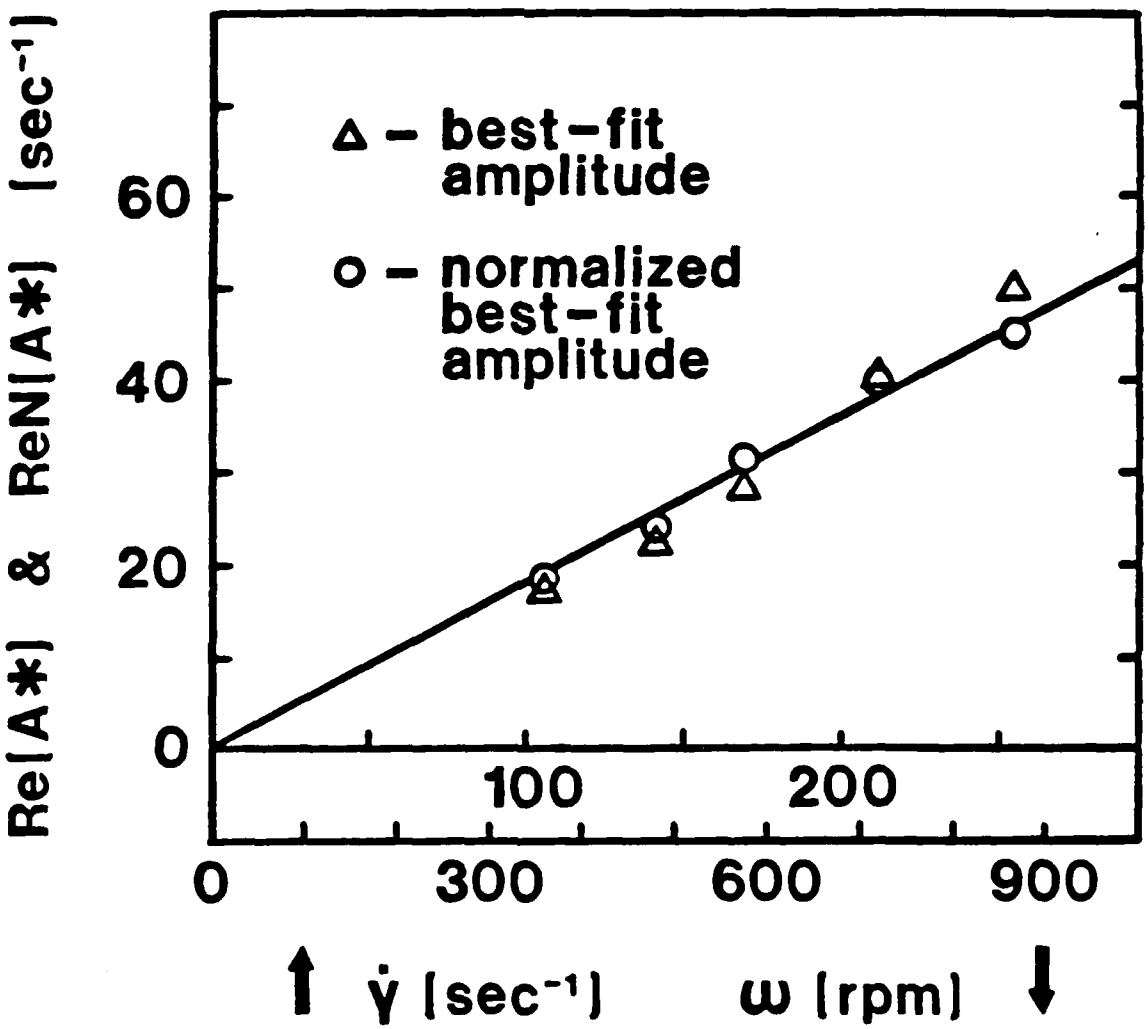

FIGURE 5-3. Linear relationship between experimental flow strength and (normalized) model flow parameter.

In both experiment and theory, substantial increases in fluid viscosity (up to 16x) resulted in only relatively small increases in bubble deformation (up to 25%). This observation was in sharp contrast to the linear relationship predicted by steady-state bubble deformation modelling. The results further demonstrated the dominance of inertial effects over viscous effects in nonspherical as well as spherical cavitation bubble dynamics. However, the agreement between experiment and theory progressively worsened (from within ± 10% to ± 15%) as fluid viscosity increased.

Experimentally, the effects of fluid viscosity were dwarfed by the dramatic bubble deformation suppression observed in viscoelastic polymer solutions. Nonspherical bubble dynamics were clearly shown to be influenced by the external flow through fluid rheology as qualitatively predicted by the application of Hara's model. Quantitatively, both experiment and theory demonstrated greater deformation reduction with increased fluid elasticity (see Tables 4-8A and 4-8B). These conclusions regarding the viscoelastic suppression of flow-induced deformation in model cavitation bubbles have been qualitatively related to hydraulic cavitation observations of a similar nature (see page 114). This connection was made by relating the decrease in deformation amplitude (increase in bubble nonsphericity) observed in polymer solutions to a predicted reduction in pressure-field amplitude upon bubble collapse resulting from this increase in sphericity (Chahine & Bovis, 1981).

The present research did, however, turn up some discrepancies between the physical observations and theoretical predictions. The

experimental results displayed a competition between viscous deformation promotion and elastic deformation suppression, the correct magnitude of which was not predicted theoretically. This competition was demonstrated experimentally by the upturn in the maximum amplitude data at higher polymer concentrations. Conversely, model results predicted a temporal shift in the position of the maximum deformation amplitude, relative to that for Newtonian solvents (for a value of (t/τ) from 1.4 to 1.1), which was not observed experimentally. These differences, while minor relative to the overall agreement of theory and experiment, have suggested both interesting extensions of the present work and important new directions for future fundamental research.

As is common in fundamental investigations, the results of the present study have raised as many questions as they have answered. Several immediate extensions of this research would serve to further elucidate the dynamic phenomenon of flow-induced cavitation bubble deformation. One interesting prospect would be flow experiments designed to produce significantly larger deformation amplitudes than achieved by this study, possibly approaching the values for steady-state flow deformation. This would necessitate substantial flow system modification in order to sustain the higher shear rates (200 to 500 sec^{-1}) with the higher solvent viscosities (2 to 5 poise) required for large bubble deformations.

The effect of bubble size on dynamic flow deformation is another question which has been brought to attention. Even though the present study has sought to simplify the analyses by examining bubbles within a fairly narrow size range, the model predictions demonstrated

greater self-consistency when input parameters were normalized to account for bubble size variations. The present experimental system is capable of producing and recording bubble dynamics for sizes from 0.1 to 1.0 centimeters in radius.

The effects of fluid physical properties, particularly viscosity and surface tension, on flow-induced bubble nonsphericity is a third area where immediate investigations can be made. The experimental data from this research clearly demonstrated that dynamic viscous effects did not follow the linear behavior predicted by steady-state deformation modelling. In fact, even the predictions of Hara's dynamic model began to differ significantly from experimental results for fluids of only moderate viscosity ($\eta \geq 0.1$ poise).

Fluid viscoelasticity and its effect of suppression of flow-induced bubble nonsphericity is an area where more quantitative work can be done. Specifically, a detailed examination of deformation suppression as a function of polymer concentration in the dilute regime ($0 \leq C(\text{wppm}) \leq 1000$ with $\Delta C = 100$ wppm) would be quite informative. The additional effects (if any) of polymer solutes at high concentrations ($C \approx 1$-10 wt.%) might prove interesting. Another area of interest, both experimentally and theoretically, is in the examination of polymer solute effects on jet formation from bubble collapse near a solid wall. An attempt to model this highly nonspherical phenomenon in a quiescent viscoelastic fluid and an effort to conduct related pilot experiments, are currently underway at Princeton University.

However, it is the combination of an imposed flow field with bubble collapse near a solid boundary (as occurs in hydraulic cavitation) which

could lead to the most important fundamental advances. The present study has sought to eliminate the solid boundary effects and focus on flow-induced bubble nonsphericity alone. This was easily accomplished by employing a sufficiently large annular test region for bubble dynamics experiments. Straightforward modifications of the flow system should easily permit bubble production sufficiently close to the inner cylinder (solid boundary) for the observation of wall effects (jet formation) both with and without the external shearing flow. Thus, the effects of fluid viscoelasticity on (a) flow-induced bubble deformation (present research), (b) bubble collapse near a solid boundary (research in progress) and (c) on combinations of these two situations (future research) can be systematically investigated. In this way, experimental advances and related theoretical predictions can attempt to model more accurately the hydraulic phenomenon which has served to motivate this and other research.

BIBLIOGRAPHY

Acosta, A.J. and B.R. Parkin
Cavitation inception - a selective review.
J. Ship Research 19, 193 (1975)

Apollo Lasers, Inc.
Apollo Ruby/Glass Laser Systems

Askar'yan, A., A.M. Prokhorov, G.F. Chanturiya and G.P. Shipulo
The effects of a laser beam in a liquid.
Soviet Physics JETP 17, 1463 (1963)

Barnes, P.A. and K.E. Rieckhoff
Laser induced underwater sparks.
Applied Physics Letters 13, 282 (1968)

Bell, C.E. and J.A. Landt
Laser-induced high-pressure shock waves in water.
Applied Physics Letters 10, 46 (1967)

Benjamin ,T.B. and A.T. Ellis
The collapse of cavitation bubbles and the pressures thereby produced against solid boundaries.
Phil. Trans. Royal Soc., London A260, 221 (1966)

Besant, W.H.
Hydrostatics and Hydrodynamics
Article 158, Cambridge University Press (1859)

Bird, R.B., W.E. Stewart and E.N. Lightfoot
Transport Phenomena
J. Wiley (1960)

Bird, R.B., R.C. Armstrong and O. Hassager
Dynamics of Polymeric Liquids: Volume 1. Fluid Mechanics
J. Wiley (1977)

Bird, R.B., O. Hassager R.C. Armstrong and C.F. Curtiss
Dynamics of Polymeric Liquids: Volume 2. Kinetic Theory
J. Wiley (1977)

Bjorno, L., ed.
Finite Amplitude Wave Effects in Fluids
IPC Science and Tecnology Press (1974)

Blake, J.R. and D.C. Gibson
Growth and collapse of a vapor cavity near a free surface.
J. Fluid Mech. 111, 123 (1981)

Born, M. and E. Wolf
Principles of Optics, 3rd ed.
Pergamon Press (1965)

Brennen, C.
Some cavitation experiments with dilute polymer solutions.
J. Fluid Mech. **44**, 51 (1970)

Brewer, R.G. and K.E. Riechoff
Stimulated Brillouin scattering in liquids.
Phys. Review Letters **13**, 334 (1964)

Carome, E.F., C.E. Moeller and N.A. Clark
Intense ruby-laser-induced acoustic impulses in liquids.
Acoust. Soc. Amer. J. **40**, 1462 (1966)

Carome, E.F., E.M. Carreira and C.J. Prochaska
Photographic studies of laser-induced pressure impulses in liquids.
Appl. Physics Letters **11**, 64 (1967)

Chahine, G.L.
Interaction between an oscillating bubble and a free surface.
Trans. ASME, J. Fluids Eng. **99**, 709 (1977)

Chahine, G.L.
Experimental and asymptotic study of nonspherical bubble collapse.
Appl. Sci. Research **38**, 187 (1982)

Chahine, G.L. and D.H. Fruman
Dilute polymer solution effects on bubble growth and collapse.
Phys. Fluids **22**, 1406 (1979)

Chahine, G.L. and A.G. Bovis
Oscillation and collapse of a cavitation bubble in the vicinity of a two liquid interface.
In *Cavitation and Inhomogeneities in Underwater Acoustics* 23, Springer-Verlag (1980)

Chahine, G.L. and A.G. Bovis
Pressure field generated by nonspherical bubble collapse.
Proc. ASME Symp. Cav. Erosion in Fl. Syst., Boulder CO, 27 (1981)

Chang, C.F.
Secondary flow induced by a cylinder oscillating in a viscoelastic liquid.
Ph.D. Thesis, Princeton University (1975)

Chang, C.F. and W.R. Schowalter
Flow near an oscillating cylinder in a dilute viscoelastic fluid.
Nature **252**, 686 (1974)

Chapman, R.B. and M.S. Plesset
Nonlinear effects in the collapse of a nearly spherical cavity in a liquid.
Trans. ASME, J. Basic Eng. D94, 142 (1972)

Cordin (1965)
Operating Manual - Model 350 Framing Camera

Crowley, D.G., F.C. Frank, M.R. Mackley and R.G. Stephenson
Localized flow birefringence of polyethylene oxide solutions in a four-roll mill.
J. Polym. Sci., Polym. Phys. Ed. 14, 1111 (1976)

Dergarabedian, P.
The rate of growth of vapor bubbles in superheated water.
Trans. ASME, J. Appl. Mech. 75, 537 (1953)

Ebeling, K.J.
Applications of high-speed holocinematographical methods in cavitation research.
In *Cavitation and Inhomogeneities in Underwater Acoustics*
35, Springer-Verlag (1980)

Ellis, A.T., J.G. Waugh and R.Y. Ting
Cavitation suppression and stress effects in high-speed flows of water with dilute macromolecule additives.
Trans. ASME, J. Basic Eng. D92, 459 (1970)

Ellis, A.T. and R.Y. Ting
Non-Newtonian effects on flow generated cavitation and on cavitation generated in a pressure field.
In *Fluid Mechanics, Acoustics and Design of Turbomachinery*
NASA-SP-304, 403 (1974)

Felix, M.P. and A.T. Ellis
Laser-induced liquid breakdown - a step-by-step account.
Appl. Phys. Letters 19, 484 (1971)

Fogler, H.S. and J.D. Goddard
Collapse of spherical cavities in viscoelastic fluids.
Phys. Fluids 13, 1135 (1970)

Fujikawa, S. and T. Akamatsu
Effects of the non-equilibrium condensation of vapor on the pressure wave produced by the collapse of a bubble in a liquid.
J. Fluid Mech. 97, 481, (1980)

Fuller, G.G. and L.G. Leal
Flow birefringence of concentrated polymer solutions in two-dimensional flows.
J. Polym. Sci., Polym Phys. Ed. 19, 556 (1981)

Gibson, D.C.
The pulsation time of spark-induced bubbles.
Trans. ASME, J. Basic Eng. D94, 248, (1972)

Gibson, D.C. and J.R. Blake
The growth and collapse of bubbles near deformable surfaces.
Appl. Sci. Research 38, 215 (1982)

Gilmore, F.R.
The growth or collapse of a spherical bubble in a viscous compressible liquid.
Proc. Heat Transfer and Fluid Mech. Inst., 53 (1952)

Hammitt, F.G.
Observations of cavitation damage in a flowing system.
Trans. ASME, J. Basic Eng. D85, 347 (1963)

Hammitt, F.G.
Cavitation and Multiphase Flow Phenomena
McGraw-Hill (1980)

Hara, S.K.
The effects of flow and non-Newtonian fluids on nonspherical cavitation bubbles.
Ph.D. Thesis, Princeton University (1983)

Hara, S.K. and W.R. Schowalter
Dynamics of nonspherical bubbles surrounded by a viscoelastic fluid.
J. Non-Newt. Fl. Mech. 14, 249 (1984)

Hentschel, W. and W. Lauterborn
Holographic generation of multi-bubble systems.
In *Cavitation and Inhomogeneities in Underwater Acoustics*
47, Springer-Verlag (1980)

Hentschel, W. and W. Lauterborn
Acoustic emmissions of single laser-produced cavitation bubbles and their dynamics.
Appl. Sci. Research 38, 225 (1982)

Hickling, R.
Some physical effects of cavity collapse in liquids.
Trans. ASME, J. Basic Eng. D88, 229 (1966)

Hickling, R. and M.S. Plesset
Collapse and rebound of a spherical bubble in water.
Phys. Fluids 7, 7 (1964)

Hoyt, J.W.
Effect of polymer additives on jet cavitation.
Trans. ASME, J. Fluids Eng. 98, 106 (1976)

Hsieh, D.Y.
Some analytical aspects of bubble dynamics.
Trans. ASME, J. Basic Eng. D87, 991 (1965)

Hsieh, D.Y.
On the dynamics of nonspherical bubbles.
Trans. ASME, J. Basic Eng. D94, 655 (1972)

Inge, C. and F. Bark
Surface tension driven oscillations of a bubble in a viscoelastic liquid.
Appl. Sci. Research 38, 231 (1982)

Ivany, R.D. and F.G. Hammitt
Cavitation bubble collapse in viscous, compressible liquids - numerical analysis.
Trans. ASME, J. Basic Eng. D87, 977 (1965)

Johnsson, C.A.
Cavitation inception on head forms, further tests.
Proc. 12th ITTC, Rome, 381 (1969)

Kirkwood, J.G. and H.A. Bethe
The pressure wave produced by an underwater explosion.
OSRD Report 588 (1942)

Kling,C.L. and F.G. Hammitt
A photographic study of spark-induced cavitation bubble collapse.
Trans. ASME, J. Basic Eng. D94 825 (1972)

Knapp, R.T.
Recent investigations of cavitation and cavitation damage.
Trans. ASME 77, 1045 (1955)

Knapp, R.T., J.W. Daly and F.G. Hammitt
Cavitation
McGraw-Hill (1970)

Kornfeld, M. and L. Suvorov
On the destructive action of cavitation.
J. Appl. Phys. 15, 495 (1944)

Lamb, Sir H.
Hydrodynamics
Dover (1945)

Lauterborn, W.
High-speed photography of laser-induced breakdown in liquids.
Appl. Phys. Letters 21, 27 (1972)

Lauterborn, W.
General and basic aspects of cavitation.
In *Finite Amplitude Wave Effects in Fluids*
195, IPC Science and Technology Press (1974)

Lauterborn, W. and H. Bolle
Experimental investigations of cavitation bubble collapse in the neighborhood of a solid boundary.
J. Fluid Mech. **72**, 391 (1975)

Lauterborn, W. and H. Bolle
On the production of bubbles by focussed laser light.
Proc. Int. Colloq. on Drops and Bubbles,
Pasadena CA, 322 (1976)

Lauterborn, W.
Liquid jets from cavitation bubble collapse.
Proc. 5th Int. Conf. on Eros. by Sol. and Liq. Imp.,
Cambridge GB (1979)

Lauterborn, W., ed.
Cavitation and Inhomogeneities in Underwater Acoustics
Springer-Verlag (1980)

Lauterborn, W.
Cavitation and coherent optics.
In *Cavitation and Inhomogeneities in Underwater Acoustics*
3, Springer-Verlag (1980)

Lauterborn, W.
Cavitation bubble dynamics - new tools for an intricate problem.
Appl. Sci. Research **38**, 165 (1982)

Lauterborn, W. and K.J. Ebeling
High-speed holography of laser-induced breakdown in liquids.
Appl. Phys. Letters **31**, 663 (1977)

Lauterborn, W. and R. Timm
Bubble collapse at a million frames per second.
In *Cavitation and Inhomogeneities in Underwater Acoustics*
42, Springer-Verlag (1980)

Lauterborn, W. and A. Vogel
Modern optical techniques in fluid mechanics.
Ann. Rev. Fluid Mech. **16**, 223, (1984)

Mark, H.F. et al., ed.
Encyclopedia of Polymer Science and Technology
J. Wiley (1966)

Marshall, S.L.
Laser Technology and Its Applications
McGraw-Hill (1968)

Melles Griot (1981)
Optics Guide 2

Mitchell, T.M. and F.G. Hammitt
Asymmetric cavitation bubble collapse.
Trans. ASME, J. Fluids Eng. **95**, 29 (1973)

Naude, C.F. and A.T. Ellis
On the mechanism of cavitation damage by hemispherical cavities collapsing in contact with a solid boundary.
Trans. ASME, J. Basic Eng. **D83**, 648 (1961)

Noltingk, B.E. and E.A. Neppiras
Cavitation produced by ultrasonics.
Proc. Phys. Soc., London, J. Phys. **B63**, 674 (1950)

Oba, R., Y. Ito and K. Uranishi
Effect of polymer additives on cavitation development and noise in water flow through an orifice.
Trans. ASME, J. Fluids Eng. **100**, 493 (1978)

Padday, J.F., A.R. Pitt and R.M. Pashley
Menisci at a free surface: surface tension from the maximum pull on a rod.
J. Chem. Soc., Faraday Trans. I **71**, 1919 (1975)

Pearson, G. and S. Middleman
Elongational flow behavior of viscoelastic liquids: Part 1. Modeling of bubble collapse. Part 2. Definition and measurement of apparent elongational viscosity.
AIChE J. **23**, 714 (1977)

Pearson, G. and S. Middleman
Elongational flow behavior of viscoelastic liquids: Modelling Bubble dynamics with viscoelastic constitutive relations.
Rheol. Acta **17**, 500 (1978)

Perry, R.H. and C.H. Chilton, ed.
Chemical Engineer's Handbook, 5th ed.
McGraw-Hill (1973)

Plesset, M.S.
On the stability of flows with spherical symmetry.
J. Appl. Phys. **25**, 96 (1954)

Plesset, M.S.
Bubble dynamics and cavitation erosion.
In *Finite Amplitude Wave Effects in Fluids*
203, IPC Science and Technology Press (1974)

Plesset, M.S. and T.P. Mitchell
On the stability of the spherical shape of a vapor cavity in a liquid.
Quart. Appl. Math. **13**, 419 (1956)

Plesset, M.S. and R.B. Chapman
Collapse of an initially spherical vapour cavity in the neighborhood of a solid boundary.
J. Fluid Mech. **47**, 283 (1971)

Plesset, M.S. and A. Prosperetti
Bubble dynamics and cavitation.
Ann. Rev. Fluid Mech. **9**, 145 (1977)

Poritsky, H.
The collapse or growth of a spherical bubble or cavity in a viscous liquid.
Proc. First U.S. Nat. Cong. Appl. Mech., 813 (1952)

Prosperetti, A.
On the dynamics of nonspherical bubbles.
In *Cavitation and Inhomogeneities in Underwater Acoustics* 13, Springer-Verlag (1980)

Prosperetti, A.
A generalization of the Rayleigh-Plesset equation of bubble dynamics.
Phys. Fluids **25**, 409 (1982)

Prosperetti, A.
Bubble dynamics: a review and some recent results.
Appl. Sci. Research **38**, 145 (1982)

Prosperetti, A. and M.S. Plesset
Vapor-bubble growth in a superheated liquid.
J. Fluid Mech. **85**, 349 (1978)

Prosperetti, A. and G. Seminara
Linear stability analysis of a growing or collapsing bubble in a slightly viscous liquid.
Phys. Fluids **21**, 1465 (1978)

Rayleigh, Lord (J.W. Strutt)
On the pressure developed in a liquid during the collapse of a spherical cavity.
Philos. Mag. **34**, 94 (1917)

Reynolds, O.
Experiments showing the boiling of water in an open tube at ordinary temperatures.
Brit. Assoc. Adv. Sci., Report 546 (1894)
also Science Papers **2**, 578 (1901)

Roach, J.F., W. Zagieboylo and J.M. Davies
Shock wave generation in dielectric liquids using a Q-switched laser.
Proc. IEEE **57**, 1693 (1969)

Schlicting, H.
Boundary-Layer Theory, 6th ed.
McGraw-Hill (1968)

Schowalter, W.R.
Mechanics of Non-Newtonian Fluids
Pergamon Press (1978)

Scrivner, O., C. Benner, R. Cressely, R. Hoquart et al.
Dynamical behavior of drag-reducing polymer solutions.
J. Non-Newt. Fluid Mech. **5**, 475 (1979)

Singurel, G.
Dielectric breakdown and cavitation in liquids produced by ruby laser radiation.
Rev. Roum. Phys. **14**, 337 (1969)

Shapoval, I.F. and K.K. Shal'nev
Cavitation and erosion in aqueous solutions of polyacrylamide.
Sov. Phys. Dokl. **22**, 635 (1977)

Shima, A. and T. Tsujino
The behavior of bubbles in polymer solutions.
Chem. Eng. Sci. **31**, 863 (1976)

Shima, A. and T. Tsujino
On the dynamics of bubbles in aqueous polymer solutions.
Appl. Sci. Research **38**, 255 (1982)

Shutler, N.D. and R.B. Mesler
A photographic study of the dynamics and damage capabilities of bubbles collapsing near solid boundaries.
Trans. ASME, J. Basic Eng. **D87**, 511 (1965)

Stamberg, R.C. and D.E. Gillespie
Laser-stimulated nucleation in a bubble chamber.
J. Appl. Phys. **37**, 459 (1966)

Telesenko, V.S.
Experimental investigation of bubble collapse at laser-induced breakdown in liquids.
In *Cavitation and Inhomogeneities in Underwater Acoustics*
30, Springer-Verlag (1980)

Ting, R.Y.
Cavitation suppression by polymer additives: concentration effect and implication on drag reduction.
AIChE J. **20**, 827 (1974)

Ting, R.Y.
Viscoelastic effect of polymers on single bubble dynamics.
AIChE J. **21**, 810 (1975)

Ting, R.Y.
Polymer effects on microjet impact and cavitation erosion.
Nature 262, 572 (1976)

Ting, R.Y.
Effect of polymer viscoelasticity on the initial growth of a vapor bubble from gas nuclei.
Phys. Fluids 20, 1427 (1977)

Ting, R.Y.
Characterisics of flow cavitiation in dilute solutions of polyacrylamide and polyethylene oxide.
Phys. Fluids 21, 898 (1978)

Ting, R.Y. and A.T. Ellis
Bubble growth in dilute polymer solutions.
Phys. Fluids 17, 1461 (1974)

van Wijngaarden, L., ed.
Mechanics and Physics of Bubbles in Liquids
Appl. Sci. Research 38, Martinus Nijhoff (1982)

Voinov, O.V. and V.V. Voinov
On the process of collapse of a cavitation bubble near a wall and the formation of a cumulative jet.
Sov. Phys. Dokl. 21, 133 (1976)

Weast, R.C., ed.
CRC Handbook of Chemistry and Physics, 55th ed.
CRC Press (1974)

Wendt, F.
Turbulente stromungen zwischen zwei rotierenden konaxialen zylindern.
Ing. Arch. 4, 577 (1933) (in German)

Yariv, A.
Introduction to Optical Electronics, 2nd ed.
Holt, Rinehart and Winston (1976)

t(μsec)	R_m(cm)	A_m(cm)
0	0.000	0.00
50	0.200	+.0002
100	0.318	+.0008
150	0.364	+.0016
200	0.395	+.0024
250	0.430	+.0034
300	0.451	+.0044
350	0.458	+.0053
400	0.468	+.0063
450	0.476	+.0073
500	0.471	+.0081
550	0.460	+.0087
600	0.453	+.0092
650	0.436	+.0094
700	0.403	+.0082
750	0.370	+.0035
800	0.332	-.0102
850	0.233	-
900	0.047	-

TABLE B-3. Sample model bubble predictions.

renormalized model flow amplitude from equation 5-7 was given by,

$$Re(A^*) = 30.6\ (0.45/R_0)^2$$
$$\approx 27.6$$

For predicting bubble dynamics in DH2O and other Newtonian fluids, this model flow amplitude as well as the experimental and theoretical parameters from Table B-1 served as a typical data set for Hara's numerical model (see Chapter 5). The modelling involved the simultaneous numerical solution of three differential and/or integro-differential equations (III.27, III.32 and III.34) subject to the specified radial bubble profile $R_{fit}(t)$ and the appropriate ambient flow conditions (III.29 and III.30) (Hara, 1983). Sample model predictions (dimensional bubble radius and deformation amplitude versus dimensional time) for conditions corresponding to those for the sample experimental data (Table B-2) are presented in Table B-3.

For modelling bubble dynamics in a non-Newtonian fluid only two additional parameters needed to be specified (see Table B-1). The appropriate integro-differential equations for the inclusion of fluid viscoelasticity were III.41, III.44, III.45 and III.46 (Hara, 1983). In addition, the radial profile and ambient flow conditions were the same as in the Newtonian fluid case. Finally, the format for the input of the data into the numerical scheme is documented in the program listing (available from the author).

(t/τ)	$\overline{(R/R_0)}$	$\overline{A}$(cm)
0.00	0.00	-
0.10	0.412	0.00
0.20	0.625	+.0005
0.30	0.745	+.0014
0.40	0.827	+.0033
0.50	0.888	+.0047
0.60	0.933	+.0048
0.70	0.966	+.0055
0.80	0.984	+.0062
0.90	0.998	+.0066
1.00	0.998	+.0071
1.10	0.986	+.0083
1.20	0.970	+.0088
1.30	0.944	+.0092
1.40	0.906	+.0097
1.50	0.860	+.0090
1.60	0.799	+.0074
1.70	0.720	+.0064
1.80	0.610	+.0043
1.90	0.404	+.0023
2.00	-0.009	+.0001

TABLE B-2. Sample bubble composite data.

resulted in nearly identical values for the series coefficients. These were,

$$C_1 = 0.5412 \text{ cm}$$
$$C_2 = 0.0951 \text{ cm}$$
$$C_3 = 0.0397 \text{ cm}$$
$$C_4 = 0.0201 \text{ cm}$$
$$C_5 = 0.0107 \text{ cm}$$

for the coefficients of the included odd (2i-1) series terms. The coefficients for all even series terms (not included) were at least a factor of ten smaller than the smallest coefficient of the included series terms.

With this series representation of the spherical bubble data and the known physical properties of the fluid, for steady flow modelling (see Chapter 5) only the flow strength parameter, Re(A*), needed to be specified. From equation 5-6, the normalized model flow amplitude was determined to be,

$$\begin{aligned} ReN(A^*) &= 0.18\,\dot{\gamma} \\ &\approx 30.6 \end{aligned}$$

This value was then modified to account for the variation in bubble radius from the overall experimental mean (R_m = 0.45 cm). The

physical properties :

fluid density :	ρ = 1.00 gm/cm^3
fluid viscosity :	η = 0.01 poise
surface tension :	σ = 71.0 dyne/cm
rotation rate :	ω = 575 rpm
shear rate :	$\dot{\gamma}$ = 170 sec^{-1}

spherical parameters :

comp. max. radius :	R_0 = 0.474 cm
norm. bubble lifetime :	$(2\tau/R_0)$ = 1921 μsec
avg. bubble lifetime :	2τ = 911 μsec

numerical parameters :

flow decay constants :	$(1/\zeta) = 10^{-10}$ sec^{-1}
	$(1/t_{decay}) = 10^{-10}$ sec^{-1}
flow osc. frequency :	$\Omega = 10^{-10}$ sec^{-1}

non-Newtonian parameters :

relaxation time :	$10^{-6} \leq \lambda(\text{sec}) \leq 10^{-5}$
elastic modulus :	G_0 = 1.00 poise

TABLE B-1. Physical properties, spherical parameters and numerical parameters.

APPENDIX B

Sample Calculations.

The application of Hara's theoretical model to these experimental results followed a straightforward procedure. An example of this procedure is presented below for a deformation amplitude composite of a bubble in distilled water (DH2O) at a flow system rotation rate of 575 rpm (shear rate: $\dot{\gamma} \approx 170\ sec^{-1}$). The composite spherical parameters, appropriate physical properties and numerical model parameters are presented in Table B-1. The composites of dimensionless radius and deformation amplitude versus dimensionless time are presented in Table B-2.

Next, the radial profile composite was represented by a Fourier sign series approximation (equation 5-1A). The coefficients (C_i) were determined by a numerical integration of equation 5-1B in which the experimental radial data are given by,

$$R(t) = R(t/\tau) = (R/R_0)\,\overline{R_0} \qquad \text{(B-1)}$$

where (R/R_0) is the average dimensionless radius and $\overline{R_0}$ is the composite maximum bubble radius. A numerical time step in the range of 0.5 to 1.0 μs was used for the integration. The use of either the trapezoidal rule or Simpson's rule to interpolate between the data points

contents (assuming saturation conditions), and (c) comparing the latent heat of vaporization for the contents to the experimentally measured bubble energy. More detailed modelling, possibly including shock wave energy loss and non-ideal vapor expansion, should lead to even better quantitative agreement.

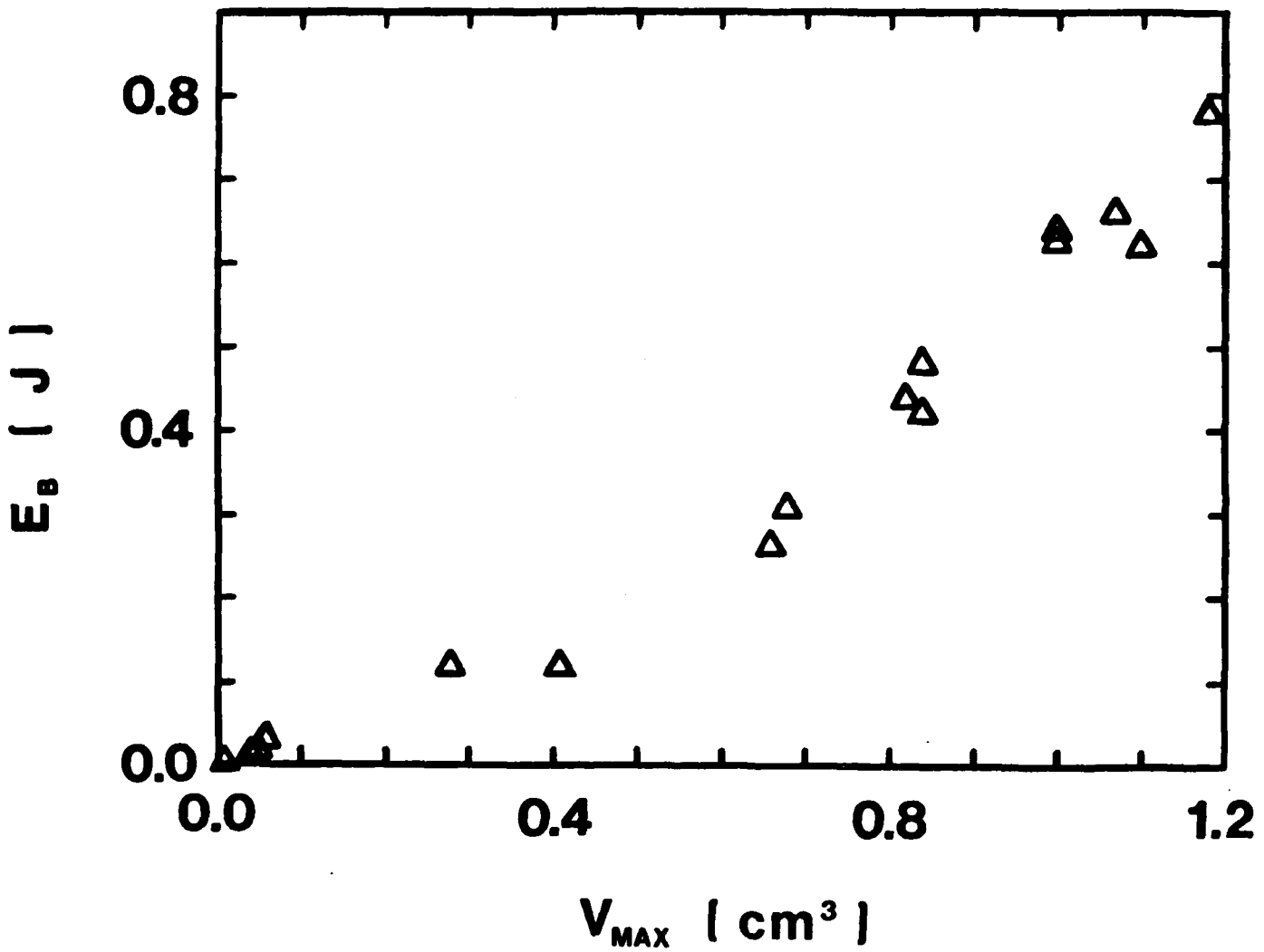

FIGURE A-3. Bubble nucleation energy versus maximum bubble volume.

E_{cal}(J)	E_b(J)	R_{max}(cm)	V_{max}(cm³)
0.08	0.004	0.13	0.01
0.08	0.016	0.205	0.04
0.08	0.021	0.225	0.05
0.08	0.027	0.245	0.06
0.29	0.12	0.405	0.28
0.29	0.12	0.46	0.41
0.49	0.265	0.54	0.66
0.49	0.31	0.55	0.67
0.82	0.42	0.585	0.84
0.70	0.44	0.58	0.82
0.82	0.48	0.585	0.84
1.00	0.62	0.64	1.10
0.94	0.63	0.62	1.00
0.94	0.64	0.62	1.00
1.00	0.66	0.635	1.07
1.11	0.78	0.655	1.18

TABLE A-2. Bubble nucleation energy data versus maximum bubble size for bubbles in DH2O.

this reflection was the sole source of energy loss since no appreciable liquid (DH2O) absorption occurred. The loss from each lens (both surfaces) was determined to be 5 ± 1% of the total incident energy. With this result, the bubble nucleation energy (E_b) was easily determined from the laser output energy (E_{cal}) (for the appropriate capacitor voltage) and the transmitted energy (E_{net}) measured by the laser calorimeter. With nucleation,

$$E_b = E_{cal}(1-L) - E_{net}/(1-L) \qquad \text{(A-3)}$$

where L is the lens reflective loss determined above.

High-speed photography was again used to record the dynamics of these essentially spherical bubbles in distilled water. Bubble sizes were measured from the *microfilm prints* as described in Chapter 4. The data for bubble energy and maximum bubble size (radius R and/or volume V) are presented in Table A-2 and Figure A-3. These data and this experimental technique should be useful in research aimed at (a) bubble/shock energy balances and measurements (Hentschel & Lauterborn, 1982) or (b) internal vapor/gas pressure and temperature modelling (Fujikawa & Akamatsu, 1980). A crude modelling effort based on adiabatic bubble growth from a high-pressure nucleus (RNNP theory) was found to be in agreement with these preliminary energy measurements to within ± 20-40%. This modelling involved (a) choosing the nucleus vapor pressure and the vapor expansion coefficient which would result in the desired maximum bubble size, (b) using the vapor pressure at maximum bubble size to determine the mass of the bubble

V_{cap}(% max)	E_{cal}(J)
78.0	0.29 ± 0.01
80.0	0.49 ± 0.01
82.0	0.70 ± 0.01
84.0	0.82 ± 0.02
86.0	0.94 ± 0.02
88.0	1.00 ± 0.02
90.0	1.11 ± 0.02

TABLE A-1. Laser output energy calibration results.

measurements of the unobstructed laser output as a function of capacitor bank voltage (V_{cap}) over the range of interest (Table A-1). The second required the determination of the reflective energy losses from the focussing and collimating lenses. This was accomplished by measuring the laser pulse energy with the test cell in place (E_{net}) at a sufficiently low charge voltage to preclude cavity nucleation. This transmitted energy was then referenced to the energy of the unobstructed laser pulse (E_{cal}) to reveal the percentage energy loss (L) due to reflection from the two lenses. Without nucleation,

$$E_{net} = E_{cal} (1 - L)^2 \qquad \text{(A-1)}$$

$$L = 1 - (E_{net}/E_{cal})^{\frac{1}{2}} \qquad \text{(A-2)}$$

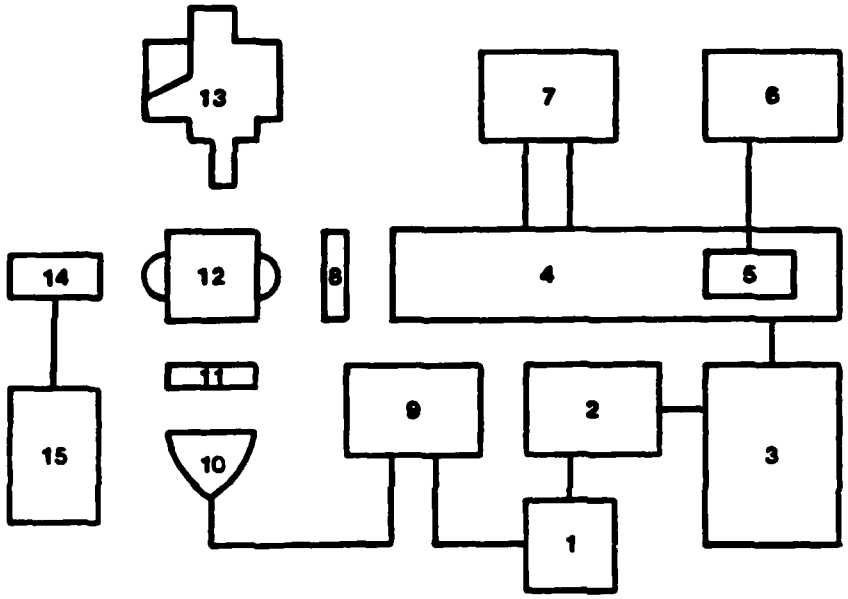

1 SYSTEM TRIGGER
2 DELAY GENERATOR
3 LASER POWER SUPPLY
4 RUBY LASER
5 HeNe LASER
6 HeNe POWER SUPPLY
7 COOLING SYSTEM
8 LASER FILTER
9 FLASH POWER SUPPLY
10 FLASHLAMP HEAD
11 FRESNEL LENS AND/OR FLASH DIFFUSER
12 ENERGY TEST CUVETTE
13 HIGH-SPEED CAMERA
14 LASER CALORIMETER
15 CALORIMETER POWER SUPPLY

FIGURE A-2. *Schematic diagram of the equipment configuration for energy tests.*

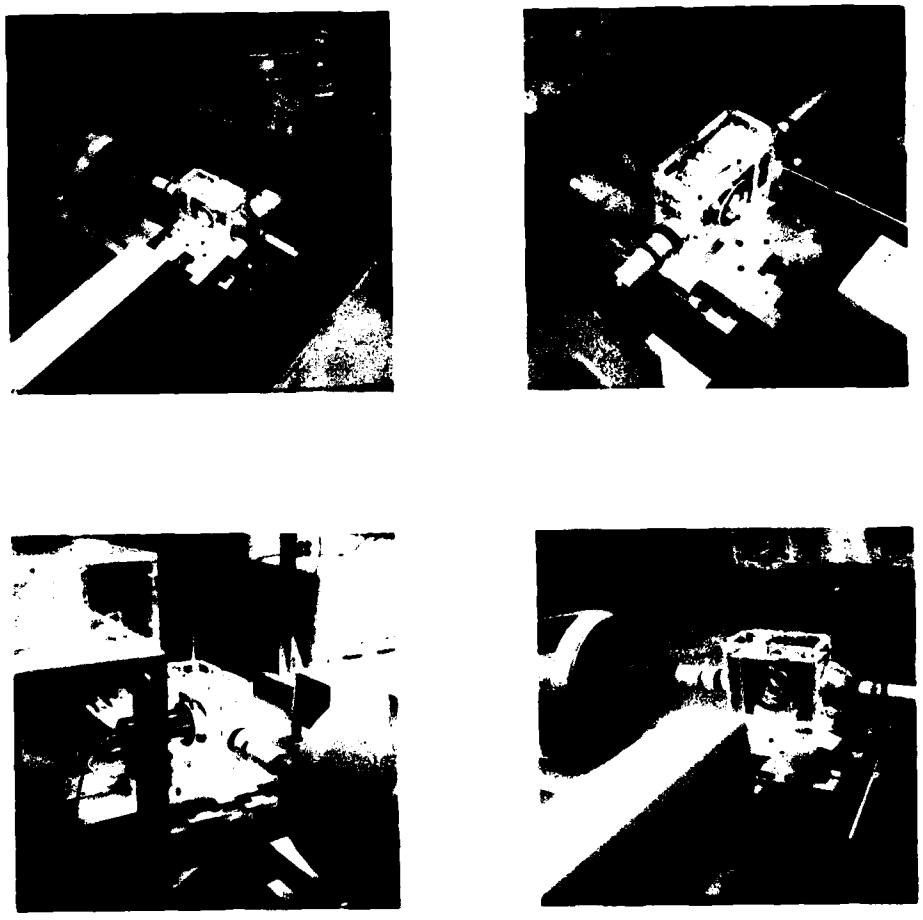

FIGURE A-1. Equipment configuration for bubble energy measurement experiments.

APPENDIX A

Bubble Energy Measurements.

In addition to the numerous experiments performed on the flow-induced deformation of model cavitation bubbles, a new technique for bubble energy measurements was briefly explored. With the technique of laser-induced bubble production there was considerable uncertainty in any *a priori* estimation of the energy involved in actual cavity formation. While the laser pulse energy was quite reproducible from shot-to-shot (± 5%), the fraction of energy absorbed in the bubble nucleation process was not. Microscopic impurities, such as dust, in the vicinity of the laser focal point resulted in relatively large variations in bubble size,

$$\Delta(\text{radius}) : \pm 10 - 20\%$$

$$\Delta(\text{volume}) : \pm 30 - 60\%$$

for similar laser pulse energies (identical laser capacitor bank charge voltages).

The technique which was developed involved the use of a laser calorimeter for energy measurements (see Table 3-7) and a quiescent energy test cell for focussing and collimating the laser pulse (see Figure 3-5). The experimental configuration for these tests is shown photographically in Figure A-1 and schematically in Figure A-2. Initially, two system calibrations were performed. The first involved

END

FILMED

7-85

DTIC